

AD-A071 950

TORONTO UNIV DOWNSVIEW (ONTARIO) INST FOR AEROSPACE --ETC F/G 20/9
FINITE-DIFFERENCE SOLUTIONS FOR NONEQUILIBRIUM LAMINAR BOUNDARY--ETC(U)
MAY 79 W S LIU

AFOSR-77-3303

UNCLASSIFIED

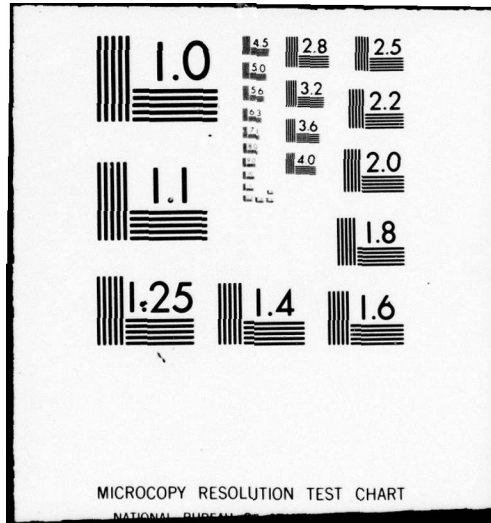
UTIAS-226

AFOSR-TR-79-0884

NL

1 OF 2
ADA
071950





AFOSR-TR-

79-0884

FINITE-DIFFERENCE SOLUTIONS FOR NONEQUILIBRIUM LAMINAR BOUNDARY LAYERS
IN IONIZING-ARGON FLOWS

LEVEL

by

W. S. Liu

DDC
RECEIVED
JUL 30 1979
RECEIVED
C

DA071950

DDC FILE COPY

May, 1979

Approved for public release;
distribution unlimited.

UTIAS Report No. 226
CN ISSN 0082-5255

79 07 27 072

UNCLASSIFIED

SECURITY CLASSIFICATION OF THIS PAGE (When Data Entered)

REPORT DOCUMENTATION PAGE		READ INSTRUCTIONS BEFORE COMPLETING FORM
1. REPORT NUMBER AFOSR-TR-79-8884	2. GOVT ACCESSION NO.	3. RECIPIENT'S CATALOG NUMBER
4. TITLE (and Subtitle) FINITE-DIFFERENCE SOLUTIONS FOR NONEQUILIBRIUM LAMINAR BOUNDARY LAYERS IN IONIZING-ARGON FLOWS.		5. TYPE OF REPORT & PERIOD COVERED INTERIM Rept.
7. AUTHOR(s) W. S. LIU		6. PERFORMING ORG. REPORT NUMBER UTIAS Report No 226
9. PERFORMING ORGANIZATION NAME AND ADDRESS UNIVERSITY OF TORONTO INSTITUTE FOR AEROSPACE STUDIES, 4925 DUFFERIN ST DOWNSVIEW, ONTARIO, CANADA, M3H 5T6		8. CONTRACT OR GRANT NUMBER(s) AFOSR-77-3303
11. CONTROLLING OFFICE NAME AND ADDRESS AIR FORCE OFFICE OF SCIENTIFIC RESEARCH/NA BLDG 410 BOLLING AIR FORCE D C 20332		10. PROGRAM ELEMENT, PROJECT, TASK AREA & WORK UNIT NUMBERS 2307A3 17A3 61102F
14. MONITORING AGENCY NAME & ADDRESS (if different from Controlling Office) 12 119p.		12. REPORT DATE 11 May 79
		13. NUMBER OF PAGES 110
		15. SECURITY CLASS. (of this report) UNCLASSIFIED
		15a. DECLASSIFICATION/DOWNGRADING SCHEDULE
16. DISTRIBUTION STATEMENT (of this Report) Approved for public release; distribution unlimited.		
17. DISTRIBUTION STATEMENT (of the abstract entered in Block 20, if different from Report)		
18. SUPPLEMENTARY NOTES		
19. KEY WORDS (Continue on reverse side if necessary and identify by block number) FINITE-DIFFERENCE SOLUTIONS NONEQUILIBRIUM FLAT-PLATE BOUNDARY LAYERS NONEQUILIBRIUM SIDEWALL BOUNDARY LAYERS		
20. ABSTRACT (Continue on reverse side if necessary and identify by block number) Details are given of an implicit six-point finite-difference scheme for solving two-temperature chemical nonequilibrium laminar boundary-layer flows in ionizing argon. The analysis extends previous work by considering the radiation-energy loss and the chemical reactions in the plasma of the ionizing boundary layer. The variations of transport properties based on the known elastic-scattering cross-sections for an argon plasma across the boundary layer are considered. The effects of the chemical reactions, radiation-energy loss and the electric sheath on the boundary-layer structures are discussed. Both the flat-plate and the		

UNCLASSIFIED

SECURITY CLASSIFICATION OF THIS PAGE(When Data Entered)

shock-tube sidewall boundary-layer flows are analyzed and compared with interferometric data obtained using the UT^AIAS 10 cm x 18 cm Hypervelocity Shock Tube at shock Mach numbers $M_s \sim 13$ and ~ 16 at an initial argon pressure $p_0 \sim 5$ torr and temperature $T_0 \sim 300$ K. Fairly good agreement was obtained between analysis and experiment for both types of boundary layers.

UNCLASSIFIED

Qualified requestors may obtain additional copies from the Defense Documentation Center, all others should apply to the National Technical Information Service.

Conditions of Reproduction:

Reproduction, translation, publication, use and disposal in whole or in part by or for the United States Government is permitted.

Approved for public release; distribution unlimited.

AIR FORCE OFFICE OF SCIENTIFIC RESEARCH (AFSC)
NOTICE OF TRANSMITTAL TO DDC
This technical report has been reviewed and is
approved for public release IAW AFR 190-12 (7b).
Distribution is unlimited.
A. D. BLOSE
Technical Information Officer

FINITE-DIFFERENCE SOLUTIONS FOR NONEQUILIBRIUM LAMINAR BOUNDARY LAYERS
IN IONIZING-ARGON FLOWS

by

W. S. Liu

Submitted April, 1978

Accession For	
NTIS GRA&I	<input checked="checked" type="checkbox"/>
DDC TAB	<input type="checkbox"/>
Unannounced	<input type="checkbox"/>
Justification	
By	
Distribution/	
Availability Codes	
Dist	Available/or special

February, 1979

UTIAS Report No. 226
CN ISSN 0082-5255

Acknowledgements

I am pleased to express my thanks to Dr. I. I. Glass for his constructive review of my manuscript and many useful suggestions. The discussions on several experimental and theoretical aspects of the work held with Dr. I. I. Glass and Mr. B. T. Whitten are very much appreciated.

I wish to thank my wife, Alice, for her support and understanding during the preparation of this manuscript.

The financial assistance received from the Air Force Office of Scientific Research under Grant No. AF-AFOSR-77-3303 and from the National Research Council of Canada is acknowledged with thanks.

Summary

Details are given of an implicit six-point finite-difference scheme for solving two-temperature chemical nonequilibrium laminar boundary-layer flows in ionizing argon. The analysis extends previous work by considering the radiation-energy loss and the chemical reactions in the plasma of the ionizing boundary layer. The variations of transport properties based on the known elastic-scattering cross-sections for an argon plasma across the boundary layer are considered. The effects of the chemical reactions, radiation-energy loss and the electric sheath on the boundary-layer structures are discussed. Both the flat-plate and the shock-tube sidewall boundary layer flows are analyzed and compared with interferometric data obtained using the UTIAS 10 cm x 18 cm Hypervelocity Shock Tube at shock Mach numbers $M_s \sim 13$ and ~ 16 at an initial argon pressure $p_0 \sim 5$ torr and temperature $T_0 \sim 300$ K. Fairly good agreement was obtained between analysis and experiment for both types of boundary layers.

CONTENTS

	<u>Page</u>
Acknowledgements	11
Summary	111
Notation	vi
1. INTRODUCTION	1
1.1 General Considerations	1
1.2 Scope of Present Work	4
1.3 Basic Assumptions	4
1.4 Regions of Flow Near the Wall	5
2. BASIC EQUATIONS AND TRANSFORMATION	6
2.1 Boundary Layer Equations for Ionizing Monatomic Gases	6
2.2 Transformation of Boundary-Layer Equations	11
3. THERMAL PROPERTIES OF AN ARGON PLASMA	13
3.1 Elastic-Scattering Cross-Sections	13
3.2 Transport Properties of Ionizing Argon	14
3.3 Inelastic-Scattering Cross-Sections and Reaction-Rate Coefficients	15
4. BOUNDARY AND INITIAL CONDITIONS FOR BOUNDARY-LAYER FLOWS	18
4.1 Boundary Conditions	18
4.2 Compatibility Conditions	20
4.3 Solutions for Inviscid-Flow Region	23
4.4 Initial Conditions	23
5. FINITE-DIFFERENCE METHOD	24
5.1 Mathematical Considerations	24
5.2 Finite-Difference Equations	26
5.3 Accuracy and Stability	31
5.4 Transformation of Coordinates	32
6. FLAT-PLATE BOUNDARY-LAYER FLOWS IN IONIZING ARGON	33
6.1 General Considerations	33
6.2 Comparison of Theoretical and Experimental Results	35
7. SHOCK-TUBE SIDEWALL BOUNDARY-LAYER FLOWS IN IONIZING ARGON	38
7.1 General Considerations	38
7.2 Comparison of Theoretical and Experimental Results	39
8. DISCUSSIONS AND CONCLUSIONS	42

Page	CONTENTS	Page
44	REFERENCES	44
	APPENDICES:	
	A - DESCRIPTION OF COMPUTER PROGRAM	
	B - THERMODYNAMIC QUANTITIES	
	C - EXPRESSIONS OF FUNCTIONS $x_j^{(1)}$	
	D - EFFECTS OF CHEMICAL REACTIONS ON BOUNDARY LAYER	
	E - EFFECTS OF BOUNDARY LAYER ON SHOCK-WAVE STRUCTURE	
	F - COMPUTER PROGRAM BLEIG	

Notation

A_i	Coefficients of finite-difference equations, Eq. (75)
a_i	Constant value defined in Eq. (75)
B_i	Coefficients of finite-difference equations, Eq. (75)
b_i	Constant value defined in Eq. (75)
C	$\rho\mu/\rho_0\mu_0$, Eq. (24)
C_i	Coefficients of finite-difference equations, Eq. (75)
c_i	Constant value defined in Eq. (75)
C_p	$5/2 R$, Eq. (7)
D_a	Ambipolar-diffusion coefficient, Eq. (34)
D_i	Coefficients of finite-difference equations, Eq. (75)
D_{ai}	Atom-ion diffusion coefficient, Eq. (33)
d_i	Constant value defined in Eq. (75)
e	Electron charge, Eq. (8)
F	$\partial f/\partial \eta$ or u/u_0 , Eq. (68)
f	Stream function, $f = \int_0^{\eta} (u/u_0) d\eta$
\bar{g}	Gaunt factor, Eq. (8)
H	Total enthalpy, Eq. (7)
h	Planck constant, Eq. (8)
h_e	$\alpha C_p T_e$, Eq. (7)
i	Grid point in η -direction
j	Grid point in ξ -direction
k	$\Delta\eta_{i+1}/\Delta\eta_i$
k_B	Boltzmann constant
k_f	Forward reaction-rate coefficient, Eq. (10)

k_r	Reverse reaction-rate coefficient, Eq. (10)
M	Maximum value of j
m	Mass of particle
N	Maximum value of i
n	Number density
\dot{n}_e	Electron-number density production rate
p	Pressure
Pr	Prandtl number defined in Eq.(24)
Pr_e	Electron Prandtl number defined in Eq.(24)
q_c	Plasma conduction heat flux, Eq.(7)
q_d	Plasma diffusive heat flux, Eq.(7)
Q_{el}	Rate of thermal-energy transfer to electrons due to elastic collisions, Eq.(11)
Q_{inel}	Rate of thermal-energy transfer to electrons due to inelastic collisions, Eq.(12)
Q_R	Plasma radiation-energy loss, Eq.(8)
R	Gas constant, Eq.(7)
Sc	Schmidt number defined in Eq.(24)
S_{ab}^*	Excitational cross-section constant of particle a due to collision with particle b, Eq.(38)
T	Temperature
u	Velocity of plasma in x-direction
U_a	Defined in Eq.(32)
v	Velocity of plasma in y-direction
V_a	Ambipolar-diffusion velocity, Eq.(49)
V_i	Defined in Eq.(48)
$\langle V_e \rangle$	Defined in Eq.(49)
W	A function representing F , z , θ or Θ , Eq.(74)

x	Direction along the surface
y	Direction normal to the surface
z	α/α_0 , Eq. (24)
Z_{eff}	Effective nuclear charge, Eq. (8)

Greek symbols

α	Degree of ionization, Eq. (7)
β	Parameters defined in Eq. (24)
γ	$\rho_0 \mu_0 u_0$, defined in Eq. (76)
δ^*	Boundary-layer displacement thickness
ϵ	Kinetic energy of a particle in contour of mass coordinates, Eq. (38)
η	Transformed y-coordinate, Eq. (18)
θ	T_a/T_{a0} , Eq. (24)
Θ	T_e/T_{e0} , Eq. (24)
μ	Viscosity coefficient of plasma, Eq. (32)
ν_c	Cut-off frequency of plasma, Eq. (8)
ν_{ea}	Elastic collision-frequency due to electron-atom encounter, Eq. (11)
ν_{ei}	Elastic collision-frequency due to electron-ion encounter, Eq. (11)
ξ	Transformed x-coordinate, Eq. (18)
ρ	Density
σ	Scattering cross-section
τ	T_{e0}/T_{a0}
τ_u , etc.	Characteristic times, defined in Section 5.2
$\Delta\phi$	Potential difference between wall and plasma
λ	Weighting factor for finite-difference scheme
$\lambda_a, \lambda_i, \lambda_e$	Thermal-conductivity coefficients for atom, ion and electrons, respectively, Eqs. (35-37)
$\bar{\lambda}$	$\lambda_a + \lambda_i$

Subscripts and Superscripts

a	Atom
cri	Critical
e	Electron
eq	Equilibrium
f	Velocity
I	Ionization
i	Ion
s	Sheath
T_a	Atom temperature
T_e	Electron temperature
w	Wall
z	Degree of ionization
δ	Edge of boundary layer
o	Initial value of the shock front
'	$\partial/\partial\eta$
*	Excitation
η	$\partial/\partial\eta$
ξ	$\partial/\partial\xi$

1. INTRODUCTION

1.1 General Considerations

An understanding of boundary layer flows in partially ionized gases is helpful in designing successful spacecraft for re-entry into the Earth's atmosphere at hypersonic conditions. It also provides insight into the physical phenomena of interactions between solid surfaces and plasma flows. The presence of ions and electrons introduces new transport mechanisms and chemical reactions in the boundary layer. The magnitude of the various transport properties of an ionized gas can be markedly different from a perfect gas. Therefore, the boundary layers in an ionizing gas are generally more complex than those in nonionized-gas flows. Despite years of research, boundary-layer flows of partially-ionized gases are not fully understood experimentally and theoretically.

The character of the ionizing boundary layer problem was schematically described by Knöös (Ref. 1). The following characteristics are important in considering partially-ionized boundary-layer flows:

- (a) Transport properties
- (b) Interactions between moving plasma and metal surface
- (c) Atomic-collision processes
- (d) Chemical reactions
- (e) Radiation-energy transfer
- (f) Electromagnetic fields

The full boundary layer problem is exceedingly complex, and only a few cases have been treated by early investigators. Usually, some approximations are made to suit a given problem and to reduce the computation-time costs.

In general, a mixture of an ionizing gas is composed of molecules, atoms, molecular ions, atomic ions and electrons. However, since the dissociation energy is much less than the ionization energy, ionization can be considered to become appreciable only after dissociation is practically completed. Therefore, the mixture is assumed to be composed only of atoms, atomic ions and electrons. The presence of electrons in a gas introduces some features quite different from those encountered in chemical dissociations. For example, the collisional energy-transfer processes between electrons and heavy particles (atoms and ions) are relatively slow, giving rise to the possible situation that the electrons may have a temperature much different from that of the heavy particles. The extremely low mass of the electrons yields a species possessing a thermal conductivity that can be much greater than that of the other species. When such a gas is in contact with a cold surface, a space-charge sheath is formed which may affect the energy transfer to the surface. The electrons may have a higher temperature than the heavy particles near the cool surfaces. In such cases, the electrons make a greater contribution to the electrical and thermal conductivity than would be expected solely on the basis of their number density. Finally, the charged species are sensitive to electromagnetic fields yielding a possible method of controlling the energy transfer processes between electrons and ions. Therefore, the boundary-layer flows in ionizing gases are exceedingly more complex than in nonionized or dissociated gases.

The state of the mixture of atoms, ions and electrons is uniquely described by three independent state parameters: pressure, temperature and

degree of ionization. In general, the mixture of an ionizing gas is in a state of nonequilibrium, that is, both thermal nonequilibrium and chemical nonequilibrium. In thermal equilibrium, which in general cannot be expected to occur in a boundary-layer flow, the temperatures (T_a and T_e) of both heavy particles and electrons are equal. In chemical equilibrium, the degree of ionization α is immediately adjusted to its local equilibrium value, so that the degree of ionization can be given as a function of pressure p and temperature T via the Saha equation. In the frozen state, the electron number density production rate \dot{n}_e is equal to zero. The following models have been considered by a number of authors in solving ionizing boundary layer flows:

One-temperature equilibrium:	$T_e = T_a, \alpha = f(p, T_a)$
Two-temperature equilibrium:	$T_e \neq T_a, \alpha = f(p, T_e \text{ or } T_a)$
One-temperature frozen:	$T_e = T_a, \dot{n}_e = 0$
Two-temperature frozen:	$T_e \neq T_a, \dot{n}_e = 0$
One-temperature nonequilibrium:	$T_e = T_a, \dot{n}_e \neq 0$
Two-temperature nonequilibrium:	$T_e \neq T_a, \dot{n}_e \neq 0$

The thermodynamic quantities and the descriptions of equilibrium, frozen and nonequilibrium flows are given in Appendix B.

The following brief review may be helpful. Many investigators have treated weakly ionized, collision-dominated boundary layers. Their main aim was to study the effects produced on the electrical characteristics of Langmuir probes. Examples are the incompressible flow of a weakly ionized gas treated by Su and Lamb (Ref. 2) and the Couette-flow problem studied by Chung (Ref. 3). The kinetic theory of ionized-gas flows was used in the analysis. Recently, Chung, Talbot and Touryan (Ref. 4) have summarized the theoretical results for electric probes.

Based on thermal equilibrium in temperature and chemical reactions, Fay and Kemp (Ref. 5) have studied the heat transfer to a shock-tube end-wall from an ionized monatomic gas and Knöös (Ref. 1) generalized it to a simple thermal Rayleigh boundary layer in an equilibrium flow. Back (Ref. 6) studied the heat transfer through a one-temperature laminar boundary layer from a partially-ionized gas to a highly-cooled wall for frozen and equilibrium-flow models based on similar assumptions. A finite-difference method was applied by Blottner (Ref. 7) to a one-temperature nonequilibrium laminar boundary layer in ionizing air. Park (Ref. 8) analyzed the frozen and equilibrium flow over a flat plate and at an axisymmetric stagnation point based on similar and one-temperature models. Finson and Kemp (Ref. 9) extended the theory of Fay and Kemp to stagnation-point heat transfer. Using one-temperature and constant transport properties, the equilibrium, frozen and nonequilibrium solutions were obtained by Liu (Ref. 10) through an integral method.

For the two-temperature boundary layer, Sherman and Reshotko (Ref. 11) have obtained the electron temperature profiles for chemical-equilibrium flow based on similar solutions. Nishida and Matsuoka (Ref. 12) solved the similarity equations for frozen flow with constant transport properties. Analyses of flat-plate boundary layers in partially-ionized gases with thermal nonequilibrium and

recombination were investigated by Tseng and Talbot (Ref. 13) based on similar solutions and constant transport properties. Recently, Takano and Akamatsu (Ref. 14) used a finite-difference method to solve the shock-tube side-wall boundary-layer flow with constant transport properties. The thermal Rayleigh boundary layer flow for partially-ionized argon with varied transport properties were studied numerically and experimentally by Mansfeld (Ref. 15) for thermal and chemical nonequilibrium cases. Honma and Komuro (Ref. 16) studied an ionizing nonequilibrium boundary layer behind a moving shock wave by using a finite-difference scheme.

The numerical methods for solving the boundary layer equations can be divided into the following categories:

- (a) Local-similarity method
- (b) Integral method
- (c) Difference-differential procedure
- (d) Series-expansion method
- (e) Perturbation method
- (f) Finite-difference method

With the exception of the finite-difference scheme, all these techniques involve, in one way or another, the reduction of the nonlinear partial-differential equations to ordinary-differential equations. In the local-similarity method the history of the flow is ignored except insofar as it appears in the calculation of the variable x (or ξ), where x is the coordinate along the surface. This results in a set of ordinary-differential equations with two-point boundary conditions. In the integral method one or more assumptions are made regarding the profiles of the flow quantities. The equations used are obtained by taking suitable integrals of the boundary-layer equations across the boundary layer. The boundary-layer equations reduce to a system of ordinary-differential equations of the initial-value type. In the difference-differential procedure, the derivatives in the direction along the surface are replaced with finite-difference relations and the nonlinear partial-differential equations reduce to ordinary-differential equations with two-point boundary conditions. In the series-expansion method, the coefficients of a series in an x -dependent variable are obtained from a solution of ordinary-differential equations. The expansion variable depends on the external-flow conditions. The perturbation method is based on the concept that a perturbation of a known boundary-layer solution is considered and an expansion is carried out in terms of a parameter. A critical review of the early work up to 1969 was given by Blottner (Ref. 17).

Two difficulties exist in the analysis of ionizing boundary-layer flows: (1) the evaluation of the reaction-rate coefficients near the wall, (2) the boundary conditions for the degree of ionization and the electron temperature at the wall. First, near the wall, where the temperature of the heavy particles is in equilibrium with the wall temperature, the temperature of the heavy particles is very small compared with that at the edge of the boundary layer. Near the wall the electron-number density is also very low. In this low temperature and low electron-number-density domain, thermal ionization hardly occurs. Consequently, thermal transport processes will dominate. The reverse chemical-reaction-rate coefficients for atom-ion-electron and electron-ion-electron collisions are extremely large and difficult to evaluate in that domain. Second, the boundary conditions for the degree of ionization and the electron temperature at the wall are usually determined from the collision-free sheath theory. However, some authors, for example Mansfeld (Ref. 15), found that owing to the assumptions and incomplete description of the electric sheath a comparison of theoretical and experimental results would be

of questionable value. Careful experiments for electron-number density near the wall must be done in order to check the validity of the electric-sheath theory.

The difficulty in using the finite-difference method for an ionizing boundary layer lies in the stability of the scheme and in significant computation times. The stability criterion for the set of strongly-coupled nonlinear partial-differential equations with their boundary conditions of a mixed Neumann/Dirichlet type in the finite-difference scheme is difficult to evaluate. In order to avoid the difficulty of stability, Mansfeld (Ref. 15) applied the backward implicit method in the time-dependent one-dimensional Rayleigh problem. However, his program is near the maximum acceptable computation time. In the present two-dimensional boundary-layer flow, which is more complex than the Rayleigh boundary-layer flow, the stability criterion and computation time should be examined carefully.

Blottner (Ref. 17) mentioned that the iteration procedure for controlling the nonlinear terms is not required for a dissociated boundary-layer flow. However, when the variations of the transport properties across the boundary layer are taken into account in the ionizing boundary-layer equations, a successive iteration procedure is necessary in the present problem. This iteration scheme increases the computation time. Therefore, in the present calculation, the implicit six-point finite-difference method and nonequidistant step sizes are applied in order to decrease the computation time.

1.2 Scope of Present Work

The present paper gives the details of an implicit six-point finite-difference scheme for solving the nonlinear partial-differential equations of thermal and chemical-nonequilibrium boundary-layer flows in ionizing argon. The transport properties evaluated from known elastic-scattering cross-sections of the plasma are varied across the boundary layer. The radiation-energy loss of the plasma and the appropriate chemical reactions are both considered. The flat-plate and shock-tube sidewall boundary-layer flows are studied. The theoretical results are compared with interferometric measurements obtained in the UTIAS Hypervelocity Shock Tube for argon boundary layers on a flat plate and on the shock-tube sidewall behind a shock wave under close initial conditions.

In Chapter 2, the basic equations for laminar boundary-layer flows in partially-ionized monatomic gases are discussed and transformed. The basic assumptions are evaluated. The transport properties and chemical-reaction rates are considered using the known elastic and inelastic-scattering cross-sections for an argon plasma (see Chapter 3). The initial and boundary conditions are given in Chapter 4. The implicit six-point method of the finite-difference scheme is presented and discussed in Chapter 5. The analytical and experimental results are compared in Chapters 6 and 7 for flat-plate and shock-tube sidewall boundary-layer flows, respectively. Discussions and conclusions are given in Chapter 8. The explanation of the computer program is presented in Appendix A. The computer program is listed in Appendix F.

1.3 Basic Assumptions

In the present analysis, the following basic assumptions are used.

- (1) For a mixture of atoms, ions and electrons, it will be assumed that each species has a Maxwellian-velocity distribution with an appropriate temperature.

The governing equations for the plasma motion can be obtained from the Boltzmann equation by employing approximations to the distribution functions. One of the cases for which the equations are solvable is when the particles have a Maxwellian-velocity distribution. The assumption of a Maxwellian-velocity distribution can be justified when all the gradients in the macroscopic properties of the plasma are small and no external forces act on the plasma. In such a case the plasma flow is an isentropic flow, and it can be proven that the velocity distribution is Maxwellian. The condition that the velocity distribution for the electrons and ions is near a Maxwellian distribution is that the Larmor radius is much greater than the mean-free-path, or the elastic-collision frequency is to be large during the time-evolution process.

Under this assumption the evaluation of the binary-collision integrals in the macroscopic equations can be greatly simplified. This assumption should be valid for the region of the boundary layer except the sheath region adjacent to the wall where the electron and ion-number densities are very low.

(2) Only a singly ionized species is considered. The electron-number density can be assumed equal to the ion-number density. The plasma is quasi-neutral. Therefore, the effects of elastic and magnetic fields on the boundary-layer structure are neglected. The essential requirement for quasi-charge neutrality is that the Debye length is much smaller than the characteristic length of the problem (Ref. 18). The ambipolar character of the diffusion process results from this assumption providing that no electric currents cross the boundary.

The temperatures of heavy particles and electrons considered here are much smaller than the ionization temperature. Therefore the assumption that ions are singly ionized is valid in general. However, in the region adjacent to the wall, a space-charge sheath exists wherein the gas is no longer quasi-neutral. The sheath is composed of excess ions, yielding an electric field to repel electrons. Therefore special consideration of the sheath region is needed.

(3) The atom and ion temperatures are equal. Therefore, atoms and ions have the same velocity. This assumption can be justified since the mass of the ions is almost equal to that of atoms, and therefore only few collisions between atoms and ions are necessary to reach a common temperature. Jaffrin (Ref. 27) has investigated the structure of a steady plane shock in a partially ionizing gas using the Navier-Stokes equations. He showed that ion temperature is almost identical with atom temperature in the whole region. However, the collisional energy-transfer processes between electrons and heavy particles are relatively slow, giving rise to a situation that electrons may have a temperature much different from that of heavy particles. It is shown from the analysis of shock structure that electrons have a much lower temperature than the heavy particles in the ionization-relaxation zone. However, in a boundary layer, electrons may have a higher temperature than the heavy particles near the cool surfaces.

Additional assumptions made in the present analysis are described in Chapters 2 and 3.

1.4 Regions of Flow Near the Wall

As suggested by Dix (Ref. 18), three distinct regions exist near the wall: (1) Continuum-flow region; away from the wall, the gas is quasi-neutral, the ion-diffusion velocity is small, and the continuum equations are valid. The boundary-layer equations described in this report should be applicable. (2) Transition region; near the wall but not adjacent to it, the gas remains quasi-neutral,

but the ion-diffusion velocity is of the same order as the ion sound velocity. The continuum equations are not valid. (3) Sheath region; in the region adjacent to the wall, quasi-charge neutrality collapses near a catalytic boundary. In this so-called sheath region with thickness on the order of a Debye length, strong electric-field strengths are created in order to prevent the plasma from being broken down in a very short time. The sheath is composed of excess ions, yielding an electric field to repel electrons. The Boltzmann equation is required in the latter two regions.

For the flow conditions considered in the present analysis, the thicknesses of the transition and sheath regions are very small compared with the boundary-layer thickness. Since a major difficulty exists in the solution of the transition region, it is neglected and the solutions at the edge of the sheath region are regarded as the wall conditions of the boundary-layer flow.

The physical phenomena of the sheath region can be described as follows. Whenever a charged particle strikes an absorbing surface, this particle loses its charge by recombination on the surface. Thus, solid surfaces act as sinks for charged particles. Electrons have much larger thermal velocities than the ions. Consequently, per unit time more electrons are likely to strike the surface than the slower ions. As the electrons diffuse in the general direction of the surface, the slow ions retard the diffusion by setting up an electrostatic field. This process is called ambipolar diffusion, and the associated electric-potential field falls in the direction of the charge motion. Immediately next to the wall, the electron-number density becomes too low to carry the ions, and the potential of the surface and the ion-diffusion motion take over. Therefore, a sheath of high electric field exists. Two methods can be applied to the analysis of the sheath region: (1) the continuum-sheath theory, and (2) the collisionless-sheath theory. In the present analysis, the simpler method of collisionless-sheath theory is considered and described in Section 4.1.

2. BASIC EQUATIONS AND TRANSFORMATION

2.1 Boundary Layer Equations for Ionizing Monatomic Gases

A partially ionized monatomic gas or plasma is considered consisting of a mixture of atoms, ions and electrons. For each species the macroscopic balance equations can be expressed by using the plasma macroscopic properties, as shown below (Ref. 19),

$$\frac{\partial}{\partial t} [n_s \langle \phi_s \rangle] + \frac{\partial}{\partial x^j} [n_s \langle \phi_s V_s^j \rangle] = I(\phi_s) \quad (1)$$

where the quantity $\langle \phi_s \rangle$ is the average of the property ϕ_s , n_s is the number density of species s , $I(\phi_s)$ is the source term of property ϕ_s , and V_s is the total velocity of a particle of species s . The source term expresses the change in $\langle \phi_s \rangle$ as a result of both external influence (i.e., electric, magnetic and gravitational fields) and internal influence (i.e., chemical reactions, heat transfer, radiation, diffusion and viscosity). The continuity, momentum and energy equations are obtained by putting $\phi_s = m_s$, $m_s V_s^j$ and $1/2 m_s V_s^j V_s^j + \epsilon_{int}$ respectively, where m is the mass of particle and ϵ_{int} is the internal energy of particle.

The thermodynamic quantities used in this work are presented in Appendix B.

The general formulation of the gasdynamic conservation equations for individual species in a nonequilibrium partially ionized gas mixture has been discussed by Appleton and Bray (Ref. 20), Kaufman (Ref. 21), Grewal and Talbot (Ref. 22), Spitzer (Ref. 23) and Igra (Ref. 19).

Following the above considerations the basic equations for a boundary-layer flow of a partially ionized gas are given by

Continuity equation for plasma:

$$\frac{\partial}{\partial x} (\rho u) + \frac{\partial}{\partial y} (\rho v) = 0 \quad (2)$$

Momentum equation for plasma:

$$\rho u \frac{\partial u}{\partial x} + \rho v \frac{\partial u}{\partial y} = - \frac{\partial p}{\partial x} + \frac{\partial}{\partial y} \left(\mu \frac{\partial u}{\partial y} \right) \quad (3)$$

Energy equation for plasma:

$$\rho u \frac{\partial H}{\partial x} + \rho v \frac{\partial H}{\partial y} = - \frac{\partial}{\partial y} (q_c + q_d) + \frac{\partial}{\partial y} \left(\mu u \frac{\partial u}{\partial y} \right) - Q_R \quad (4)$$

Conservation equation for electron species:

$$\rho u \frac{\partial \alpha}{\partial x} + \rho v \frac{\partial \alpha}{\partial y} = - \frac{\partial}{\partial y} [\rho_i V_i] + m_a \dot{n}_e \quad (5)$$

Energy equation for electrons:

$$\rho u \frac{\partial h_e}{\partial x} + \rho v \frac{\partial h_e}{\partial y} = u \frac{\partial p_e}{\partial x} + v \frac{\partial p_e}{\partial y} - \frac{\partial}{\partial y} (q_{ce} + q_{de}) + V_i \frac{\partial p_e}{\partial y} + Q_{el} + Q_{inel} \quad (6)$$

with u, v as the velocities of the plasma in x, y directions, x coordinate along the body surface and y normal to it; ρ , plasma density; p , plasma pressure; μ , plasma-viscosity coefficient; H , total enthalpy of the plasma; q_c , plasma heat-conduction flux; q_d , plasma diffusive-energy flux; Q_R , plasma radiation-energy loss; α , degree of ionization; V_i , ion diffusion velocity relative to v ; m_a , mass of atom (or ion); \dot{n}_e , electron-number density production rate; h_e , electron specific enthalpy defined in Eq. (7); Q_{el} , rate of thermal energy given to free electrons by elastic collisions; Q_{inel} , inelastic energy-transfer rate; p_e , electron pressure; subscript e denotes electron encounter. The following quantities are applied in Eqs. (2)-(6):

$$\rho = m_a (n_a + n_e)$$

$$p = (n_a + n_e)k_B T_a + n_e k_B T_e$$

$$H = C_p(T_a + \alpha T_e) + RT_I \alpha + u^2/2$$

$$\alpha = n_e / (n_a + n_e)$$

$$q_c = -(\lambda_a + \lambda_i) \frac{\partial T_a}{\partial y} - \lambda_e \frac{\partial T_e}{\partial y}$$

$$q_d = \rho_i V_i (RT_I + C_p T_e)$$

$$\rho_i V_i = -\rho D_a \left[\frac{\partial \alpha}{\partial y} + \frac{\alpha(1-\alpha)}{1+\alpha(T_e/T_a)} \frac{\partial}{\partial y} \left(\frac{T_e}{T_a} \right) \right]$$

(7)

$$h_e = \alpha C_p T_e$$

$$C_p = \frac{5}{2} R$$

$$R = k_B / m_a$$

$$q_{ce} = -\lambda_e \frac{\partial T_e}{\partial y}$$

$$q_{de} = C_p T_e \rho_i V_i$$

$$p_e = n_e k_B T_e$$

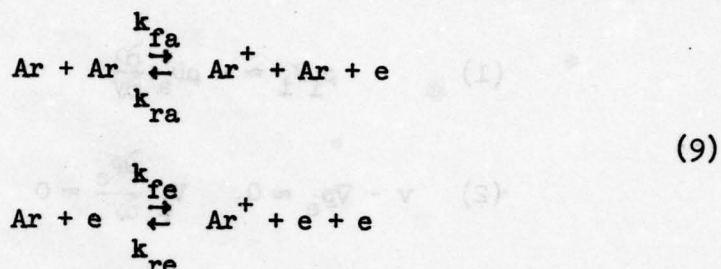
where subscripts a, i and e denote atom, ion and electron, respectively; T, temperature; T_I , ionization temperature; n, number density; R, gas constant; λ , thermal conductivity coefficient, D_a , ambipolar-diffusion coefficient; k_B , Boltzmann constant.

The rate of radiant energy loss Q_R of a plasma consists of the rates of energy loss by continuum radiation and by line radiation. In order to simplify the calculation, the rate of the line radiant-energy loss for the argon plasma is assumed equal to its continuum radiation-energy loss. This assumption has been discussed in Refs. 24 and 25. Based on the assumption of local-temperature equilibrium, Q_R is given by

$$Q_R = \frac{128\pi^{3/2} e^6}{3\sqrt{6} m_e^{3/2} c^3 h \sqrt{k_B}} \frac{n_e^2}{\sqrt{T_e}} (h\nu_c + k_B T_e) \bar{g} Z_{eff}^2 \quad (8)$$

with e, electron charge; h, Planck constant; c, speed of light; ν_c , cut-off frequency; \bar{g} , Gaunt factor; Z_{eff} , effective nuclear charge.

(2f) It has been shown that excitation to the first state is rate-controlling for the overall ionization process. We assume that atoms in the ground level are excited to the first-excitation level by collision with other particles, then excited atoms are ionized by subsequent collisions. The rates of reaction among levels higher than the first are assumed to be in thermal equilibrium with the electrons in the entire flow. The following reactions are considered for the collisional-ionization processes:



with k_f and k_r as forward and backward-rate coefficients.

Based on the two-temperature two-step model of Hoffert and Lien (Ref. 26), the electron-number density production rate \dot{n}_e can be written as

$$\dot{n}_e = (\dot{n}_e)_a + (\dot{n}_e)_e \quad (10)$$

where $(\dot{n}_e)_a$ and $(\dot{n}_e)_e$ denote the net electron number density production rates by atom-atom collision and electron-atom collision, respectively. The following equations are used for the electron number density production rates:

$$\begin{aligned} (\dot{n}_e)_a &= k_{fa} n_a^2 - k_{ea} n_a n_e^2 \\ (\dot{n}_e)_e &= k_{fe} n_a n_e - k_{re} n_e^3 \end{aligned} \quad (10a)$$

The elastic energy-transfer rate Q_{el} is the sum of the rates of thermal energy given to the free electrons by electron-atom and electron-ion elastic collisions (Ref. 27):

$$Q_{el} = 3n_e \left(\frac{m_e}{m_a} \right) (v_{ea} + v_{ei}) k_B (T_a - T_e) \quad (11)$$

where v_{ea} and v_{ei} are elastic-collision frequencies due to electron-atom and electron-ion encounters, respectively.

The inelastic energy-transfer rate Q_{inel} is the sum of the rates of thermal energy given to the free-electrons by electron-atom and electron-ion-electron inelastic collisions and by bremsstrahlung. The latter is neglected in the boundary-layer flow since it is small compared with the former. For the two-step model, Q_{inel} is given by,

$$Q_{inel} = -k_B T_I (\dot{n}_e)_e \quad (12)$$

where the term for the creation energy of electron due to atom-atom ionization collisions is very small and can be neglected in inviscid and viscous flows.

In order to simplify the present analysis, two approximations are made for the boundary-layer flows:

$$(1) \quad \rho_i V_i \approx -\rho D_a \frac{\partial \alpha}{\partial y} \quad (13)$$

$$(2) \quad v \cdot \nabla p_e \approx 0, \quad V_i \frac{\partial p_e}{\partial y} \approx 0$$

Approximation (1) has been widely accepted by many authors (for example, Refs. 12 and 28 in the analysis of two-temperature boundary-layer flows in ionizing gases. Approximation (2) has been used by Chung and Mullen (Ref. 28) and Takano and Akamatsu (Ref. 14) since these terms are very small compared with others on the RHS of Eq. (6). However, in the analysis of inviscid flow for ionizing gases (for example, the analysis of shock-wave structure given in Refs. 24 and 25, approximation (2) should not be made.

Under these approximations, the total energy equation, Eq. (4), for the plasma becomes

$$\begin{aligned} \rho u \frac{\partial H}{\partial x} + \rho v \frac{\partial H}{\partial y} &= \frac{\partial}{\partial y} \left(\bar{\lambda} \frac{\partial T_a}{\partial y} \right) + \frac{\partial}{\partial y} \left(\lambda_e \frac{\partial T_e}{\partial y} \right) \\ &+ \frac{\partial}{\partial y} \left[\rho D_a (RT_I + C_p T_e) \frac{\partial \alpha}{\partial y} \right] + \frac{\partial}{\partial y} \left(\mu u \frac{\partial u}{\partial y} \right) - Q_R \end{aligned} \quad (14)$$

where $\bar{\lambda} = \lambda_a + \lambda_i$.

The conservation equation for electron species, Eq. (5), becomes

$$\rho u \frac{\partial \alpha}{\partial x} + \rho v \frac{\partial \alpha}{\partial y} = \frac{\partial}{\partial y} \left(\rho D_a \frac{\partial \alpha}{\partial y} \right) + m_a \dot{n}_e \quad (15)$$

Using Eq. (15), the electron-energy equation, Eq. (6), can be rewritten as

$$\begin{aligned} C_p \alpha \left[\rho u \frac{\partial T_e}{\partial x} + \rho v \frac{\partial T_e}{\partial y} \right] &= \frac{\partial}{\partial y} \left(\lambda_e \frac{\partial T_e}{\partial y} \right) + \rho D_a \frac{\partial \alpha}{\partial y} \frac{\partial}{\partial y} (C_p T_e) \\ &- Q_{el} - (k_B T_I + \frac{5}{2} k_B T_e) (\dot{n}_e)_e - \frac{5}{2} k_B T_e (\dot{n}_e)_a \end{aligned} \quad (16)$$

The total-enthalpy equation, Eq. (14), can be rewritten in terms of T_a by using Eqs. (3), (15) and (16):

$$c_p \left[\rho u \frac{\partial T_a}{\partial x} + \rho v \frac{\partial T_a}{\partial y} \right] = u \frac{dp}{dx} + \frac{\partial}{\partial y} \left(\bar{\lambda} \frac{\partial T_a}{\partial y} \right) + \mu \left(\frac{\partial u}{\partial y} \right)^2 - Q_{el} - k_B T_I (\dot{n}_e)_a - Q_R \quad (17)$$

The basic equations for the boundary-layer flows are given by Eqs. (2), (3), (15), (16) and (17) with five unknowns: u , v , α , T_a and T_e . The boundary conditions of these equations are discussed in Chapter 4.

2.2 Transformation of Boundary-Layer Equations

The similarity transformation coordinates are applied:

$$\xi(x) = \int_0^x \rho_\delta u_\delta \mu_\delta dx$$

$$\eta(x,y) = \frac{u_\delta}{\sqrt{2\xi}} \int_0^y \rho dy \quad (18)$$

where the subscript δ denotes the edge of the boundary layer.

From Eq. (18),

$$\frac{d\xi}{dx} = \rho_\delta u_\delta \mu_\delta$$

$$\frac{\partial \eta}{\partial y} = \frac{\rho u_\delta}{\sqrt{2\xi}} \quad (19)$$

By employing the transformed continuity equation,

$$\rho v = - \left[\frac{d\xi}{dx} \frac{\partial \sqrt{2\xi} f}{\partial \xi} + \sqrt{2\xi} \frac{\partial \eta}{\partial x} \frac{\partial f}{\partial \eta} \right]$$

and the transformed convective operator,

$$\rho u \frac{\partial}{\partial x} + \rho v \frac{\partial}{\partial y} = \frac{\rho u_\delta}{2\xi} \frac{d\xi}{dx} \left[2\xi \left(\frac{\partial f}{\partial \eta} \frac{\partial}{\partial \xi} - \frac{\partial f}{\partial \xi} \frac{\partial}{\partial \eta} \right) - f \frac{\partial}{\partial \eta} \right]$$

the basic equations are transformed from the coordinates (x,y) to the coordinates (ξ,η) . Here,

$$f = \int_0^{\eta} \frac{u}{u_0} d\eta$$

The transformed equations for momentum, electron species, atom temperature and electron temperature are

$$[Cf'']' + ff'' + \beta_f \left[\frac{\rho_0}{\rho} - f'^2 \right] = 2\xi \left[f' \frac{\partial f'}{\partial \xi} - \frac{\partial f}{\partial \xi} f'' \right] \quad (20)$$

$$\left[\frac{C}{Sc} z' \right]' + fz' - \beta_z zf' + \frac{2}{\rho_0 \mu_0 u_0^2} \frac{m_a \dot{n}_e}{\rho \alpha_0} = 2\xi \left[f' \frac{\partial z}{\partial \xi} - \frac{\partial f}{\partial \xi} z' \right] \quad (21)$$

$$\begin{aligned} \left[\frac{C}{Pr} \theta' \right]' + f\theta' + \frac{u_0^2}{C_p T_a \delta} Cf''^2 - \beta_{T_a} \theta f' - \beta_f \frac{u_0^2}{C_p T_a \delta} \frac{\rho_0}{\rho} f' \\ - \frac{2\xi}{\rho_0 \mu_0 u_0^2} \frac{Q_{el} + k_{BI} T_I (\dot{n}_e)_a + Q_R}{\rho C_p T_a \delta} = 2\xi \left[f' \frac{\partial \theta}{\partial \xi} - \frac{\partial f}{\partial \xi} \theta' \right] \quad (22) \end{aligned}$$

$$\begin{aligned} \left[\frac{C}{Pr_e} \theta' \right]' + \frac{C}{Sc} \alpha_0 z' \theta' + \alpha_0 z f \theta' - \beta_{T_e} \alpha_0 z f' \theta \\ + \frac{2\xi}{\rho_0 \mu_0 u_0^2} \frac{Q_{el} - (k_{BI} + \frac{5}{2} k_{Be}) (\dot{n}_e)_e - \frac{5}{2} k_{Be} (\dot{n}_e)_a}{\rho C_p T_e \delta} \\ = 2\xi \alpha_0 z \left[f' \frac{\partial \theta}{\partial \xi} - \frac{\partial f}{\partial \xi} \theta' \right] \quad (23) \end{aligned}$$

where the prime denotes $\partial/\partial\eta$ and the following definitions are used:

$$\begin{aligned} f' &= \frac{u}{u_0} & C &= \frac{\rho \mu}{\rho_0 \mu_0} \\ z &= \frac{\alpha}{\alpha_0} & Sc &= \frac{\mu}{\rho D_a} \\ \theta &= \frac{T_a}{T_{a\delta}} & Pr &= \frac{\mu C_p}{\lambda} \\ \theta &= \frac{T_e}{T_{e\delta}} & Pr_e &= \frac{\mu C_p}{\lambda_e} \end{aligned} \quad (24)$$

Contd...

$$\begin{aligned}
 \beta_f &= \frac{2\xi}{u_0} \frac{du_0}{d\xi} & \beta_{T_a} &= \frac{2\xi}{T_{a0}} \frac{dT_{a0}}{d\xi} & (24) \\
 \beta_z &= \frac{2\xi}{\alpha_0} \frac{d\alpha_0}{d\xi} & \beta_{T_e} &= \frac{2\xi}{T_{e0}} \frac{dT_{e0}}{d\xi} & \text{Contd.}
 \end{aligned}$$

We note that solutions of Eqs. (20)-(23) are strongly dependent on the thermal properties of the ionizing gas. The transport properties are calculated from the elastic-scattering cross-sections and the chemical-reaction-rate coefficients are calculated from the inelastic-scattering cross-sections for the ionizing gas. In the following chapter, the thermal properties of ionizing argon are discussed.

3. THERMAL PROPERTIES OF AN ARGON PLASMA

3.1 Elastic-Scattering Cross-Sections

The elastic-scattering cross-sections are used in determining the transport properties of ionizing gases. They will be evaluated here from experimental results for argon. The average atom-atom elastic-collision cross-section σ_{aa} is obtained from the values of the viscosity coefficient given by Amdur and Mason (Ref. 29). At high temperature $\mu \approx 31 \times 10^{-7} T_a^{3/4}$ g/cm-sec, which corresponds to

$$\sigma_{aa} = 1.7 \times 10^{-14} / T_a^{0.25} \text{ cm}^2 \quad (25)$$

Experimental data compiled by Fay (Ref. 30) show that the average atom-ion elastic cross-section σ_{ai} is much bigger than the atom-atom elastic cross-section because of the charge-exchange mechanism. This cross-section decreases very slowly with the atom (or ion) temperature and will be taken as

$$\sigma_{ai} = 2.454 \times 10^{-14} / T_a^{0.09} \text{ cm}^2 \quad (26)$$

The average momentum-transfer cross-section between electrons and atoms σ_{ea} for argon was calculated by Devoto (Ref. 31) using the momentum-transfer cross-section determined by Frost and Phelps (Ref. 32). An approximate value of σ_{ea} for argon by curve fitting is

$$\sigma_{ea} = \begin{cases} (0.713 - 4.5 \times 10^{-4} T_e + 1.5 \times 10^{-7} T_e^2) \times 10^{-16} \text{ cm}^2 & \text{for } T_e < 3000 \text{ K} \\ (-0.488 + 3.96 \times 10^{-4} T_e) \times 10^{-16} \text{ cm}^2 & \text{for } T_e \geq 3000 \text{ K} \end{cases} \quad (27)$$

The average momentum-transfer cross-section between electrons and electrons σ_{ee} can be obtained by assuming the relative kinetic energy of

electrons equal to $1.5 k_B T_e$ in the Coulomb scattering cross-section:

$$\sigma_{ee} = \frac{2\pi e^4}{9(k_B T_e)^2} \ln \left(\frac{9k_B^3 T_e^3}{4\pi e^6 n_e} \right) \quad (28)$$

Note that if the above assumption does not apply, one may obtain the following form by using the Maxwellian distribution in the screened Coulomb-scattering cross-section:

$$\sigma_{ee} = \frac{\pi e^4}{4(k_B T_e)^2} \ln \left(\frac{9k_B^3 T_e^3}{4\pi e^6 n_e} \right) \quad (29)$$

Similarly, the average elastic-scattering cross-section between ions and ions, σ_{ii} is given by

$$\sigma_{ii} = \frac{\pi e^4}{4(k_B T_a)^2} \ln \left(\frac{9k_B^3 T_a^3}{4\pi e^6 n_e} \right) \quad (30)$$

Since $T_e/m_e \gg T_a/m_a$, the electron temperature is the relevant temperature in the calculation of ion-electron collision cross-section, therefore,

$$\sigma_{ei} = \sigma_{ee} \quad (31)$$

3.2 Transport Properties of Ionizing Argon

The kinetic theory of gases provides a means of estimating the transport coefficients of a partially-ionized gas. In this section, transport properties of partially-ionized argon are considered as based on the mixture rule of Fay and Kemp (Ref. 5).

The viscosity of plasma can be calculated as

$$\mu = \frac{5\pi}{32} \frac{m_a U_a}{\sigma_{aa}} \frac{1 + \frac{\alpha}{1-\alpha} \frac{\sigma_{ai}}{\sigma_{aa}}}{1 + \frac{\alpha}{1-\alpha} \frac{\sigma_{ai}}{\sigma_{aa}} + \frac{\alpha}{1-\alpha} \frac{\sigma_{ii}}{\sigma_{aa}}} \quad (32)$$

where

$$U_a = \left(\frac{8k_B T_a}{\pi m_a} \right)^{1/2}$$

is the mean thermal speed of the atoms. The electrons make no contribution to the viscosity because of their extremely low mass compared with atoms and ions.

The ambipolar diffusion coefficient D_a is defined in terms of the atom-ion diffusion coefficient D_{ai} by

$$D_a \approx \frac{2}{1 + \alpha} D_{ai} \quad (33)$$

or approximately as

$$D_a \approx \frac{0.833}{n_e + n_a} \sqrt{\frac{\pi k_B T_a}{m_a}} / \sigma_{ai} \quad (\text{cm}^2/\text{sec}) \quad (34)$$

where the contribution of the electron temperature due to electron-ion collision is negligible owing to the small electron mass.

The thermal conduction coefficients for atoms, ions and electrons may be written as (Ref. 27)

$$\lambda_a = \frac{75k_B}{64\sigma_{aa}} \left(\frac{\pi k_B T_a}{m_a} \right)^{1/2} \left[1 + \frac{n_e \sigma_{ai}}{n_a \sigma_{aa}} \right]^{-1} \quad (35)$$

$$\lambda_i = \frac{75k_B}{64\sigma_{ai}} \left(\frac{\pi k_B T_a}{m_a} \right)^{1/2} \left[1 + \frac{n_e \sigma_{ii}}{n_a \sigma_{ai}} \right]^{-1} \quad (36)$$

$$\lambda_e = \frac{75k_B}{64\sigma_{ee}(1 + \sqrt{2})} \left(\frac{\pi k_B T_e}{m_e} \right)^{1/2} \left[1 + \frac{\sqrt{2} n_a \sigma_{ea}}{(1 + \sqrt{2}) n_e \sigma_{ee}} \right]^{-1} \quad (37)$$

3.3 Inelastic-Scattering Cross-Sections and Reaction-Rate Coefficients

The forward-rate coefficient k_f , Eq.(10), can be obtained from kinetic theory by computing the collision rate between two particles. The calculation requires knowledge of the dependence of the inelastic-collision cross-sections for the first and higher excitation steps on incident energy. For a two-step model considered here, a knowledge of the energy dependence of the cross-section for the first excited state is required. Since only the energy dependence of inelastic cross-sections near the threshold energy is important in the calculation of the rate coefficients, some knowledge about the energy dependence of inelastic cross-sections near the threshold is required. The inelastic cross-sections thus obtained are often expressed in terms of the following relation:

$$\sigma^*(\epsilon) = \sigma_0 \left(1 - \frac{\epsilon^*}{\epsilon} \right)$$

where σ_0 is a constant and ϵ^* is the threshold energy.

Nevertheless, by making use of Wigner's R-matrix theory, Eu and Liu (Ref. 33) have obtained a general form for leading threshold behaviour of inelastic cross-sections in the form

$$\sigma^*(\epsilon) = \sigma_0 \left(1 - \frac{\epsilon^*}{\epsilon} \right)^{1/2}$$

which fits the experimental data fairly well within the experimental errors.

For the present analysis, a reasonably good approximation to this cross-section is given by the linear relationship:

$$\sigma_{ab}^*(\epsilon) = S_{ab}^*(\epsilon - \epsilon^*) \text{ for } \epsilon \geq \epsilon^* \quad (38)$$

where ϵ is the kinetic energy (in centre-of-mass coordinates) of particle b (b can be atom or electron), ϵ^* is the first excitation energy of particle a, and S_{ab}^* is the first-excitation collision cross-section slope.

The forward rate coefficient appearing in Eq. (10) can be written as,

$$k_{fb}(T_b) = S_{ab}^* \left[\frac{32}{\pi} \left(\frac{m_a + m_b}{m_a m_b} \right) \right]^{1/2} (k_B T_b)^{1/5} \left(\frac{T^*}{2T_b} + 1 \right) \exp(-T^*/T_b) \quad (39)$$

where T^* is the first excitation temperature of particle a, and this rate coefficient must be divided by two for like-like particle collisions.

From a comparison of theoretical and experimental results for argon shock-wave structure, we found (Ref. 24) that $S_{aa}^* = 1.0 \times 10^{-19} \text{ cm}^2/\text{eV}$. A more recent electron-atom excitation cross-section constant $S_{ae}^* = 4.9 \times 10^{-18} \text{ cm}^2/\text{eV}$ for argon obtained by Zapesochnyi and Felston (Ref. 34) is used here. Therefore, k_{fa} and k_{fe} yield:

$$k_{fa}(T_a) = 1.4 \times 10^{-20} T_a^{1.5} \left(\frac{T^*}{T_a} + 2 \right) e^{-T^*/T_a} (\text{cm}^3/\text{sec}) \quad (40)$$

$$k_{fe}(T_e) = 2.63 \times 10^{-16} T_e^{1.5} \left(\frac{T^*}{T_e} + 2 \right) e^{-T^*/T_e} (\text{cm}^3/\text{sec}) \quad (41)$$

Hoffert and Lien (Ref. 26) used a chemical equilibrium concept for the present chemical-nonequilibrium case to determine k_{ra} and k_{re} . However, for low temperatures these results are not valid and the ionic-recombination theory based on the classical electron-impact cross-section is needed. In order to avoid the difficulty of determination of the reverse reaction-rate coefficients, a critical temperature T_c is defined which separates the high and low-temperature regions. This critical temperature can be obtained by ensuring the continuity of the rate coefficients at T_c . For the electron-catalyzed reactions, Hinnov and Hirschberg (Ref. 35) have obtained an empirical relation for the reverse reaction-rate coefficient at low temperature ($T_e < 4000 \text{ K}$). The following reverse reaction-rate coefficient k_{re} for electron-

catalyzed reactions is used,

$$k_{re}(T_e) = \begin{cases} 9.03 \times 10^{-33} (T^*/T_e + 2) e^{(T_I - T^*)/T_e} \text{ cm}^6/\text{s} & \text{for } T_e \geq T_c \\ 1.09 \times 10^{-8} T_e^{-4.5} \text{ cm}^6/\text{s} & \text{for } T_e \leq T_c \end{cases} \quad (42)$$

where $T_c \sim 3100$ K.

For the atom-catalyzed reactions, a similar procedure can be applied. However, there is no available empirical relation for k_{ra} at temperatures T_a below 3000 K. At the same time, the chemical equilibrium concept used to determine k_{ra} by Hoffert and Lien (Ref. 26) is in serious error for the case where the electron temperature is considerably different from the atom temperature. In order to avoid a significantly large value of k_{ra} at low atom temperature, the following forms are applied (Glass and Liu, Ref. 24)

$$k_{ra}(T_a) = \begin{cases} 4.83 \times 10^{-37} (T^*/T_a + 2) e^{(T_I - T^*)/T_a} \text{ cm}^6/\text{s} & \text{for } T_a \geq T_c \\ 4.83 \times 10^{-37} (T^*/T_c + 2) e^{(T_I - T^*)/T_c} \text{ cm}^6/\text{s} & \text{for } T_a < T_c \text{ it has a constant value} \end{cases} \quad (43)$$

The physical meaning of the cut-off of k_{ra} at low temperature is that at low T_a the reverse atom-atom reaction rate is frozen at some particular rate and the re-excitation from the first excited state is not rate-controlling for atom-atom collisions. In general, the reaction rates due to atom-atom collisions are very small compared with those due to electron-atom collisions for atom temperature below about 15,000 K. Therefore, the atom-catalyzed reactions can be neglected for $T_a \leq 15,000$ K, in a flat-plate boundary-layer analysis where the flow has cooled significantly. However, for the case of a shock-tube sidewall boundary layer near the shock front where the atom temperature is large ($\sim 25,000$ K), atom-catalyzed reactions are more important than the electron-catalyzed reactions and k_{ra} must be retained. Byron et al (Ref. 36) have shown that for the low-temperature case, de-excitation from other than the first-excited state can be rate controlling in the recombination process. For the present two-step model, the approximation made in Eq. (43) is necessary in order to avoid the unknown physical effects due to a very large value of k_{ra} . It is also worth noting that a large value of k_{ra} destabilizes the finite-difference scheme.

Another method for evaluating the rate of atom-catalyzed reactions is to cut off k_{ra} and to limit the rate of recombination reaction of atom-atom

collision at some particular value. The following equation can be applied:

$$\begin{aligned}
 (\dot{n}_e)_a &= k_{fa} n_a^2 - k_{ra} n_a n_e^2 & \text{if } (\dot{n}_e)_a > 0 \\
 &= 0 & \text{if } (\dot{n}_e)_a < 0
 \end{aligned}
 \tag{44}$$

4. BOUNDARY AND INITIAL CONDITIONS FOR BOUNDARY-LAYER FLOWS

4.1 Boundary Conditions

The boundary conditions for Eqs. (2)-(6) are

$$\begin{aligned}
 y = 0: \quad & u = u_w \\
 & v = 0 \\
 & T_a = T_w \text{ (or } \partial T_a / \partial y = 0 \text{ for zero heat transfer)} \\
 y \rightarrow \infty: \quad & u = u_\infty \\
 & \alpha = \alpha_\infty \\
 & T_a = T_{a\infty} \\
 & T_e = T_{e\infty}
 \end{aligned}
 \tag{45}$$

where the wall values u_w and T_w are usually given. The other values u_∞ , α_∞ , $T_{a\infty}$ and $T_{e\infty}$ are determined from the inviscid-flow region (see Section 4.3).

The boundary conditions, Eq. (45), for the transformed equations, Eqs. (20)-(23), are

$$\begin{aligned}
 \eta = 0: \quad & f = 0 \\
 & f' = u_w / u_\infty \\
 & \theta = T_w / T_{a\infty} \text{ (or } \theta' = 0 \text{ for zero heat transfer)} \\
 \eta \rightarrow \infty: \quad & f' = 1 \\
 & z = 1 \\
 & \theta = 1 \\
 & \Theta = 1
 \end{aligned}
 \tag{46}$$

The other required boundary conditions are z and θ at the wall; these can be obtained from the following methods:

(1) Wall-Sheath Properties:

For the case in which the wall is at floating potential, the first equation is obtained from Langmuir-probe theory for a Maxwellian distribution of electrons:

$$\frac{n_{es} \langle V_e \rangle}{4} \exp \left(- \frac{e\Delta\phi}{k_B T_{es}} \right) - n_{es} e V_i = 0 \quad (47)$$

where $\langle V_e \rangle = (8k_B T_{es}/\pi m_e)^{1/2}$, $V_i = (k_B T_{es}/m_a)^{1/2}$, $\Delta\phi$ is the potential difference between wall and plasma and subscript s denotes the value evaluated at the sheath edge.

The second equation is the continuity of mass flow of ions at the outer edge of the sheath:

$$\rho_s D_{as} \left(\frac{\partial \alpha}{\partial y} \right)_s = \rho_s \alpha_s V_i \quad (48)$$

The energy equation at the edge of the sheath is

$$\left[\lambda_B \frac{\partial T_e}{\partial y} \right]_s - [\rho \alpha V_a n_e]_s = (2k_B T_{es} + e\Delta\phi) \frac{n_{es} \langle V_e \rangle}{4} \exp \left(- \frac{e\Delta\phi}{k_B T_{es}} \right) \quad (49)$$

where V_a is the ambipolar-diffusion velocity.

From Eqs. (47) and (48) we obtain

$$\theta'_w = \frac{2}{5} \left(\frac{Pr_e}{Sc} \right)_w \left[- \frac{1}{2} \theta_w + \frac{e\Delta\phi}{k_B T_{e0}} \right] \alpha_\delta z'_w \quad (50)$$

and Eq. (49) becomes

$$z'_w = (Sc)_w \frac{\sqrt{2\pi}}{\mu_w} \frac{V_{i0}}{u_\delta} z_w \theta_w^{1/2} \quad (51)$$

where $V_{i0} = (k_B T_{e0}/m_a)^{1/2}$ and $e\Delta\phi/k_B T_{e0} = \ln(m_a/2\pi m_e)^{1/2} \theta_w$.

This model, based on continuity at the sheath edge, was widely used by many authors, for example, Camac and Kemp (Ref. 37), Dix (Ref. 18), Nishida and Natsuoka (Ref. 12), Sherman et al (Ref. 11) and Mansfeld (Ref. 15). However, Mansfeld (Ref. 15) mentioned that the artificial boundary condition used for the two-temperature equilibrium model leads to values of n_e near the wall which seem to be in much better agreement with the experimental results than the values obtained from an electric-sheath consideration. He concluded that the validity of the boundary condition for z and θ at the wall derived from a presently incomplete description of the sheath is still unknown.

(2) Catalytic Wall Model

By analogy with the dissociated boundary-layer flow, the wall is assumed to be a catalytic wall when an equilibrium composition is used at the wall. For a one-temperature equilibrium model where $T_{aw} \approx 300$ K, the boundary condition for z at the wall is approximately given by

$$z_w \approx 0$$

For a two-temperature equilibrium catalytic wall model, z_w is given by

$$z_w = g$$

where g is a constant value.

For a cooled-wall case with a wall sheath model, Takano and Akamatsu (Ref. 14) have shown that

$$z_w \sim 0 (10^{-2})/\sqrt{Re}$$

$$\theta'_w \sim 0 (10^{-4})$$

where Re is the Reynolds number.

We also note that Nishida and Matsuoka (Ref. 12) have shown that the slope of the electron temperature at the wall is almost equal to zero. Mansfield (Ref. 15) has obtained the following results even when x is very small:

$$z_w \approx 0 \quad (52a)$$

$$\theta'_w \approx 0 \quad (52b)$$

In order to obtain better agreement between theory and experiment, Tseng and Talbot (Ref. 13) have used a measured value of z_w as the wall boundary condition:

$$z_w = 0.02$$

4.2 Compatibility Conditions

At the edge of the boundary layer, the following boundary conditions must be satisfied:

$$f'' = 0$$

$$z' = 0$$

$$\theta' = 0$$

(53)

$$\theta' = 0$$

By using the above boundary conditions, the compatibility conditions at $\eta \rightarrow \infty$ can be obtained from Eqs. (20)-(23):

$$\beta_f = - \frac{2\xi}{\rho_\delta u_\delta^2} \frac{dp_\delta}{d\xi}$$

$$\beta_z = \frac{2\xi}{\rho_\delta \mu_\delta u_\delta^2} \frac{m_a \dot{n}_e}{\rho_\delta \alpha_\delta}$$

(54)

$$\beta_{T_a} = - \beta_f \frac{u_\delta^2}{C_p T_a \delta} - \frac{2\xi}{\rho_\delta \mu_\delta u_\delta^2} \frac{Q_{e1} + k_{B I}^T (\dot{n}_e)_a + Q_R}{\rho_\delta C_p T_a \delta}$$

$$\beta_{T_e} = \frac{2\xi}{\rho_\delta \mu_\delta u_\delta^2} \frac{Q_{e1} - \left(k_{B I}^T + \frac{5}{2} k_{B e \delta}^T \right) (\dot{n}_e)_e - \frac{5}{2} k_{B e \delta}^T (\dot{n}_e)_a}{\rho_\delta C_p T_e \delta \alpha_\delta}$$

These conditions must be satisfied in the calculations in order to avoid a discontinuity in the gradients of the dependent variables at the edge of the boundary layer.

The value $dp_\delta/d\xi$ appearing in Eq. (54) must be obtained either from experiment or theory. The following considerations should be noted in the calculation:

(1) If the external effects (for example, an unsteady effect) or interactions (for example, the interactions with a shock wave or an expansion wave) occur in the inviscid-flow region, the value $dp_\delta/d\xi$ is obtained from the solution of the inviscid flow with these effects or interactions taken into account.

(2) If there is no external effect or interaction in the inviscid flow, another equation is needed to form a complete set of equations with five unknowns: $dp_\delta/d\xi$, β_f , β_z , β_{T_a} and β_{T_e} . This equation is obtained from the continuity equation of the plasma flow, Eq. (1),

$$\rho_{\delta} \frac{du_{\delta}}{d\xi} = - u_{\delta} \frac{d\rho_{\delta}}{d\xi}$$

where ρ_{δ} is related to p_{δ} by the equation of state,

$$p_{\delta} = \rho_{\delta} R (T_{a\delta} + \alpha_{\delta} T_{e\delta})$$

After some algebraic arrangement,

$$\beta_f = \frac{R}{A^* u_{\delta}^2} [T_{a\delta} \beta_{T_a} + \alpha_{\delta} T_{e\delta} \beta_{T_e} + \alpha_{\delta} T_{e\delta} \beta_z]$$

where β_{T_a} , β_{T_e} and β_z are calculated from Eq. (54) and

$$A^* = \frac{R}{u_{\delta}^2} (1 + \alpha_{\delta} \tau) T_{a\delta} - 1$$

$$\tau = \frac{T_{e\delta}}{T_{a\delta}}$$

It was shown by Blottner (Ref. 17) that a swallowing of the inviscid flow into the boundary layer is necessary in order to satisfy the compatibility conditions.

Since some approximations have been made in the boundary-layer equations with respect to the inviscid-flow equations, the values $dp_{\delta}/d\xi$, β_f , β_z , β_{T_a} and β_{T_e} obtained from the above equations should be slightly different from that obtained from the inviscid-flow region. If there is no approximation made in the boundary-layer equations, or the inviscid-flow equations are obtained directly by letting all $\partial/\partial y$ terms equal to zero in the boundary-layer equations, then the above method provides the same results that would be obtained from the inviscid-flow region.

A local-similarity method was applied by Brown and Mitchner (Ref. 38) in predicting the electron-temperature and electron-number-density profiles of a flat-plate boundary-layer plasma. They predicted that the electron temperature at the edge of the boundary layer is smaller than the atom temperature and explained it as due to the radiation-energy loss. However, it is clear that the compatibility conditions described above were not applied in their calculations. The electron temperature at the edge of the boundary layer must be calculated from the equations for the inviscid flow and not from the boundary-layer equations. In their calculation, in order to satisfy the boundary conditions at the edge of the boundary layer, Eq. (53), the values of the degree of ionization and the electron temperature at the edge were adjusted.

4.3 Solutions for Inviscid-Flow Region

The solutions for u_δ , $T_{a\delta}$, $T_{e\delta}$, α_δ and p_δ must be obtained from the equations for the inviscid-flow region. The quasi-one-dimensional equations for inviscid flow are obtained from Eqs. (1)-(5) by letting $\partial/\partial y = 0$:

$$\frac{d}{dx} (\rho u) = 0 \quad (55)$$

$$\rho u \frac{du}{dx} + \frac{dp}{dx} = 0 \quad (56)$$

$$\rho u \frac{dH}{dx} = -Q_R \quad (57)$$

$$\rho u \frac{d\alpha}{dx} = m_a \dot{n}_e \quad (58)$$

$$\rho u \frac{d}{dx} (\alpha C_p T_e) - u \frac{dp_e}{dx} = Q_{el} + Q_{inel} \quad (59)$$

Equations (55)-(59) have been solved by Glass and Liu (Ref. 24) for the shock-wave structure of ionizing argon and by Glass et al (Ref. 25) for a krypton shock-wave structure. The inviscid flow generated by a shock wave can be separated into two zones: (1) an ionization-relaxation zone and (2) a radiative-cooling zone. In the relaxation zone the elastic and inelastic-collision processes are important while in the radiative-cooling zone the radiation-energy loss is significant. Equations (55)-(59) provide a unified treatment applicable to both zones. However, from our numerical experience in solving the shock-wave structure, a complete solution for the radiative-cooling region requires a small step-size to be stable. As the plasma is nearly in equilibrium, values for u_δ , $T_{a\delta}$, $T_{e\delta}$, α_δ and p_δ in the cooling region can also be obtained approximately by solving only Eqs. (55)-(57) together with the Saha equation. Whitten (Ref. 39) has shown that the error in using a radiant equilibrium model is within 2% of the present nonequilibrium model.

4.4 Initial Conditions

The initial profiles are required for a finite-difference method. At the start of the boundary layer, $\xi = 0$, and the partial-differential equations become ordinary-differential equations. At $\xi = 0$: $\beta_f = \beta_{Ta} = \beta_{Te} = \beta_z = 0$, the following ordinary-differential equations are obtained from Eqs. (20)-(23):

$$[Cf'']' + ff'' = 0 \quad (60)$$

$$\left[\frac{C}{Sc} z' \right]' + fz' = 0 \quad (61)$$

$$\left[\frac{C}{Pr} \theta' \right]' + f' + \frac{u_\delta^2}{C_p T_{a\delta}} C f'^2 = 0 \quad (62)$$

$$\left[\frac{C}{Pr_e} \theta' \right]' + \frac{C}{Sc} \alpha_6 z' \theta' + \alpha_6 z f \theta' = 0 \quad (63)$$

Equations (60)-(63) with two-point boundary conditions can be solved using the usual iteration techniques (for example, the Newton-Raphson method). A subroutine BEGIN for solving Eqs. (60)-(63) is discussed and presented in Appendix F.

5. FINITE-DIFFERENCE METHOD

5.1 Mathematical Considerations

Numerical methods have developed rapidly in the last decade and solutions have now been found to many systems of simultaneous equations which, prior to the development of the digital computer, could not be solved because of the immense amount of calculation required. One of the most common numerical techniques for solving partial-differential equations is the finite-difference method, where the differential equations are replaced by a large number of difference equations, which are then solved by various algebraic methods.

The means of solving simultaneous algebraic equations can be divided into two general types called direct and indirect methods. Direct methods, which include elimination and matrix inversion techniques, require a finite number of steps to obtain an exact solution. Indirect methods theoretically require an infinite number of steps to obtain a solution but often can provide a sufficiently accurate solution in a much smaller number of steps than would be required with a direct method. The large number of difference equations resulting from partial-differential equations make direct methods impractical for solving a problem. For indirect methods, for example, the modified-Leibmann method, or over-relaxation method, are free from round-off errors and have the additional advantage that they can often be adapted to solve nonlinear equations. The direct methods are usually applied in the parabolic or hyperbolic-type partial differential equations having sides with an open boundary. The indirect methods are applied to elliptic-type equations with a closed boundary.

The finite-difference method for linear partial-differential equations has been well established. Unfortunately, methods for solving nonlinear algebraic equations are lagging far behind. Recently, because of the large number of physical and engineering problems which are described by nonlinear equations and the prospects which the computer offers for their solutions, the techniques for solving nonlinear algebraic equations has become an active field of mathematical research.

Two general methods have been developed for the solution of a set of simultaneous nonlinear algebraic equations. The first is called by Greenspan (Ref. 40) the nonlinear-Liebmann method, which involves linearizing the equations by putting known values into the nonlinear terms and requires iteration. The resultant set of linear algebraic equations is then solved by the extrapolated-Liebmann method or some other method. The process of iteration is continued until all the residuals are suitably small. The

second method, known either as the generalized Newton's method or nonlinear over-relaxation, is an iterative procedure where the grid is scanned in order. The generalized Newton's method is the faster of the two nonlinear methods according to Greenspan, but this is based only on examples and not a general mathematical theory.

The above iteration techniques are general mathematical methods developed to be applicable to a wide range of nonlinear differential equations. When the generalized Newton's method was applied to some engineering problems, it was found to work satisfactorily only for one-dimensional cases.

When a nonlinear differential equation is a description of some physical situation, the nature of the nonlinearity is known and often a special numerical method can be devised to control the nonlinearity during a relaxation-type iteration procedure. When the generalized Newton's method has serious drawbacks then the above becomes necessary. For example, the projection method (Ref. 41) can be applied in order to control the nonlinear terms.

For the nonlinear parabolic differential equations, the projection method is usually applied in order to control the nonlinear term. For example, we consider the following nonlinear equation:

$$a(F) \frac{\partial^2 F}{\partial x^2} = \frac{\partial F}{\partial t}$$

The finite difference analogs used in solving this simple type of equation are centred around the time level $t + \delta t/2$, and the coefficient $a(F)$ must be evaluated at this time level. The simplest method of solving this type of equation is an iteration process where for all grid points i , the terms $a(F_i)$ are first evaluated using the values of F_i at time t . Substitution of these terms into the difference equations results in a set of linear equations which are easily solved for the function F at the time $t + \delta t$. The coefficients $a(F_i)$ are then re-evaluated, using for F_i the average of its value at time t and the newly calculated value for time $t + \delta t$. After substitution of the newly calculated $a(F_i)$ terms, the difference equations are again solved for the function F_i at time $t + \delta t$. This iteration is repeated until the function F_i determined in two successive iterations agree within a predetermined tolerance. The nonlinear terms have been projected forward to the level $t + \delta t/2$. More sophisticated techniques use a Taylor series in conjunction with the finite-difference analog of the original equation to project the nonlinear terms to the half-time level. The above projection method can be used in the usual boundary-layer equations. Further discussion on the nonlinear partial-differential equations in engineering applications can be found in Ref. 42.

Many methods can be applied for the parabolic-type partial-differential equations, for example, the explicit method, implicit method, Crank-Nicolson method, DuFort-Frankel method, Saul'yev method, and the explicit and implicit alternating-direction methods. In the explicit method, usually undesirable restrictions on the step-size increment occur in the computation. The implicit method can overcome this difficulty at the expense of a somewhat more complicated calculation procedure. However, the discretization errors for both methods are still too large. The Crank-Nicolson

method is of the implicit type and also can decrease the discretization errors. It is always stable and the error is of second order.

The solution of equations resulting from the implicit or Crank-Nicolson method can be obtained by any elimination technique. However, since the resulting equations have the form of the tridiagonal-type the complete algorithm method, which has less of an iteration scheme than the Gaussian or Gauss-Seidal elimination methods, can be applied. A general form which can be applied by explicit, implicit or Crank-Nicolson method is developed in the present work. An excellent review for the finite difference method of solution of the boundary-layer equations has been given by Blottner (Ref. 17).

5.2 Finite Difference Equations

The nonlinear equations, Eqs. (20)-(23), with the boundary conditions of a mixed Neumann/Dirichlet type are solved numerically by the finite-difference method. An implicit six-point finite-difference scheme is applied.

These equations are first linearized in a form suitable for an iteration scheme. Blottner (Ref. 17) has stated that the order of the equations is important. The momentum equation is solved first, and the species must be solved before the atom temperature. Therefore, these linearized equations can be written in order as follows:

$$C_F^{(p)} + [C_\eta + f + 2\xi f_\xi] F_\eta^{(p)} - \beta_F F F^{(p)} = 2\xi F F_\xi^{(p)} - \beta_F \frac{\rho_\delta}{\rho} \quad (64)$$

$$\left[\frac{C}{Sc} \right] z_{\eta\eta}^{(p)} + \left[\left(\frac{C}{Sc} \right)_\eta + f + 2\xi f_\xi \right] z_\eta^{(p)} - \left[\beta_z F - \tau_u \frac{\dot{n}_e}{n_e} \right] z^{(p)} = 2\xi F z_\xi^{(p)} \quad (65)$$

$$\begin{aligned} \left[\frac{C}{Pr} \right] \theta_{\eta\eta}^{(p)} + \left[\left(\frac{C}{Pr} \right)_\eta + f + 2\xi f_\xi \right] \theta_\eta^{(p)} - \left[F \left(\beta_{T_a} + \frac{\beta_F \tau_F}{1 + \alpha_\delta \tau} \right) + \frac{3}{5} \tau_u \alpha_{vai} \right] \theta^{(p)} = 2\xi F \theta_\xi^{(p)} - \tau_F C_F^2 + \tau_u Q_R / (\rho C_p T_{a\delta}) \\ + \alpha \frac{T_e}{T_{a\delta}} \left[- \frac{3}{5} \tau_u V_{vai} + \tau_I \frac{(\dot{n}_e)_a}{n_e T_e} \right] + \beta_F \tau_F F z_\theta \frac{\alpha_\delta \tau}{1 + \alpha_\delta \tau} \end{aligned} \quad (66)$$

$$\begin{aligned} \left(\frac{C}{Pr_e} \right) \theta_{\eta\eta}^{(p)} + \left[\left(\frac{C}{Pr_e} \right)_\eta + \left(\frac{C}{Sc} \right) \alpha_\delta z_\eta + \alpha(f + 2\xi f_\xi) \right] \theta_\eta^{(p)} - \alpha \left[\beta_{T_e} F + \frac{3}{5} \tau_u V_{vai} + \tau_u \frac{\dot{n}_e}{n_e} \right] \theta^{(p)} \end{aligned} \quad (67)$$

Contd...

$$= 2\xi F\theta_{\xi}^{(p)} + \alpha \frac{T_a}{T_{e\delta}} \left[-\frac{3}{5} \tau_u v_{eai} + \tau_I \frac{(\dot{n}_e)_e}{n_e T_a} \right] \quad (67)$$

where

$$\tau_u = \frac{2\xi}{\rho_{\delta} \mu_{\delta} u_{\delta}^2}, \quad \tau_f = \frac{u_{\delta}^2}{C_p T_a \delta}$$

$$\tau = \frac{T_{e\delta}}{T_a \delta}, \quad \tau_I = \frac{2}{5} \tau_I \tau_u$$

$$v_{eai} = 2 \left(\frac{m k_B T_e}{m_e} \right)^{1/2} \frac{m_e}{m_a} [n_a \sigma_{ea} + n_e \sigma_{ei}]$$

The superscript p denotes the order of the iteration process and the quantities without the superscript denote those evaluated at the $p-1$ iteration order. $F = \partial f / \partial \eta$ or

$$f = \int_0 F d\eta \quad (68)$$

These linearized equations are of the second order and are solved for the unknowns F , z , θ and Θ in that order. The derivatives and the integral in the η -direction are then expressed by three-point difference formulae. The derivatives in the ξ -direction are approximated by a forward-difference scheme.

Let i and j be the indices of the η , ξ -coordinates for the difference net at the point considered in Fig. 1. Any function W (F , z , θ or Θ) is written in terms of the values of two adjacent points in the ξ -direction as

$$W = \lambda W(i, j+1) + (1 - \lambda) W(i, j)$$

where λ is a weighting factor which can be suitably adjusted for improving the convergence of the iteration scheme:

$$\lambda = \begin{cases} 0: & \text{Explicit method} \\ \frac{1}{2}: & \text{Crank-Nicolson method} \\ 1: & \text{Implicit method} \end{cases}$$

In this formulation either equal intervals or nonequal intervals in η -direction can be used. In the present case, the interval in η -direction is increased in a geometric progression as

$$\frac{\Delta\eta_{i+1}}{\Delta\eta_i} = k$$

where k is a constant which is set with a value slightly greater than unity.

The following derivatives are applied:

$$\begin{aligned} W_{\eta} &= \frac{\lambda}{(1+k)k^i} \frac{1}{\Delta\eta_1} [W(i+1, j+1) + (k^2-1)W(i, j+1) - k^2W(i-1, j+1)] \\ &+ \frac{1-\lambda}{(1+k)k^i} \frac{1}{\Delta\eta_1} [W(i+1, j) + (k^2-1)W(i, j) - k^2W(i-1, j)] \end{aligned} \quad (69)$$

$$\begin{aligned} W_{\eta\eta} &= \frac{2\lambda}{(1+k)k^{2i-1}} \frac{1}{\Delta\eta_1^2} [W(i+1, j+1) - (1+k)W(i, j+1) + kW(i-1, j+1)] \\ &+ \frac{2(1-\lambda)}{(1+k)k^{2i-1}} \frac{1}{\Delta\eta_1^2} [W(i+1, j) - (1+k)W(i, j) + kW(i-1, j)] \end{aligned} \quad (70)$$

$$W_{\xi} = \frac{1}{\Delta\xi} [W(i, j+1) - W(i, j)] \quad (71)$$

where $\Delta\eta_1$ is the first interval in η -direction.

The quantity ξ is evaluated at a point between two adjacent points as

$$\xi = \lambda \xi_{j+1} + (1-\lambda) \xi_j$$

The values f and f_{ξ} at a $(i, j+1)$ point are given by

$$\begin{aligned} f(i, j+1) &= \sum_{\ell=1}^i \frac{k^{\ell-1} \Delta\eta_1}{6} \left[\left(\frac{2+3k}{1+k} \right) F(\ell-1, j+1) + \left(\frac{1+3k}{k} \right) F(\ell, j+1) \right. \\ &\quad \left. - \left(\frac{1}{k(1+k)} \right) F(\ell+1, j+1) \right] \end{aligned} \quad (72)$$

$$\begin{aligned} f_{\xi}(i, j+1) &= \sum_{\ell=1}^i \frac{k^{\ell-1} \Delta\eta_1}{6} \left[\left(\frac{2+3k}{1+k} \right) F_{\xi}(\ell-1, j+1) + \left(\frac{1+3k}{k} \right) F_{\xi}(\ell, j+1) \right. \\ &\quad \left. - \left(\frac{1}{k(1+k)} \right) F_{\xi}(\ell+1, j+1) \right] \end{aligned} \quad (73)$$

where

$$F_{\xi}(\ell, j+1) = \frac{1}{\Delta\xi} [F(\ell, j+1) - F(\ell, j)]$$

The linearized equations, Eqs. (64)-(67), may be written in the following common form with

$$x_1^{(1)} W_{\eta\eta}^{(1)} + x_2^{(1)} W_{\eta}^{(1)} + x_3^{(1)} W^{(1)} = x_4^{(1)} W_{\xi}^{(1)} + x_5^{(1)} \quad (74)$$

where $W^{(1)} = F$, $W^{(2)} = z$, $W^{(3)} = \theta$ and $W^{(4)} = \theta$. The expressions $x_j^{(i)}$ ($i = 1$ to 4) for the momentum, species, atom temperature and electron temperature equations are listed in Appendix C.

Substituting Eqs. (69)-(71) into Eq. (74), the following equation is obtained:

$$A_i^{(t)} W^{(t)}(i-1, j+1) + B_i^{(t)} W^{(t)}(i, j+1) + C_i^{(t)} W^{(t)}(i+1, j+1) = D_i^{(t)} \quad (75)$$

where $t = 1$ to 4; $i = 1$ to N and $j = 1$ to M .

$$\begin{aligned} A_i^{(t)} &= a_i k x_1^{(t)} - c_i k^2 x_2^{(t)} \\ B_i^{(t)} &= -a_i x_1^{(t)}(1+k) + c_i x_2^{(t)}(k^2-1) + \lambda x_3^{(t)} - \frac{x_4^{(t)}}{\Delta\xi} \\ C_i^{(t)} &= a_i x_1^{(t)} + x_2^{(t)} c_i \end{aligned} \quad (75a)$$

$$D_i^{(t)} = -b_i x_1^{(t)} \Delta W - d_i x_2^{(t)} \Delta W - (1-\lambda) x_3^{(t)} W(i, j) - \frac{x_4^{(t)}}{\Delta\xi} W(i, j) + x_5^{(t)}$$

$$a_i = \frac{2\lambda}{(1+k)k^{2i-1}} \frac{1}{\Delta\eta_1^2}$$

$$b_i = \frac{2(1-\lambda)}{(1+k)k^{2i-1}} \frac{1}{\Delta\eta_1^2}$$

$$c_i = \frac{\lambda}{(1+k)k^i} \frac{1}{\Delta\eta_1}$$

$$d_i = \frac{1-\lambda}{(1+k)k^i} \frac{1}{\Delta\eta_1}$$

$$\Delta W = W(i+1, j) + (k^2-1)W(i, j) - k^2 W(i-1, j)$$

$$\Delta^2 W = W(i+1, j) - (1+k)W(i, j) + kW(i-1, j)$$

The boundary conditions for the finite difference equations are:

$$i = 0 (\eta = 0): \quad W^{(1)}(0, j+1) = \frac{u_w}{u_\infty}$$

$$W^{(2)}(0, j+1) = 0 \quad \text{for } z_w = 0$$

$$= W^{(2)}(1, j+1) - \Lambda_1 \Delta \eta_1 \quad \text{for } z'_w = \Lambda_1$$

$$W^{(3)}(0, j+1) = \frac{T_w}{T_{a\infty}}$$

$$W^{(4)}(0, j+1) = W^{(4)}(1, j+1) - \Lambda_2 \Delta \eta_1 \quad \text{for } \theta'_w = \Lambda_2$$

$$= W^{(4)}(1, j+1) \quad \text{for } \theta'_w = 0$$

$$i = N (\eta \rightarrow \infty)$$

$$W^{(1)}(N, j+1) = 1$$

$$W^{(2)}(N, j+1) = 1$$

$$W^{(3)}(N, j+1) = 1$$

$$W^{(4)}(N, j+1) = 1$$

The maximum value of i (or N) which represents the freestream condition can be determined as follows: After the values k and $\Delta \eta_1$ are chosen (see next section), the results for all grid points at a fixed j with an arbitrary value N are compared with that calculated from the $N+1$ value. If they do not have the same value, then N is increased until the results of using N and $N+1$ have identical values. In order to guarantee that the value N used represents the freestream condition for all j , N is given by $N = N_0 + 20$, where N_0 is the minimum value of N at $x = 0$. The maximum value of η is obtained from the following equation,

$$\eta_{\max} = \sum_{i=1}^N i \Delta \eta_1$$

The computational scheme is an iterative one. The momentum equation is first solved with assumed distributions of species and

atom and electron temperatures. The resulting velocity field is employed for the species equation. The resulting species field is then applied to the equations for atom and electron temperatures, respectively. The new species and atom and electron temperature distributions are then used to replace the assumed one and the process is continued until the solutions converge to satisfy a preset criterion.

The convergence criterion of the system of difference equations to the differential equations has not been investigated. However, Douglas et al (Ref. 43) stated that an implicit or Crank-Nicolson difference scheme is convergent for an equation of the type given by Eq. (74).

In order to avoid third-order derivatives in the momentum equation, Blottner (Ref. 7) has introduced a transformed normal velocity and retained the continuity equation. However, in the present method, the stream function is introduced and the momentum equation is written as a second-order equation. The partial differential equation for momentum involves f and f_ξ . The value of f can be readily obtained from an integration once the value of the tangential velocity component across the boundary layer is known. The same method was applied by Fannelop (Ref. 44). Sells (Ref. 45) also used the same implicit finite-difference method for a laminar compressible boundary layer and Chan (Ref. 46) for a turbulent incompressible boundary layer.

5.3 Accuracy and Stability

The accuracy of the numerical solution has to be better than the accuracy of the different physical models. The models used for the description of transport properties, chemical reactions and sheath theory are not supposed to have a higher accuracy than $O(10^{-1})$. The accuracy of the experimental results is at best $O(10^{-2})$. Therefore, it seems sufficient to achieve numerical results which are accurate to $O(10^{-2})$.

The accuracy of the numerical method can be achieved to any small order, say $O(10^{-5})$, at the expense of computation time. Once the accuracy of the problem is determined, the upper bounds for $\Delta\xi$ and $\Delta\eta$ are posed.

The accuracy of any numerical method can be checked by: (1) varying the ξ and η increments, (2) disturbing the boundary conditions slightly, (3) applying the difference-differential method or other numerical methods, (4) applying a stability analysis to the linearized equations, and (5) applying the method to a simple problem that can be solved analytically. In the present analysis items (1) to (4) were applied to check the accuracy of the Crank-Nicolson scheme. The step sizes used in the calculation are decreased by half and the solutions follow this in a way corresponding to the orders of the local truncation errors and remain stable. A small disturbance to the input data gives a small change in the solution. The results obtained by using $\lambda = 0.5$ (Crank-Nicolson method) and $\lambda = 1$ (implicit method) were compared and the accuracy was within $O(10^{-2})$.

In the present analysis, nonequidistant step sizes were used in order to decrease the computation time. However, the nonequidistant discretization may lead to larger inaccuracy and can even spoil the solution completely. Also the determination of error bounds for nonequidistant step sizes is more complicated than an equidistant regular network. Fortunately, the nonequidistant

discretization can be checked in the present program by comparing the results with $k = 1$ and with $k \neq 1$. It was shown that the nonequidistant discretization does not lead to larger inaccuracy or spoil the solution in the present program.

As mentioned in Section 5.2, the stability criteria for a system of nonlinear partial-differential equations are difficult to determine. When the Crank-Nicolson scheme is applied, bounded oscillations in ξ -direction appear in the analysis. Crandall (Ref. 47) showed that at a relatively large step size in ξ -direction, bounded oscillations are possible even for linear equations. According to Smolderen (Ref. 48) this may be even worse in the case of nonlinear equations. Douglas (Ref. 49) also mentioned the possibility of oscillations in the solution using a Crank-Nicolson scheme with boundary conditions of the mixed type. These oscillations do not occur when a backward-implicit method is used. However, a smaller step size, $\Delta\xi$, than the one used in the Crank-Nicolson scheme is needed for the backward-implicit scheme for the same accuracy. This results in more computation time. For the present case, the oscillation can be controlled by a suitable choice of the parameter λ . From our experience of the present analysis, the Crank-Nicolson scheme provides a bound oscillation in ξ -direction. This oscillation does not damp out even for a very small step-size $\Delta\xi$. Therefore, decreasing step size $\Delta\xi$ is not the best way to get more accuracy. This oscillation can be checked by using different values of λ in the calculations starting from an optimum value 0.5 to a maximum value of 1.0, and the smallest value of λ in this range which just eliminates the oscillations is the one to use. In the present analysis, the best value of λ was found to be 0.75 where the oscillation damps out in the first few steps. With $\lambda = 0.75$, the discretization error is expected to be $O(\Delta\xi^{1.5})$, which is smaller than $O(\Delta\xi)$ for a backward-implicit scheme.

For example (see Chapter 6, for the flat-plate boundary layer) $U_0 = 3.53 \times 10^5$ cm/sec, $T_{a0} = T_{e0} = 1.059 \times 10^4$ K, $\alpha_0 = 0.031$ and $p_0 = 1200$ torr was used for all x . The step-size $\Delta\xi$ was increased with x . At first the value of the weight parameter $\lambda = 0.5$ was used, and in all runs oscillation in f_w'' and z_w' started at the first step downstream. This oscillation tended to be small at $i = 45$. In another run $\lambda = 0.75$ was used, and this time the oscillation damped out within two steps downstream and did not reappear. Figure 2 shows how the values f_w'' and z_w' oscillate as the step number j increases. Consequently, the Crank-Nicolson scheme ($\lambda = 0.5$) was abandoned and $\lambda = 0.75$ was used in the present analysis.

Attempts were made to relate this oscillation to errors due to the step-size $\Delta\eta$ and $\Delta\xi$ with the aid of formulae like the Richardson-extrapolation rule, but a satisfactory answer was not obtained. Therefore, the oscillations were not induced only by a finite step-size as they were considerably larger than the errors expected from such step sizes.

5.4 Transformation of Coordinates

The conditions at the edge of boundary layer, U_0 , α_0 , T_{a0} , T_{e0} and p_0 , resulting from the solutions of the inviscid flow equations (see Section 4.3) are a function of x . A table of these edge properties as a function of x was used and the interpolation was applied to obtain the edge conditions for any value of x . However, the finite difference procedure was applied for the transformed (ξ, η) -coordinates. Therefore, the final results must be related back to the physical (x, y) -coordinates.

The relation between the transformed coordinate ξ and the distance x along the surface can be determined from Eq. (18). The relation between ξ and x can be determined by the following equation:

$$\xi_{j+1} = \xi_j + \Delta\xi \quad (76a)$$

with

$$\Delta\xi = \frac{\Delta x}{2} [\gamma(x_j) + \gamma(x_j + \Delta x)]$$

$$\gamma(x_j) = [\rho_0 \mu_0 U_0] \quad \text{at } x = x_j$$

$$x_{j+1} = x_j + \Delta x$$

The coordinate y relating to coordinate η is given by

$$y = \frac{\sqrt{2\xi}}{U_0} \int_0^\infty \frac{1}{\rho} d\eta \quad (76b)$$

where the three-point formula for nonequidistant step sizes applied in Eq. (72) can be used for Eq. (76).

6. FLAT-PLATE BOUNDARY-LAYER FLOWS IN IONIZING ARGON

6.1 General Considerations

Experiments on shock-wave structure and the boundary-layer flows induced by a strong shock wave were recently conducted at UTIAS in the Hypervelocity Shock Tube. These experiments provided unique and reliable interferometric data for both types of flows. Experiments on shock-wave structure were conducted by Bristow (Ref. 50), Brimelow (Ref. 51), Tang (Ref. 52) and Whitten (Ref. 39), and on the flat-plate and the shock-tube sidewall boundary layers by Whitten (Ref. 39) and Brimelow (Ref. 51), respectively. Comparisons of numerical and experimental results on shock-wave structures are given in Refs. 24 and 25 for argon and krypton, respectively.

Measurements of ionizing flat-plate boundary-layer flows have been reported by some authors (Tseng and Talbot, Ref. 13; Brown and Mitchener, Ref. 38; Bredfeldt et al, Ref. 53) for low temperatures and low electron-number densities. Under these conditions, the radiation-energy loss in the plasma is small and can be neglected for both the inviscid and viscous flow regions. Thus, the conditions at the edge of the boundary layer can generally be calculated from a nonradiant model in which the freestream-flow quantities are constant and independent of time.

Figure 3 shows schematically the experimental generation of a flat-plate boundary-layer flow over an airfoil model with a sharp expansion corner in the UTIAS 10 cm x 18 cm Hypervelocity Shock Tube. Such a boundary layer

can be regarded as developing in a steady flow if the shock wave is travelling at a constant velocity and the radiant energy loss is small. However, for the case of a flow induced by a stronger shock wave ($M_s \geq 13$), the radiation-energy loss becomes significant and the boundary layer develops in a somewhat unsteady (nonuniform) flow.

A typical analysis of the inviscid radiant flow behind a shock wave travelling at constant velocity is shown in Fig. 4. In this case, the shock wave is moving at a Mach number $M_s = 12.8$ into quiescent argon at $p_0 = 5.01$ torr and $T_0 = 297$ K and has been shown at a location $x_s = 40$ cm past the leading edge of the flat plate. The gradients result from the radiation-energy loss. Clearly, as the nonstationary shock wave travels along the tube, the inviscid-flow conditions above the plate change with time, introducing an unsteady (nonuniform) effect. Along the flat plate, it is seen that u_δ and p_δ decrease as x increases from the leading edge (or as one moves closer to the shock front) while $T_{a\delta}$, $T_{e\delta}$ and α_δ all increase. However, the fact that the inviscid flow with respect to the plate is unsteady rather than steady with flow gradients, is emphasized by a consideration of the overall momentum equation for the plasma. In a steady, one-dimensional inviscid flow,

$$\rho_\delta u_\delta \frac{du_\delta}{dx} = - \frac{dp_\delta}{dx}$$

That is, the velocity gradient and pressure gradient should have opposite signs, which is not the case in this flow.

It can be seen, however, that the variations of u_δ , $T_{a\delta}$, $T_{e\delta}$ and p_δ are quite small, particularly as the distance, x_s , from the leading edge to the shock wave increases. Under these circumstances, it is reasonable to regard the flat-plate boundary-layer flow as quasi-steady to a first-order approximation, such that the steady-flow analysis described previously can be applied. It should be mentioned that the relative changes in α_δ are slightly larger, however, and the full extent of this effect on the quasi-steady-flow assumption is not known at the present time.

For comparisons of boundary-layer profiles measured at a position x_m with analytical predictions, the inviscid flow conditions at x_m were assumed to prevail over the entire freestream region (all x) in order to satisfy the steady-flow assumption in the analysis. The initial conditions for the shock wave and the freestream quantities resulting from the radiant inviscid flow are listed in Table 1.

In the finite difference analysis, the best value of the weight parameter was found to be $\lambda = 0.75$, where the oscillations damped out during the first few steps. Case 2 of Table 1 was run with $k = 1.05$, $\Delta\eta = 0.05$ and $N = 46$ by using a step-size Δx started with 0.01 cm at $x = 0$ and increased to 0.2 cm at $x = 14$ cm. At first the value of the weight parameter $\lambda = 0.5$ was used, and in all runs oscillations in f_w' and z_w' started at the first-step downstream. The oscillations were bounded and tended to become small as x increased. The other run with $\lambda = 0.75$ was used, and this time the oscillations damped out within two downstream steps and did not reappear. Therefore the Crank-Nicolson scheme ($\lambda = 0.5$) was abandoned and $\lambda = 0.75$ was used in the analysis.

6.2 Comparison of Theoretical and Experimental Results

For the case of $M_g = 16.6$ and $p_0 = 4.81$ torr, the initial flow profiles (at $x = 0$) are shown in Fig. 5. The nondimensional electron-temperature profile θ is unity for all η , resulting from the electric-sheath condition $\theta' = 0$ at $x = 0$. The atom-temperature profile θ increases from 0.029 at $\eta = 0$ to 1 at $\eta = 1.95$, and reaches a maximum value 1.04 at $\eta = 2.4$ and then approaches unity at $\eta = 4.25$. The normalized velocity profile f' increases from zero at $\eta = 0$ to 1 at $\eta = 4.5$, while the normalized degree of ionization profile z increases from 0 at $\eta = 0$ to 1 at $\eta = 3.5$.

The variations of the transport properties at $x = 0$ of Pr , Sc , C and Pr_e with η are shown in Fig. 6. The Prandtl number for the heavy particles Pr is constant ($Pr = 0.667$) from its definition in this analysis. The ratio of density-viscosity product C decreases from 2.8 at $\eta = 0$ to 1 at $\eta = 2.23$. The Schmidt number Sc increases from 1.5 at $\eta = 0$ to 2.42 at $\eta = 1.4$, and then decreases to the freestream value 2.39 at $\eta = 3.12$. Similarly, Pr_e increases from 0.035 at $\eta = 0$ to 0.52 at $\eta = 2.4$ and then decreases to the freestream value 0.507 at $\eta = 4.79$. These transport-property parameters are functions of n_a , n_e , T_a , T_e and p_0 . The variations of these parameters with η have some effects on the boundary-layer structure. The effect of Pr_e on the electron-temperature profile is more significant than that of C on the velocity profile and of Pr on the atom-temperature profile. The total-Prandtl number Pr of the plasma can be obtained from the following equation:

$$\frac{1}{Pr} = \frac{1}{Pr} + \frac{1}{Pr_e}$$

The variations of the flow profiles with distance x are shown in Fig. 7. The velocity profile f' is almost independent of x . The variation of atom temperature ratio θ with x is also small. Therefore, the momentum and atom-temperature equations can be obtained approximately from a similarity assumption. However, significant variations of the degree of ionization ratio z and electron-temperature ratio θ with x do occur, as shown, and errors will result from a similarity assumption. The degree of ionization α and the electron temperature T_e decrease as x increases at a constant η . At $\eta = 0$, θ_w decreases from 1 at $x = 0$ to 0.87 at $x = 14$ cm.

The variations of Pr_e with η for $x = 0$ and $x = 14$ cm are shown in Fig. 8. It is seen that for $x > 0$, Pr_e exceeds the freestream value (0.507), up to $\eta \sim 2.5$.

In addition to the profiles of the various flow quantities across the boundary layer, parameters that characterize the skin friction, heat transfer due to conduction and diffusion processes and thickness of the boundary layer are important. The variations of the skin friction parameter f_w and the heat transfer parameters θ_w' and z_w' for conduction and diffusion processes, respectively, with distance x are shown in Fig. 9. The values of f_w are almost independent of x , while θ_w' increases at small x and approaches a nearly constant value for large x . The quantity z_w' decreases significantly for $x < 2$ cm and approaches a nearly constant value for large x . The boundary-layer-displacement thickness δ^* is plotted in Fig. 10 as a function of x . For x greater than 4 cm, δ^* increases almost linearly. The physical-boundary-layer thicknesses with a flow-quantity ratio of 0.995 for velocity δ_f , degree of ionization δ_z , atom temperature δ_{T_a} and electron temperature δ_{T_e} are plotted

in Fig. 11. It can be seen that the boundary-layer ($x > 3$ cm) thickness for velocity is greater than the other boundary-layer thicknesses for this case. The thickness of the electron thermal layer, δ_{Te} , is thinner than the velocity thickness which differs from the result found by Honma and Komuro (Ref. 16) for a sidewall boundary-layer flow. They showed that the thickness of the electron thermal layer is almost ten times that of the velocity or atom-temperature thicknesses.

The large change in the chemical-reaction rates with temperature has an important effect on the boundary-layer structure for the case of a large degree of ionization. Figure 12 shows the effects of chemical-reaction rates on boundary-layer structure. The results for a frozen flow ($\dot{n}_e = 0$) are compared with those for a nonequilibrium flow at $x = 14$ cm and $M_s = 16.6$. The profiles of velocity f' , and heavy particle temperature θ , hardly differ for both cases. However, the profiles of electron temperature θ_e , degree of ionization z , and electron Prandtl number Pr_e , are significantly affected by the chemical reactions. For a given η , the electron temperature θ is lower for a frozen flow than for a nonequilibrium flow, while the reverse is true for the degree of ionization z .

Comparisons of analysis with experimental results are shown in Figs. 13 and 14 for plasma density and electron-number density, respectively. Better agreement is obtained for the measured plasma density profile with the frozen-flow analysis. However, poor agreement with analysis is obtained for the electron number-density profile with either solution. The experimental data show a significant bump in the n_e profile which is not predicted by either the nonequilibrium or the frozen-flow analysis. A similar bump appears in the experimental data for the degree of ionization profile shown in Fig. 15, while there is no bump in the analytical result. This disagreement has not been resolved.

For the second case with $M_s = 12.8$, $p_0 = 5.01$ torr and $T_0 = 297$ K, the nonequilibrium and frozen-flow profiles at $x = 14$ cm are shown in Figs. 16 and 17, respectively, for comparison. It is also shown that significant differences exist for degree of ionization and electron temperature profiles, as predicted for $M_s = 16.6$ case. The analytical and experimental results for plasma density and electron number density profiles are compared in Figs. 18 and 19, respectively, while the corresponding degree of ionization profile is shown in Fig. 20. Unlike case 1, the experimental plasma-density data shows better agreement with the nonequilibrium or the calculated equilibrium similarity-solution profiles, which are very close. The experimental results for n_e lie between the analytical nonequilibrium and frozen-flow profiles. The two-temperature frozen-flow solution predicts a larger bump than that obtained from the experiment, while no bump occurs in the nonequilibrium or equilibrium profiles. The experimental data for the degree of ionization lie closer to the calculated frozen profile rather than the nonequilibrium profile.

The local-similarity solution based on thermal and chemical equilibrium are also plotted in Figs. 18-20 for case 2. It is seen that equilibrium would not occur in such boundary-layer flows. Of the three models used in the analyses for n_e and α , the equilibrium profiles provide the worst agreement with the experimental results. The n_e profile is the most sensitive indicator of the state of the boundary layer. The fact that the density data agree with the three models used in the analyses shows that it is not a sensitive parameter. Undoubtedly, measurements of electron and heavy-particle temperatures

are desirable as they would be sensitive indicators of the state of the boundary layer.

The disagreement between theory and experiment for n_e (or α) may result from: (i) the boundary-layer flow is assumed to be quasi-steady while in the experiments it is actually nonstationary with time resulting from radiation losses (which were only partially accounted for), and the effects of the sidewall boundary layers (which were not taken into account at all and have flow effects similar to radiation). These effects will be more pronounced at higher shock Mach numbers where the radiation-energy loss is significant. For example, the agreement between theory and experiment for $M_s = 16.6$ is worse than that for $M_s = 12.8$ for the n_e and α profiles. In order to assume that the boundary-layer flow is quasi-steady, the variations of the flow quantities at the edge of the boundary layer with distance were neglected in the theory. This error might have a significant effect on the boundary-layer structure. (ii) The assumptions made in the basic equations (such as $\rho_1 V_1 \approx -\rho D_a \partial \alpha / \partial y$ and $\bar{v} \cdot \nabla p_e \approx 0$), the uncertainty of the parameters used to describe the elastic and inelastic-energy-transfer rates and the model used for the radiation-energy loss, may all affect the entire boundary-layer structure. However, the comparison of analysis and experiment for the $M_s = 12.8$ case is quite good and lends support that the assumptions made in the basic equations are reasonable. Furthermore, from the shock-wave-structure analyses (Glass and Liu, Ref. 24; Glass et al, Ref. 25) the parameters used for the elastic and inelastic-energy transfer and the radiation model are considered as accurate within the limitations of present-day collision theory.

As noted earlier some possible errors in the present analysis may result by neglecting the re-absorption of the radiation-energy loss in the freestream and the effects of the sidewall boundary layers on the freestream flow. An exact solution to the set of simultaneous ordinary differential equations for the freestream flow including re-absorption would be difficult since the re-absorption coefficient is a function of the complete structure of the radiation cooling zone. The question would also arise whether the shock tube has a finite or an infinite optical depth. The Rosseland mean-free-path for argon at the freestream conditions of $M_s = 16.6$, $p_0 = 4.81$ torr and $T_0 = 296$ K (case 1), is about 97 cm. Therefore, the freestream plasma is optically thin and the re-absorption energy should be small. For the present calculations it was necessary to consider the worst case when there is no re-absorption. The shock-tube sidewall boundary layer will have some effects on the freestream conditions. In general, it would be desirable to study the present flat-plate boundary layer after the effects of the shock-tube sidewall boundary layers on the freestream were determined. In the present analysis the freestream conditions were obtained under the assumption that the flow was one-dimensional; the role of the sidewall boundary-layer growth on the inviscid flow was not considered. Mirels (Ref. 54) has shown that the flow between the shock wave and contact surface in an actual shock tube is non-uniform due to the wall boundary layer. Recently, Enomoto (Ref. 55) has studied the effects of the boundary-layer growth in shock tubes of various cross-sections on the shock-wave ionization-relaxation process in argon. He used Mirels' boundary-layer theory for a perfect gas to get some estimates. He showed that by considering the sidewall boundary-layer effects the ionization relaxation time was shortened. The inclusion of re-absorption of radiation energy and sidewall boundary-layer effects will increase the degree of ionization in the freestream. Neglecting these two effects in the analysis might alter the freestream conditions. In order to

study the effects of the freestream conditions on the boundary-layer structure for the $M_g = 16.6$ case, where the theoretical and experimental boundary-layer thicknesses for n_e are 0.8 mm and 2 mm, respectively ($x = 14$ cm), three different freestream values (at $t = 20 \mu s$, $40 \mu s$ and $60 \mu s$ after the passage of the shock wave) were used for comparison. Even then, the theoretical boundary-layer thicknesses for n_e are between 0.8 mm and 1.2 mm and still differed from the experimental results. It is shown that the boundary-layer thickness for n_e increases as the degree of ionization in the freestream increases.

It is worth noting that the error due to neglecting the photo-ionization in the analysis may not be small. Near the wall, where the ionization due to electron-atom collisions is small compared with that in the freestream, photons resulting from stimulated emission and radiation processes may have an opportunity to ionize atoms. The populations of the photon flux should be known before any calculation on the photo-ionization rate can be done.

The effects of chemical reactions on boundary-layer structure and the sidewall boundary layer on the shock structure are discussed in Appendices D and E, respectively.

Finally, from a comparison of the theoretical results of Mansfeld (Ref. 15) and the experimental results of Kuiper (Ref. 56) for a thermal Rayleigh boundary layer, it was shown that the frozen models lead to values obtained from a nonequilibrium model. No bump in n_e occurred in either theory or experiment for a thermal Rayleigh boundary layer. Details of the results described in this chapter are given in Ref. 57.

7. SHOCK-TUBE SIDEWALL BOUNDARY-LAYER FLOWS IN IONIZING ARGON

7.1 General Considerations

A considerable amount of theoretical and experimental work has been done on the prediction of heat transfer and the variations of transport and thermodynamic properties through the shock-tube sidewall (or Rayleigh) boundary layers. Kuiper (Ref. 56) made an interferometric study of the shock-tube endwall boundary-layer flow. Mansfeld (Ref. 15) compared his numerical results with Kuiper's experimental data. However, except for Brimelow's results, there are no experimental data on shock-tube sidewall boundary-layer flows for ionizing argon.

From the comparison of analyses and experiments for the flat-plate and thermal Rayleigh boundary layer flows, it has been shown that electrons have a temperature which is very different from the heavy particles owing to the slow collisional energy-transfer processes between electrons and heavy particles. In the inner part of the boundary layer (i.e., near the wall) an equilibrium assumption is not valid.

Shock-tube sidewall boundary layers for ionizing argon flows were analyzed by Knöös (Ref. 1) for flows with thermal and chemical equilibrium, Honma and Komuro (Ref. 16) for frozen flows and by Takano and Akamatsu (Ref. 14) for flows with thermal and chemical nonequilibrium. Radiation energy losses in both free-stream and boundary-layer flows were neglected in these analyses. Knöös has shown

that the equilibrium solution for the degree of ionization is in good agreement with experiment only near the edge of the boundary layer. Honma and Komuro found that the thickness of the electron thermal layer for frozen flow is about ten times the thickness of the viscous boundary layer, which is in contrast to the results for flat-plate (described in Chapter 6) and thermal Rayleigh boundary-layer flows.

The present chapter deals with comparisons of measurements and related analyses of the total-density and electron-number-density profiles in shock-tube sidewall boundary layer flows. The shock-wave-structure model of Glass and Liu (Ref. 24), which includes radiation-energy losses, was used and Brimelow's interferometric data were accurately re-evaluated for this purpose. A comparison was also made between theoretical and experimental plasma temperatures. Satisfactory agreement has been obtained for shock-tube sidewall boundary-layer flows in ionizing argon.

7.2 Comparison of Theoretical and Experimental Results

The main differences between the flat-plate and shock-tube sidewall boundary layers are: (i) the velocity profile for the flat-plate case increases from zero at the wall to the freestream value at the edge for the sidewall boundary layer. (ii) Ionizing-nonequilibrium phenomena occur in the freestream flow behind the shock front. Consequently, variations of freestream conditions for the sidewall boundary layer are significantly larger than for a flat plate. (iii) The sidewall boundary layer induces significant changes in the freestream, especially in the ionizing shock structure and beyond where the radiation losses are large.

Recently, Brimelow's data were re-evaluated and compared with the radiant shock-structure model of Glass and Liu. The data show that (i) no bump occurs in the electron-number-density profile in the sidewall boundary-layer, unlike the flat-plate case, and (ii) significant two-dimensional and wall effects on the freestream flow exist in the sidewall case at higher shock Mach numbers.

Accurate interferometric determinations of the excitational cross-section constants for argon and krypton atom-atom collisions in the relaxation zone were made by Glass et al over ranges of the initial shock Mach number and pressure of $13 < M_s < 18$ and $3.1 < p_0 < 5.2$ torr, respectively. This shock wave structure model was used to determine the range of freestream conditions.

Two cases were studied for $M_s = 13.1$, $p_0 = 5.6$ torr and $M_s = 15.9$, $p_0 = 5.10$ torr. The initial conditions and the freestream conditions at the measuring station x_m are given in Table 2. Figure 21 shows schematically the shock-tube sidewall boundary layer behind a shock front.

Figure 22 shows a plot of the freestream conditions for $M_s = 13.1$ and $p_0 = 5.16$. The boundary layer profiles were measured at the cascade front where the electron number density is a maximum and the variations of the freestream conditions are significant. At the cascade front, the radiation energy loss rate is maximum.

The dimensionless nonequilibrium-flow profiles of velocity F , degree of ionization α , atom temperature θ and electron temperature θ_e are shown in Fig. 23. It is seen that the velocity profile F is significantly different from that of the flat-plate boundary layer (Fig. 16). The thickness of the electron thermal-layer is much thinner

than that predicted by Honma and Komuro. They indicated a thickness almost an order greater than the present result.

A comparison of analysis with experimental data is shown in Figs. 24 and 25 for plasma density and electron number density, respectively. Much better agreement is obtained between the measured results and the nonequilibrium solutions for the sidewall than for the flat-plate boundary layer. Better agreement was obtained between the measured plasma density and electron-number-density profiles and the frozen-flow analysis for the flat-plate boundary layer. A bump appeared in the experimental data for the electron-number-density profile in the flat-plate case. No bump appeared in the sidewall case. The agreement with the frozen solution is rather poor for the sidewall case. The corresponding profile for the degree of ionization is shown in Fig. 26. Owing to the shape of the velocity profile, δ^* is now negative, as expected. The boundary-layer displacement thickness, δ^* , is plotted in Fig. 27. It is seen that the displacement thickness increases almost linearly with x , when x is greater than 2 cm. A comparison with Fig. 10 shows that the sidewall boundary layer is about an order thicker for an equivalent x .

For the second case with $M_s = 15.9$ and $p_0 = 5.1$ torr, the freestream conditions for p_g , n_{e0} and α_g are shown in Fig. 28 together with experimental results. Good agreement is found. The dimensionless nonequilibrium and frozen-flow profiles at $x = 18$ cm are plotted in Fig. 29. Except for the velocity profile F , these are significantly different between the nonequilibrium and the frozen-flow solutions for degree of ionization, and the atom and electron-temperature profiles. For the flat-plate case, profiles of velocity and atom temperature hardly differ for both cases. Chemical reactions have a significant effect on the degree of ionization profile.

Comparisons of analysis with experimental results are shown in Figs. 30 and 31 for plasma density and electron-number-density profiles, respectively. Better agreement is obtained for the measured plasma-density profile with the nonequilibrium analysis. However, only fair agreement with analysis is obtained for the electron number density profile. The latter is overpredicted by analysis, which is in contrast with the results for case 1. It is also shown that the electron-number density continued to increase with distance from the wall and did not reach asymptotic values. This phenomenon was also observed in the shock wave structure experiments (see Fig. 13, Glass and Liu, Ref. 24). In the relaxation region near the shock-tube wall, the electron cascade front moves in towards the wall slowly at first and then very rapidly. The reasons for this premature ionization close to the wall in the experimental shock wave structure are far from clear. One possibility considered was that a gas-surface interaction occurred between the argon plasma and the chromium-plated steel shock-tube wall. However, two experiments were carried out to try and eliminate this possibility by changing the surface material. However, no changes were observed. This phenomenon is much more in evidence for the stronger shocks. For this reason, experimental results for electron-number density for $M_s = 15.9$ are lower than that predicted. For the previous case with $M_s = 13.1$, the flow parameters reached their asymptotic values at the edge of the boundary layer. The corresponding profile for the degree of ionization is shown in Fig. 32 and the displacement thickness, δ^* , is plotted in Fig. 33 as a function of distance x .

The determination of electron temperature of a shock-heated argon plasma has received wide attention. Among the commonly used plasma diagnostics for electron temperature determination in a flowing gas plasma are Langmuir probing and microwave transmission. The difficulty in measuring two temperatures of a plasma generated by stronger shock-induced boundary layers has been recognized. In the present case, the experimental temperature of argon plasma is determined from the measured plasma-density and electron-number-density profiles by assuming thermal equilibrium in the boundary-layer flow. Even this assumed experimental temperature cannot represent the actual atom or electron temperature. However, some interesting features can be found from a comparison of the theoretical and experimental plasma-temperature profiles. The experimental plasma-temperature profile together with the calculated two-temperature profiles are plotted in Fig. 34 for $M_s = 13.1$ and $p_0 = 5.16$ torr. It is shown that the experimental plasma temperature is close to the electron temperature profile near the wall. In the outer part of the boundary layer, agreement between the theoretical and the indirect experimental results is excellent. A comparison of the temperature profiles for $M_s = 15.7$ and $p_0 = 5.1$ torr is shown in Fig. 35.

From the foregoing comparison of theory and experiment for both flat-plate and sidewall boundary-layer flows, the following differences are observed: (1) The experimental data and the nonequilibrium analysis show that there is no bump in the n_e profile for the sidewall boundary layer. However, such a bump is observed in the experimental flat-plate boundary layer profile. The frozen solution predicts a bump for both layers. (2) Better agreement is obtained between experiment and the nonequilibrium analysis in the sidewall case, while the frozen solutions agree better with experiment than the nonequilibrium solution for the flat-plate case. (3) More significant differences exist between the analytical nonequilibrium and frozen plasma-density profiles for the sidewall boundary layer, while this difference is small for the flat-plate case. (4) Even though the predicted displacement thickness for the sidewall boundary layer is an order of magnitude greater, the predicted and actual density, electron-number density and degree of ionization layers have correspondingly similar values. The density thickness is usually about half the electron-number density thickness. It shows that the total density is not a sensitive indicator of flow variations.

By and large all analytical profiles are consistent for both types of boundary layers. The fact that the experimental data is in better agreement for the sidewall boundary-layer flow may result from: (1) The unsteady effects on the sidewall boundary layer close to the shock front are smaller than those for the flat-plate cases where the shock wave is threefold the distance away. (2) There is significant ionizing nonequilibrium in the free-stream flow in the sidewall case but the flat plate is almost in a state of radiant equilibrium. (3) The degree of ionization at the points measured for the sidewall case is two to threefold larger than that for the flat-plate cases and may favour the agreement with the nonequilibrium analytical profiles.

It is worth noting that the step size Δx , used for the sidewall boundary layer, is much smaller than for the flat-plate case and results in increased computation time.

The assumption $\rho_i V_i \approx -\rho_a (\partial \alpha / \partial y)$ made in the analysis was removed and replaced by

$$\rho_i V_i \approx -\rho D_a \left(1 + \frac{T_e}{T_a} \right) \frac{d\alpha}{dy}$$

in the computer program. It is shown that the effects on the electron-number-density and plasma-density profiles are very small. This was done to remove instabilities at higher shock-Mach number for the sidewall boundary layer by using the above equation.

Finally, from a comparison of the theoretical results of Hutten-Mansfeld (Ref. 15) and the experimental results of Kuiper (Ref. 56) for a thermal Rayleigh boundary layer, it was shown that no bump in n_e occurred in both results. It should be noted that in Kuiper's experiment with $M_s = 11.1$ and $p_0 = 5$ torr, radiation cooling is not negligible. Nevertheless, similar trends of the flow profiles are observed in their end wall boundary layers and our flat-plate and sidewall boundary layers.

8. DISCUSSIONS AND CONCLUSIONS

The complete set of partial-differential equations for a laminar boundary layer in ionizing argon have been solved with a six-point implicit finite-difference scheme. The new features in the analysis are the inclusion of the radiation-energy loss and the appropriate chemical reactions. The latter also include the atom-atom reactions. Account was taken of the variation across the boundary layer of the transport properties based on the known elastic-scattering cross-sections for an argon plasma. The compatibility conditions and the electric-sheath model were described and incorporated into the analysis. The flat plate and shock-tube sidewall boundary-layer flows were analyzed and compared with interferometric data obtained using the UTIAS 10 cm x 18 cm Hypervelocity Shock Tube equipped with a 23-cm diam Mach-Zehnder dual-wavelength interferometer at shock Mach numbers $M_s \approx 13$ and 16 at an initial argon pressure $p_0 \approx 5$ torr and $T_0 \approx 300$ K.

The analysis is probably the most complete and detailed done to date. It clearly shows that the measured electron-number-density and degree-of-ionization profiles in the boundary layer for equilibrium, frozen and nonequilibrium flows are more sensitive than the measured complementary total-number density profile for determining the actual state of the boundary layer, as might have been expected. Agreement between theory and experiment for the density profiles appears good to excellent as there is little difference between the three analytical profiles for the flat-plate boundary-layer flow. However, agreement of experiment with analysis for electron-number density is only fair for the flat-plate case. The experimental data lie between the analytical frozen and nonequilibrium profiles. The experimental data show a bump in the n_e profile at both $M_s = 16.6$ and $M_s = 12.8$ for the flat-plate cases, while analysis only predicts a bump for the frozen case at $M_s = 12.8$. The nonstationary character of the inviscid flow may have an important effect on the boundary-layer structure at high shock Mach numbers where the radiation energy loss is significant. However, a substantive explanation for this phenomenon has not been found.

For the shock-tube sidewall boundary-layer flow it was shown that there is no bump in n_e profile for both the nonequilibrium analysis and the

actual experiments. Better agreement with experiment was found in this case with the nonequilibrium analysis, rather than the frozen analysis. A comparison of the indirect temperature measurements and theory for the plasma-temperature profiles shows excellent agreement.

General conclusions obtained from the comparisons between theoretical and experimental results for the flat-plate and shock-tube sidewall boundary layer flows are given as follows (Liu and Glass, Ref. 58):

- (a) Near the wall the flows are in nonequilibrium or near frozen. Equilibrium solutions are only valid for the flow at the outer part of the boundary layer. The same conclusion was drawn by Kn50s for a sidewall boundary layer and by Hutten Mansfeld for a thermal Rayleigh boundary layer.
- (b) The variation of the flow profiles with distance x for the two types of boundary layers are different. For example, for the flat-plate boundary layer the velocity profile is almost independent on x but not so for the sidewall boundary layer. Consequently, similarity assumptions are reasonable for the velocity and atom temperature profiles for the flat-plate case where the freestream variations are small; and even for the sidewall velocity profiles. However, large errors will arise in electron-number-density and temperature profiles from similarity assumptions in both cases.
- (c) Unlike the total-number density, the electron-number-density profiles are very sensitive indicators for comparing frozen, equilibrium and nonequilibrium analyses with experiments.
- (d) The thickness of the electron thermal layer is of the same order of magnitude as the viscous boundary layer for both flat-plate and sidewall boundary layers. A similar conclusion was made by Hutten Mansfeld from a comparison between his analysis and Kuiper's experimental data for a thermal Rayleigh boundary layer.

REFERENCES

1. Knoös, S. Boundary-Layer Structure in a Shock-Generated Plasma Flow, Part 1. Analysis for Equilibrium Ionization. J. Plasma Phys., Vol. 2, Part 2, 1968, pp. 207-242.
2. Su, C. Continuum Theory of Spherical Electrostatic Probes. Lam, S. H. Phys. Fluids, Vol. 6, No. 10, 1963, pp. 1479-1491.
3. Chung, P. M. Electrical Characteristics of Couette and Stagnation Boundary-Layer Flow of Weakly Ionized Gases. Phys. Fluids, Vol. 7, No. 1, 1963, pp. 110-120.
4. Chung, P. M. Electric Probes in Stationary and Flowing Plasmas, Talbot, L. Part 1. Collisionless and Transitional Probes, and Touryan, K. J. Part 2. Continuum Probes. AIAA J., Vol. 12, No. 2, 1974, pp. 133-154.
5. Fay, J. A. Theory of Heat Transfer to a Shock-Tube End-Wall Kemp, N. H. from an Ionized Monatomic Gas. J. Fluid Mech., Vol. 21, Part 4, 1965, pp. 659-672.
6. Back, L. H. Laminar Boundary-Layer Heat Transfer from a Partially Ionized Monatomic Gas. Phys. Fluids, Vol. 10, No. 4, 1967, pp. 807-819.
7. Blottner, F. G. Nonequilibrium Laminar Boundary-Layer Flow of Ionized Air. AIAA J., Vol. 2, No. 11, Nov. 1964, pp. 1921-1927.
8. Park, C. Heat Transfer from Nonequilibrium Ionized Argon Gas. AIAA J., Vol. 2, No. 1, 1964, pp. 169-171.
9. Finson, M. L. Theory of Stagnation-Point Heat Transfer in Kemp, N. H. Ionizing Monatomic Gases. Phys. Fluids, Vol. 8, No. 1, 1965, pp. 201-204.
10. Liu, W. S. An Analysis of Shock Structure and Nonequilibrium Laminar Boundary Layers Induced by a Normal Shock Wave in an Ionized Argon Flow. UTIAS Report No. 198, 1975.
11. Sherman, A. Nonequilibrium Boundary Layer Along an Insulator Reshotko, E. Wall. AIAA J., Vol. 7, No. 4, April 1969, pp. 610-615.
12. Nishida, M. Structure of Nonequilibrium Boundary Layer Along Matsuoka, K. a Flat Plate in a Partially Ionized Gas. AIAA J., Vol. 9, No. 11, Nov. 1971, pp. 2117-2118.
13. Tseng, R. C. Flat Plate Boundary Layer in a Partially Ionized Talbot, L. Gas. AIAA J., Vol. 9, No. 7, July 1971, pp. 1365-1372.

14. Takano, Y.
Akamatsu, T. A Numerical Analysis on the Ionized Boundary Layer Along a Shock-Tube Side-Wall. *Memoirs of the Faculty of Engineering, Kyoto University, Japan*, Vol. 36, No. 4, 1975, p. 33.
15. Hutten-Mansfeld,
C.B.H. On the Thermal Rayleigh Problem in Partially Ionized Argon. Ph.D. Thesis, Eindhoven Univ. of Technology.
16. Honma, H.
Komuro, H. Ionized Nonequilibrium Laminar Boundary Layer Behind a Moving Shock Wave (II) Finite Difference Method of Solution. *J. Fac. Engineering, Chiba University, Japan*, Vol. 27, No. 52, March 1976.
17. Blottner, F. G. Finite Difference Methods of Solution of the Boundary-Layer Equations. *AIAA J.*, Vol. 8, No. 2, Feb. 1970, pp. 193-205.
18. Dix, D. M. Energy Transfer Processes in a Partially Ionized Two-Temperature Gas. *AIAA J.*, Vol. 2, No. 12, Dec. 1964, pp. 2081-2090.
19. Igra, O. Supersonic Expansion of Nonequilibrium Plasmas. *UTIAS Review No. 38*, 1974.
20. Appleton, J. P.
Broy, K. N. C. The Conservation Equations for a Nonequilibrium Plasma. *J. Fluid Mech.*, Vol. 20, Part 4, 1964, pp. 659-672.
21. Kaufman, A. Article in La Theorie des Gaz Neutres et Ionises. Ed. de Witt and Detoeuf, Wiley, New York, 1960.
22. Grewal, M. S.
Talbot, L. Shock-Wave Structure in a Partially Ionized Gas. *J. Fluid Mech.*, Vol. 16, Part 4, 1963, pp. 573-594.
23. Spitzer, L. Physics of Fully Ionized Gases. Interscience, N.Y., 1956.
24. Glass, I. I.
Liu, W. S. Effects of Hydrogen Impurities on Shock Structure and Stability in Ionizing Monatomic Gases: I. Argon. *J. Fluid Mech.*, Vol. 84, Part 1, 1978, pp. 55-77.
25. Glass, I. I.
Liu, W. S.
Tang, F. C. Effects of Hydrogen Impurities on Shock Structure and Stability in Ionizing Monatomic Gases: II. Krypton. *Can. J. Physics*, Vol. 55, No. 14, 1977, pp. 1269-1279.
26. Hoffert, M. I.
Lien, M. Quasi-One-Dimensional Nonequilibrium Gas Dynamics of Partially Ionized Two-Temperature Argon. *Phys. Fluids*, Vol. 10, No. 8, Aug. 1967, pp. 1769-1777.
27. Jaffrin, M. Y. Shock Structure in a Partially Ionized Gas. *Phys. Fluids*, Vol. 8, No. 4, 1965, pp. 606-624.
28. Chung, P. M.
Mullen, J. F. Nonequilibrium Electron Temperature Effects in Weakly Ionized Stagnation Boundary Layer. *AIAA Paper No. 63-161*, Los Angeles, Calif., June 1963.

29. Amdur, I. Properties of Gases at Very High Temperatures.
Mason, E. A. Phys. Fluids, Vol. 1, No. 5, 1958, pp. 370-383.
30. Fay, J. A. Hypersonic Heat Transfer in the Air Laminar
 Boundary Layer. AMP 71, March 1962, Avon/Everett
 Research Lab.
31. Devoto, R. S. Transport Coefficients of Partially Ionized Argon.
 Phys. Fluids, Vol. 10, No. 2, 1967, pp. 334-364.
32. Frost, L. S. Momentum-Transfer Cross Sections for Slow Electrons
Phelps, A. V. in [He, Ar, Kr, Xe] from Transport Coefficient.
 Phys. Rev., Vol. 136A, 1964, p. 1538.
33. Eu, B. C. On the Energy Dependence of Reaction Cross Section
Liu, W. S. Near Threshold. J. Chem. Phys., Vol. 63, No. 1,
 July 1975, pp. 592-593.
34. Zapesochuyi, I. P. On the Excitation Cross Sections of 2p Levels of
Felston, P. V. Argon, Krypton, and Xenon. Opt. Spectrosc., Vol.
 20, 1966, p. 291.
35. Hinnov, E. Electron-Ion Recombination in Dense Plasmas. Phys.
Hirschberg, J. G. Rev., Vol. 125, 1962, p. 795.
36. Byron, S. Electron-Ion Recombination by Collisional and
Stabler, R. C. Radiative Processes. Phys. Rev. Letters, Vol. 8,
Bortz, P. I. 1962, p. 376.
37. Camac, M. A Multitemperature Boundary Layer. AIAA Paper No.
Kemp, W. H. 63-460, Aug. 1963, MIT, Cambridge, Mass.
38. Brown, R. T. Measurements in a Nonequilibrium Plasma Boundary
Mitchner, M. Layer. Phys. Fluids, Vol. 14, No. 5, May 1971, pp.
 933-940.
39. Whitten, B. T. An Interferometric Investigation of Quasi-Steady
 Shock-Induced Boundary Layers in Partially Ionized
 Argon. UTIAS Report, University of Toronto, 1978.
40. Greenspan, D. Introductory Numerical Analysis of Elliptic Boundary
 Value Problems. Harper and Row, 1965.
41. Liu, W. S. A Model for Calculating the Compactness and Drift
Neralla, V. R. for Ice Floes. Paper presented at the Symposium
Dannard, M. B. (June 8-10, 1976), Forecast and Research Division,
 Atmospheric Environment Service, Toronto.
42. Ames, W. F. Nonlinear Partial Differential Equations in Engin-
 eering. Academic Press, 1965.
43. Douglas, J., Jr. On predictor-Corrector Methods for Nonlinear
Jones, B. F., Jr. Parabolic Differential Equations. J. Soc. Indus.
 and Appl. Math., Vol. 11, No. 1, March 1963, pp.
 195-204.

44. Fannelop, T. K. A Method of Solving the Three-Dimensional Laminar Boundary-Layer Equations with Application to a Lifting Re-entry Body. AIAA J., Vol. 6, No. 6, June, 1968, pp. 1075-1084.
45. Sells, C. C. L. Two-Dimensional Laminar Compressible Boundary Layer Programme for a Perfect Gas. Royal Aircraft Est., TR.66243, Aug. 1966.
46. Chan, Y. Y. Computations of Incompressible Boundary Layer with Suction and Injection. CASI Trans., Vol. 4, No. 2, Sept. 1971, pp. 108-115.
47. Crandall, S. H. An Optimum Implicit Recurrence Formula for the Heat Conduction Equation. Q. Appl. Math., Vol. 13, 1955, p. 318.
48. Smolderen, J. J. In Introduction to Computational Fluid Dynamics. von Karman Inst. for Fluid Dynamics, Lecture Series 74, 1975.
49. Douglas, J., Jr. On the Numerical Integration of Quasi-Linear Parabolic Differential Equations. Pacif. J. Math., Vol. 6, 1956, p. 35
50. Bristow, M. P. F. An Experimental Determination of the Polarizability for Singly Ionized Argon. UTIAS Report No. 158, 1971.
51. Brimelow, P. I. An Interferometric Investigation of Shock Structure and Its Induced Shock-Tube Boundary Layer in Ionized Argon. UTIAS Technical Note No. 187, 1974.
52. Tang, F. C. Effects of Impurities on Shock Wave Stability and Structure in Ionizing Monatomic Gases. M.S. Thesis, UTIAS Technical Note No. 212, 1977.
53. Bredfeldt, H. R.
Scharfman, W. E.
Guthart, H.
Morita, T. Boundary-Layer Ion Density Profiles as Measured by Electrostatic Probes. AIAA J., Vol. 5, No. 1, Jan. 1967, pp. 91-97.
54. Mirels, H. Flow Nonuniformity in Shock Tubes Operating at Maximum Test Times. Phys. Fluids, Vol. 9, pp. 1907-1912, 1966.
55. Enomoto, Y. Wall Boundary Layer Effects on Ionizing Shock Structure in Argon. J. Phys. Soc., Japan, Vol. 35, 1973, p. 1208.
56. Kuiper, R. Interferometric Study of the Nonequilibrium Shock Reflection Process and Thermal Layer in Ionizing Argon. SUDAAR No. 353, Stanford University, 1968.
57. Liu, W. S.
Whitten, B. T.
Glass, I. I. Ionizing Argon Boundary Layers: I. Quasi-Steady Flat-Plate Laminar Boundary Layer Flows. J. Fluid Mech. Vol. 84, Pt. 1, 1978, pp. 55-77.

58. Liu, W. S.
Glass, I. I.

Ionizing Argon Boundary Layers: 2. Shock-Tube Sidewall
Boundary Layer Flows. J. Fluid Mech. (in press),
1978.

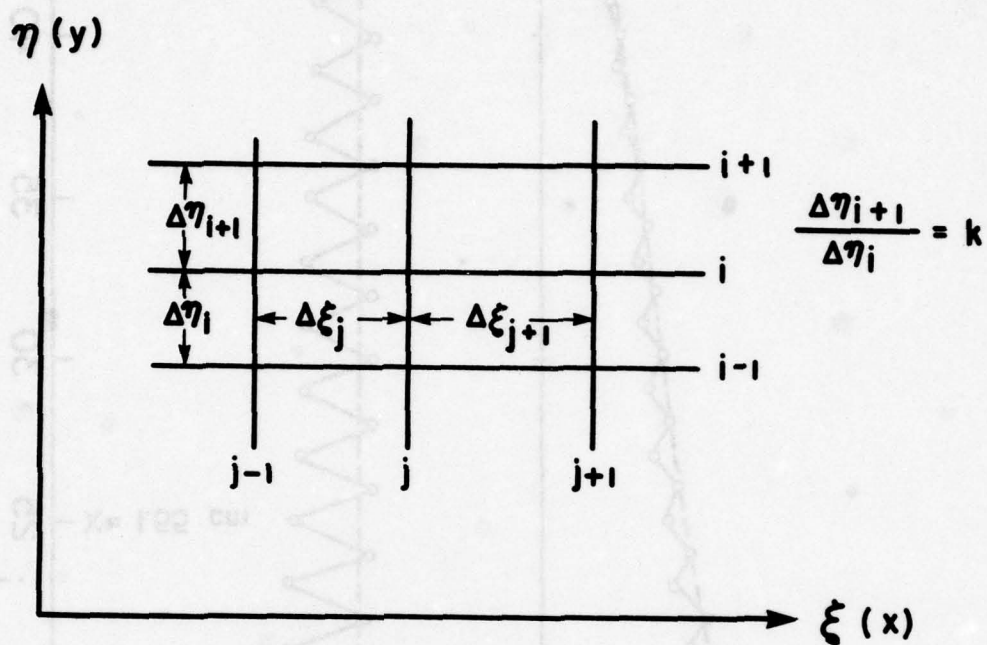


FIG. 1 GRID POINTS FOR FINITE DIFFERENCE SCHEMES.

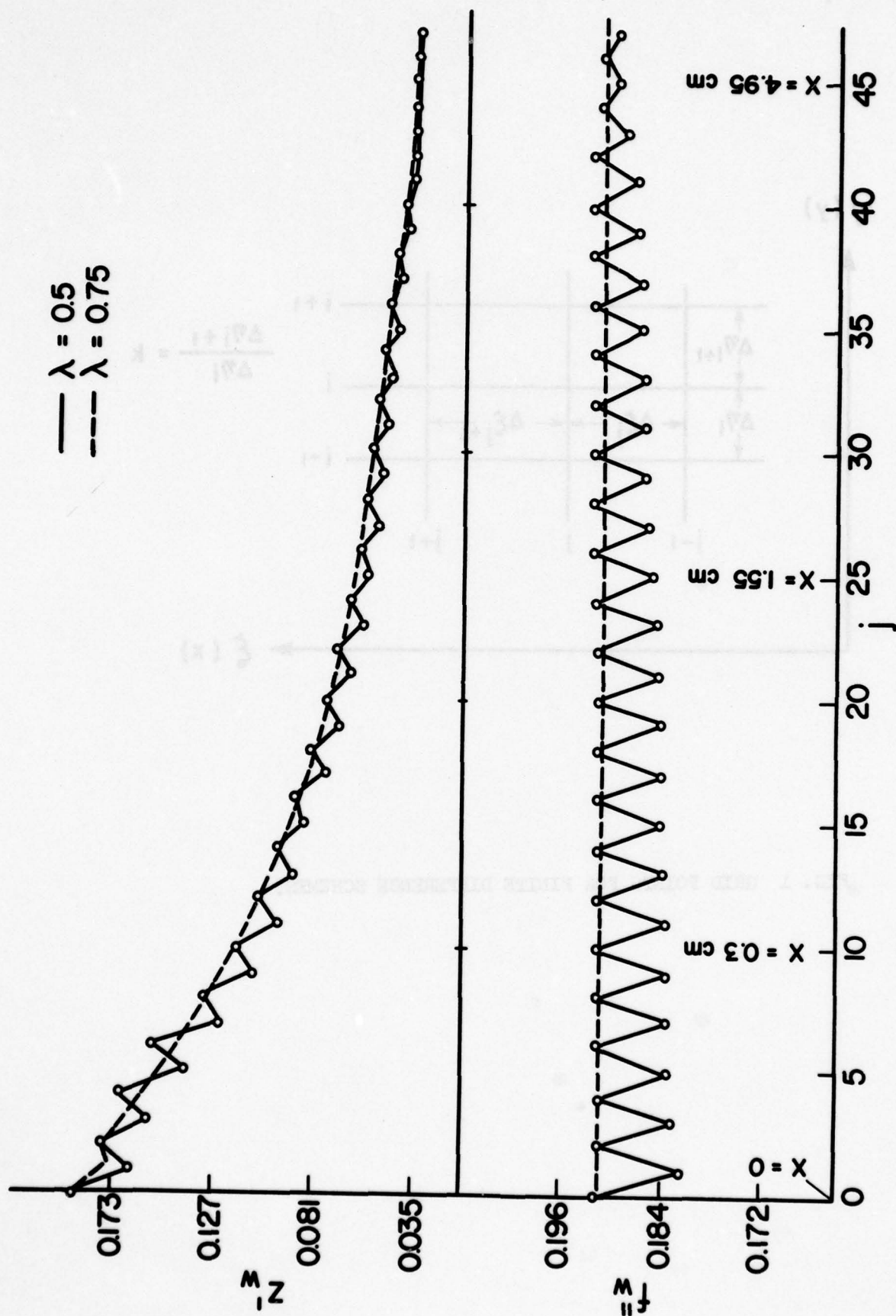


FIG. 2 VARIATIONS OF f'' AND z'' WITH STEP NUMBER j FOR $\lambda = 0.5$ AND 0.75 .
 FREESTREAM CONDITIONS ARE $u_0 = 3.53 \times 10^5 \text{ CM/S}$, $T_{a0} = T_{e0} = 10590 \text{ K}$,
 $\alpha_0 = 0.031$ AND $P_0 = 1200 \text{ TORR}$.

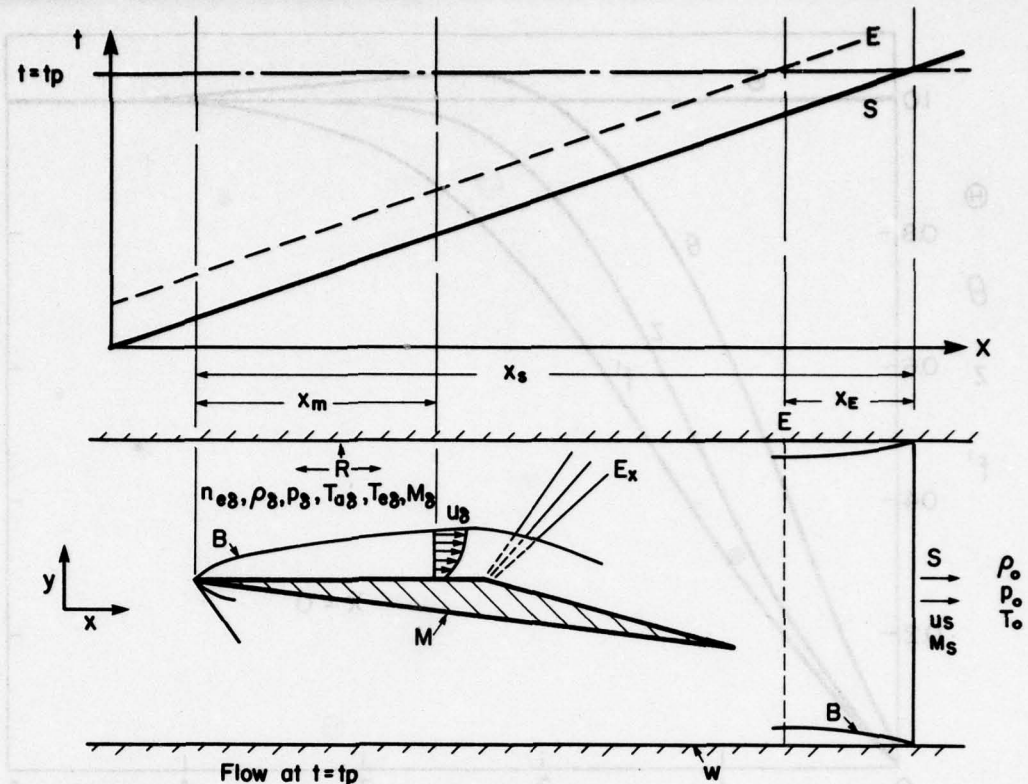


FIG. 3 SCHEMATIC DIAGRAM OF A FLAT-PLATE BOUNDARY-LAYER FLOW GENERATED BY A SHOCK WAVE (MOVING FROM LEFT TO RIGHT) IN A SHOCK TUBE. S - TRANSLATIONAL SHOCK WAVE; x_E - IONIZATION RELAXATION ZONE; E - ELECTRON CASCADE FRONT; W - SHOCK-TUBE WALLS; E_x - EXPANSION WAVE; B - BOUNDARY LAYER; M - FLAT-PLATE MODEL; R - RADIATIVE COOLING ZONE; OTHER QUANTITIES AS DEFINED IN THE TEXT.

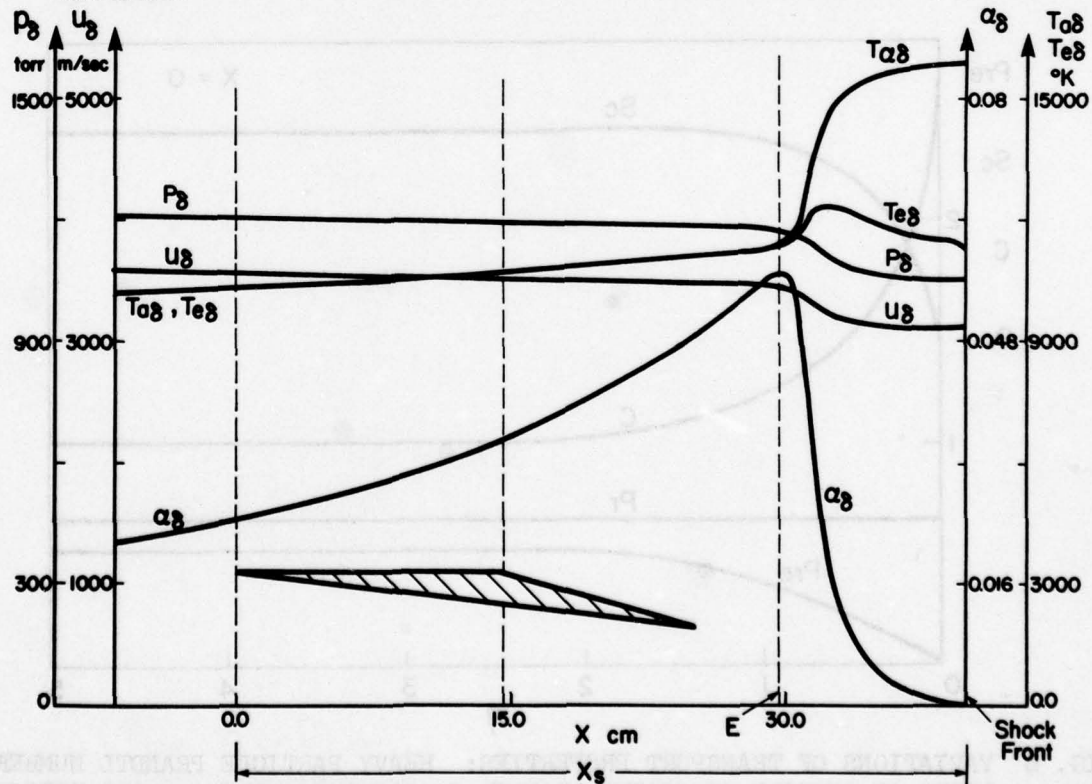


FIG. 4 VARIATION OF FREESTREAM CONDITIONS AT EDGE OF BOUNDARY-LAYER FLOW WITH FLAT-PLATE LEADING-EDGE DISTANCE x FOR $M_8 = 12.8$, $p_0 = 5.01$ TORR AND $T_0 = 297$ K.

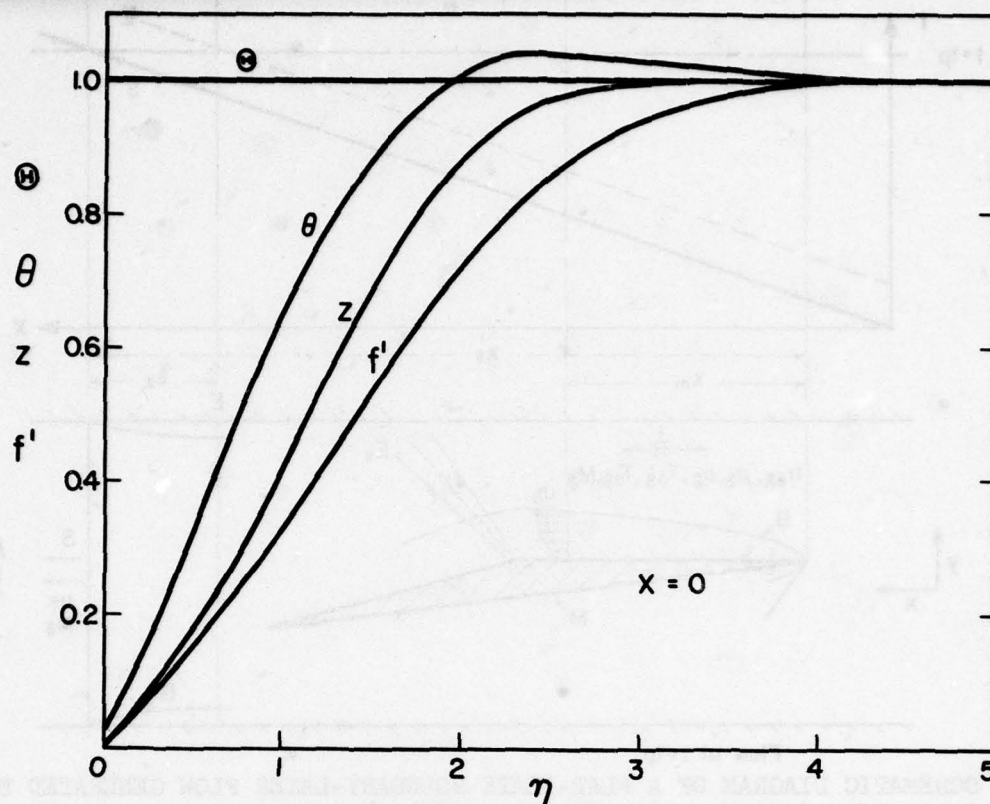


FIG. 5 INITIAL FLOW PROFILES AT $x = 0$ FOR NORMALIZED VELOCITY f' , DEGREE OF IONIZATION z , ATOM TEMPERATURE θ AND ELECTRON TEMPERATURE θ WITH η FOR $M_s = 16.6$, $p_0 = 4.81$ TORR AND $T_0 = 296$ K (CASE 1).

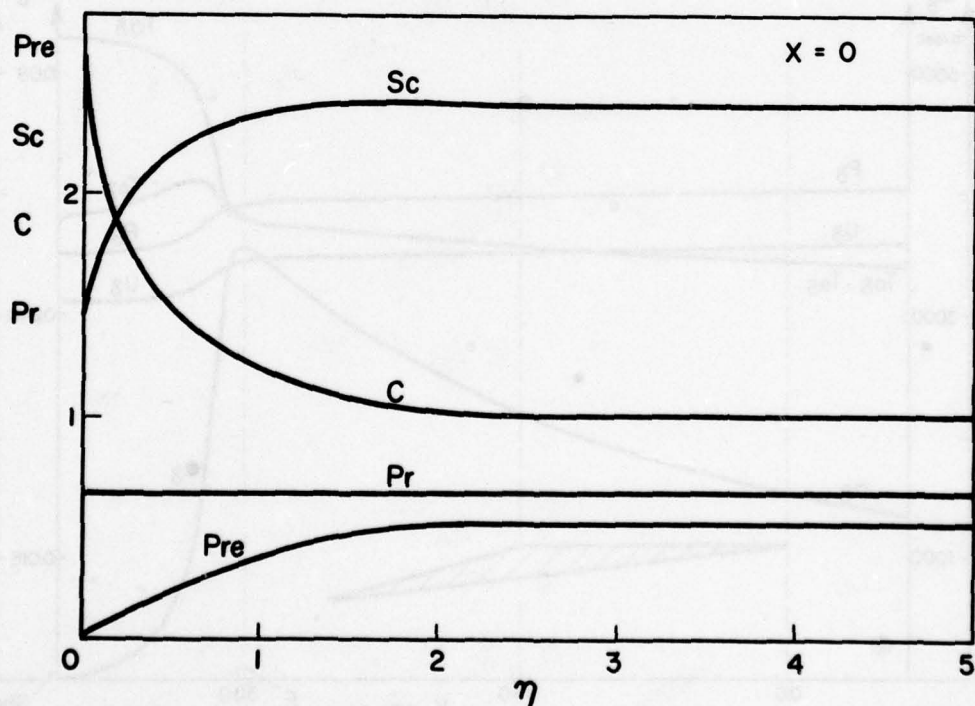


FIG. 6 VARIATIONS OF TRANSPORT PROPERTIES: HEAVY PARTICLE PRANDTL NUMBER Pr , RATIO OF DENSITY-VISCOSITY PRODUCT C , SCHMIDT NUMBER Sc AND ELECTRON PRANDTL NUMBER Pr_e WITH η AT $x = 0$ FOR $M_s = 16.6$, $p_0 = 4.81$ TORR AND $T_0 = 296$ K (CASE 1).

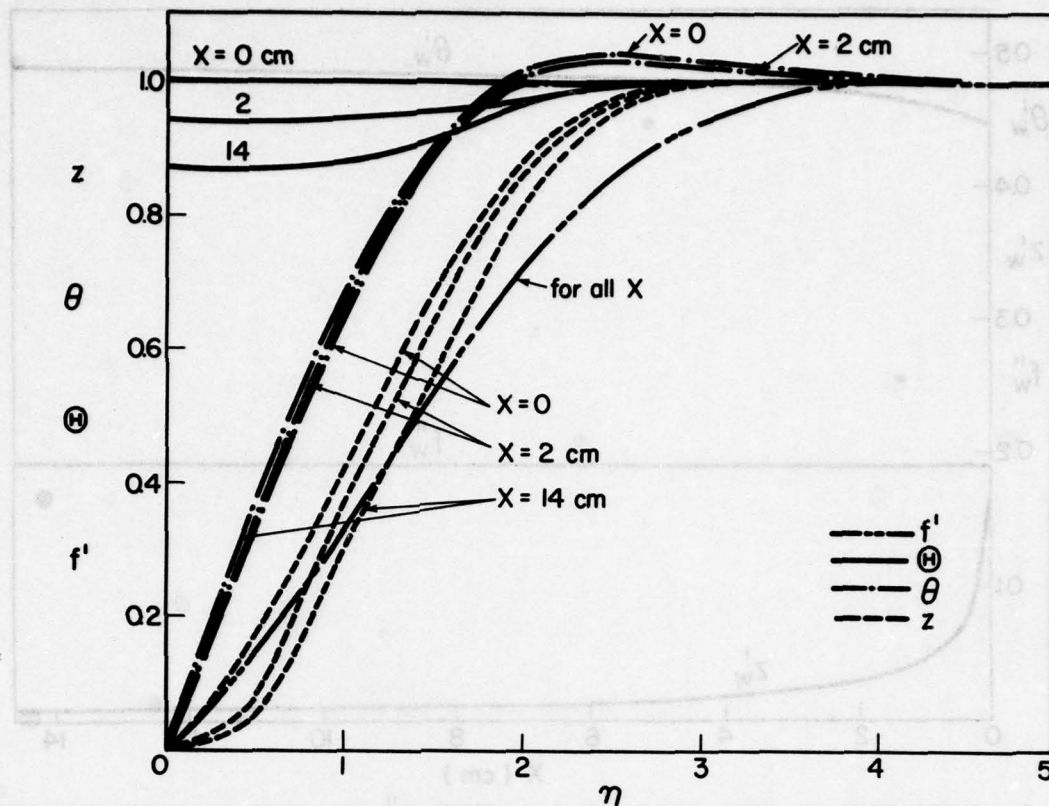


FIG. 7 VARIATIONS OF NORMALIZED FLOW PROFILES OF VELOCITY f' , DEGREE OF IONIZATION z , ATOM TEMPERATURE θ AND ELECTRON TEMPERATURE Θ WITH LEADING-EDGE DISTANCE x FOR $M_s = 16.6$, $p_o = 4.81$ TORR AND $T_o = 296$ K (CASE 1).

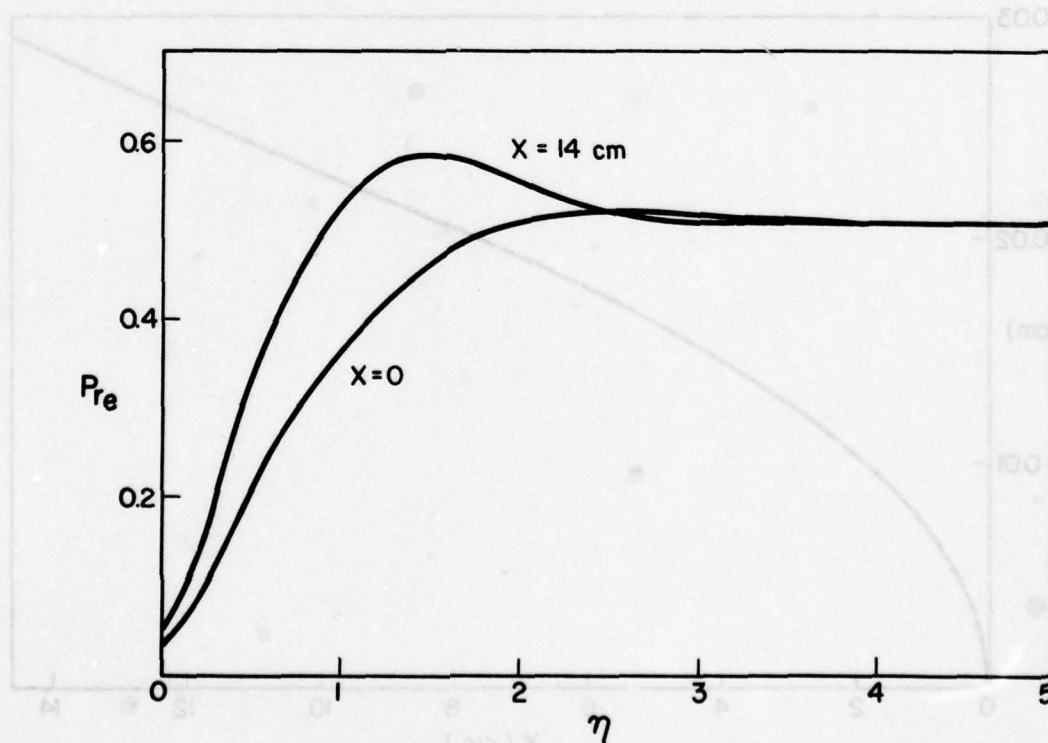


FIG. 8 VARIATION OF ELECTRON PRANDTL NUMBER Pr_e WITH η FOR LEADING-EDGE DISTANCES $x = 0$ AND $x = 14$ CM FOR $M_s = 16.6$, $p_o = 4.81$ TORR AND $T_o = 296$ K (CASE 1).

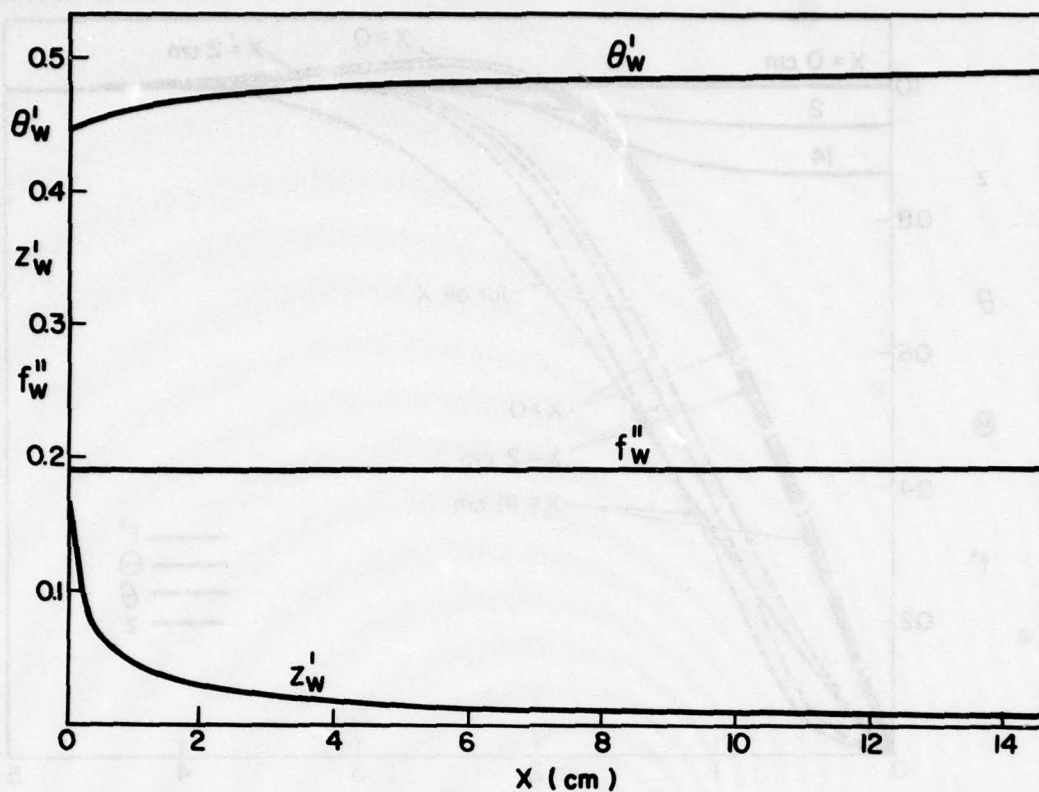


FIG. 9 VARIATIONS OF SKIN FRICTION PARAMETER f''_w AND HEAT-TRANSFER PARAMETERS θ'_w FOR CONDUCTION AND z'_w FOR DIFFUSION WITH LEADING-EDGE DISTANCE FOR $M_s = 16.6$, $p_o = 4.81$ TORR AND $T_o = 296$ K (CASE 1).

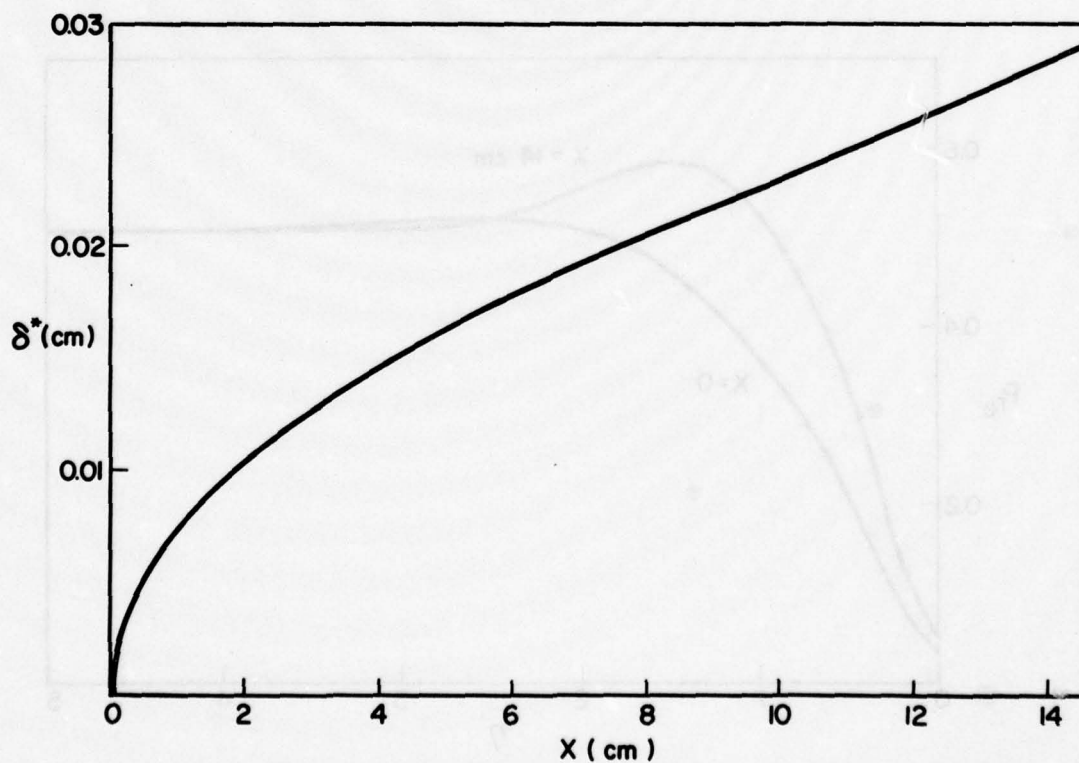


FIG. 10 VARIATION OF BOUNDARY-LAYER DISPLACEMENT THICKNESS δ^* WITH LEADING-EDGE DISTANCE x FOR $M_s = 16.6$, $p_o = 4.81$ TORR AND $T_o = 296$ K (CASE 1).

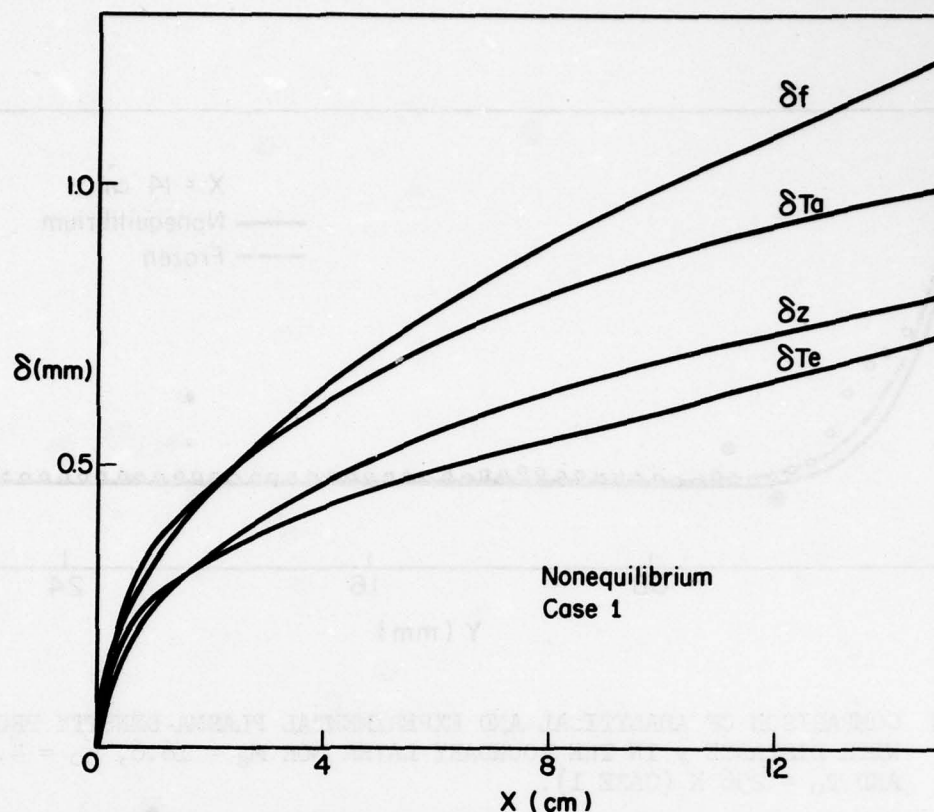


FIG. 11 VARIATIONS OF BOUNDARY-LAYER THICKNESSES OF VELOCITY δ_f , DEGREE OF IONIZATION δ_z , ATOM TEMPERATURE δ_{Ta} AND ELECTRON TEMPERATURE δ_{Te} WITH LEADING-EDGE DISTANCE x FOR $M_s = 16.6$, $p_o = 4.81$ TORR AND $T_o = 296$ K (CASE 1).

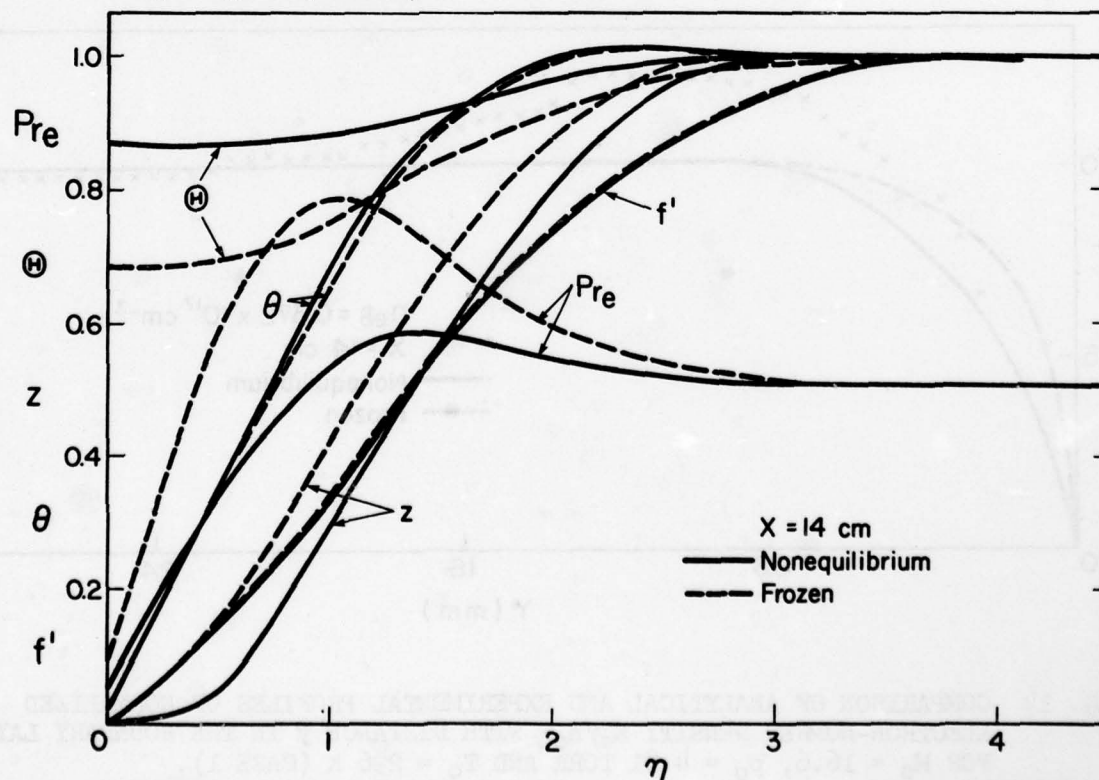


FIG. 12 VARIATIONS OF NORMALIZED PROFILES OF VELOCITY f' , ATOM TEMPERATURE θ , ELECTRON TEMPERATURE θ , DEGREE OF IONIZATION z AND ELECTRON PRANDTL NUMBER Pr_e WITH η AT LEADING-EDGE DISTANCE $x = 14$ CM FOR NONEQUILIBRIUM AND FROZEN FLOWS FOR $M_s = 16.6$, $p_o = 4.81$ TORR AND $T_o = 296$ K (CASE 1).

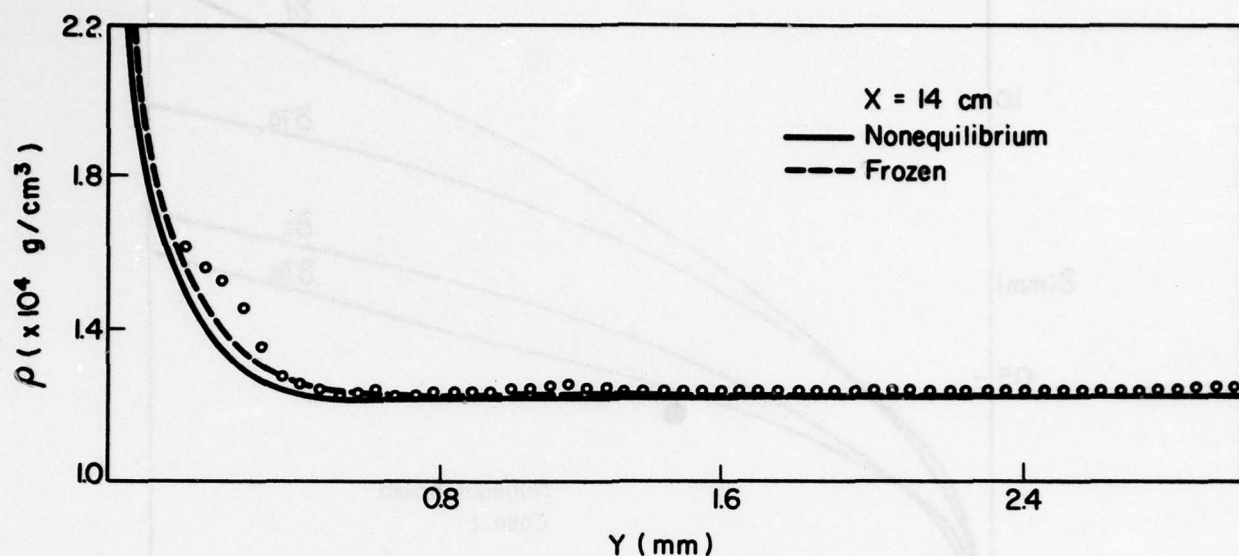


FIG. 13 COMPARISON OF ANALYTICAL AND EXPERIMENTAL PLASMA-DENSITY PROFILE ρ WITH DISTANCE y IN THE BOUNDARY LAYER FOR $M_s = 16.6$, $p_o = 4.81$ TORR AND $T_o = 296$ K (CASE 1).

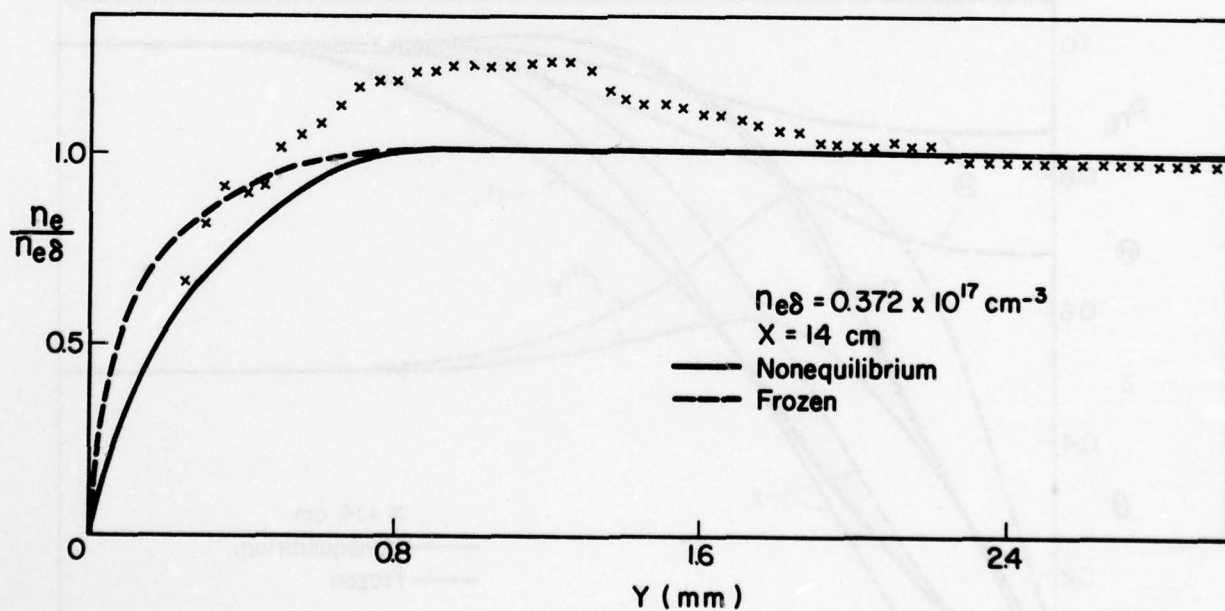


FIG. 14 COMPARISON OF ANALYTICAL AND EXPERIMENTAL PROFILES OF NORMALIZED ELECTRON-NUMBER DENSITY $n_e/n_{e\delta}$ WITH DISTANCE y IN THE BOUNDARY LAYER FOR $M_s = 16.6$, $p_o = 4.81$ TORR AND $T_o = 296$ K (CASE 1).

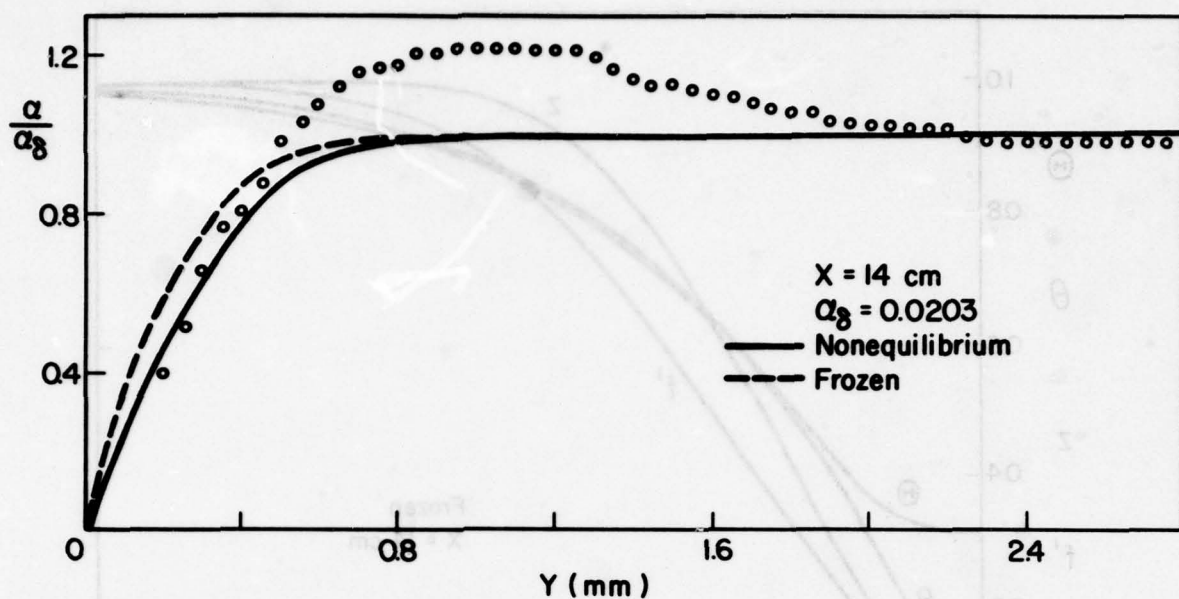


FIG. 15 COMPARISON OF ANALYTICAL AND EXPERIMENTAL PROFILES OF NORMALIZED DEGREE OF IONIZATION α/α_0 WITH DISTANCE y IN THE BOUNDARY LAYER FOR $M_s = 16.6$, $p_0 = 4.81$ TORR AND $T_0 = 296$ K (CASE 1).

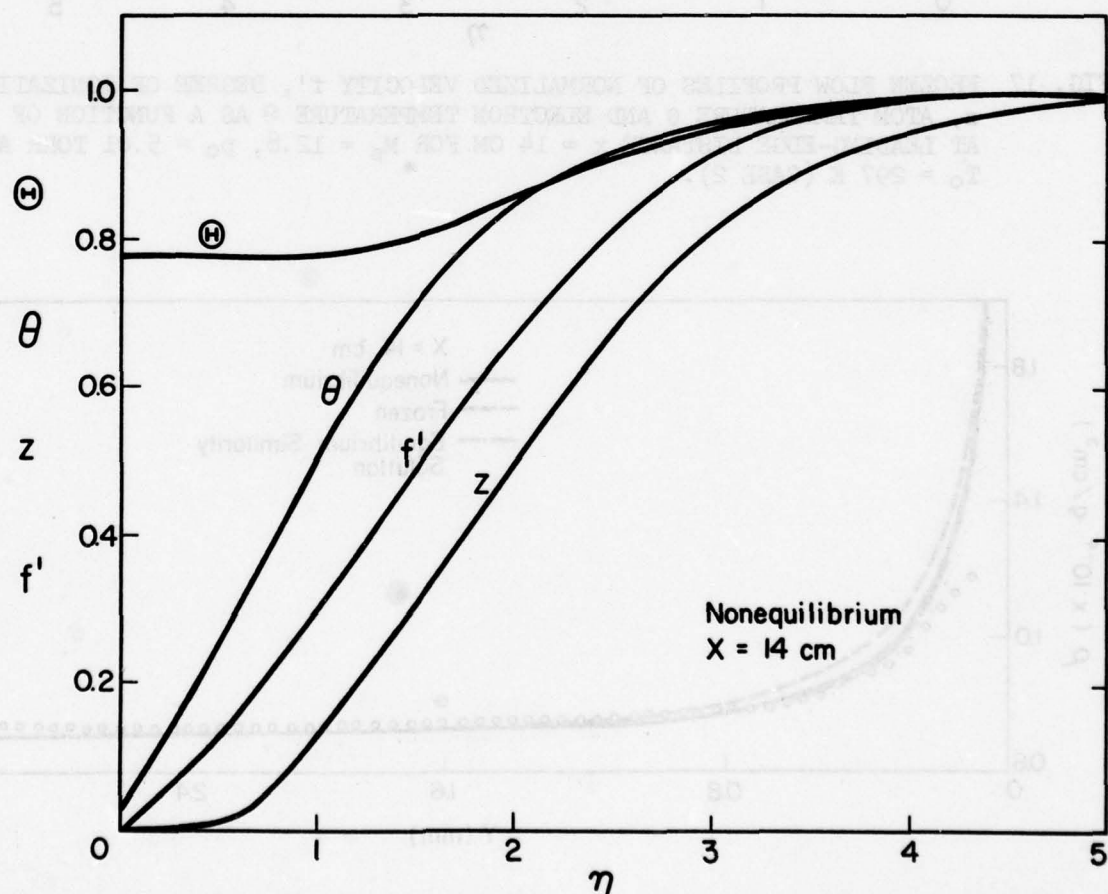


FIG. 16 NONEQUILIBRIUM-FLOW PROFILES OF NORMALIZED VELOCITY f' , DEGREE OF IONIZATION z , ATOM TEMPERATURE θ AND ELECTRON TEMPERATURE θ AS A FUNCTION OF η AT LEADING-EDGE DISTANCE $x = 14$ CM FOR $M_s = 12.8$, $p_0 = 5.01$ TORR AND $T_0 = 297$ K (CASE 2).

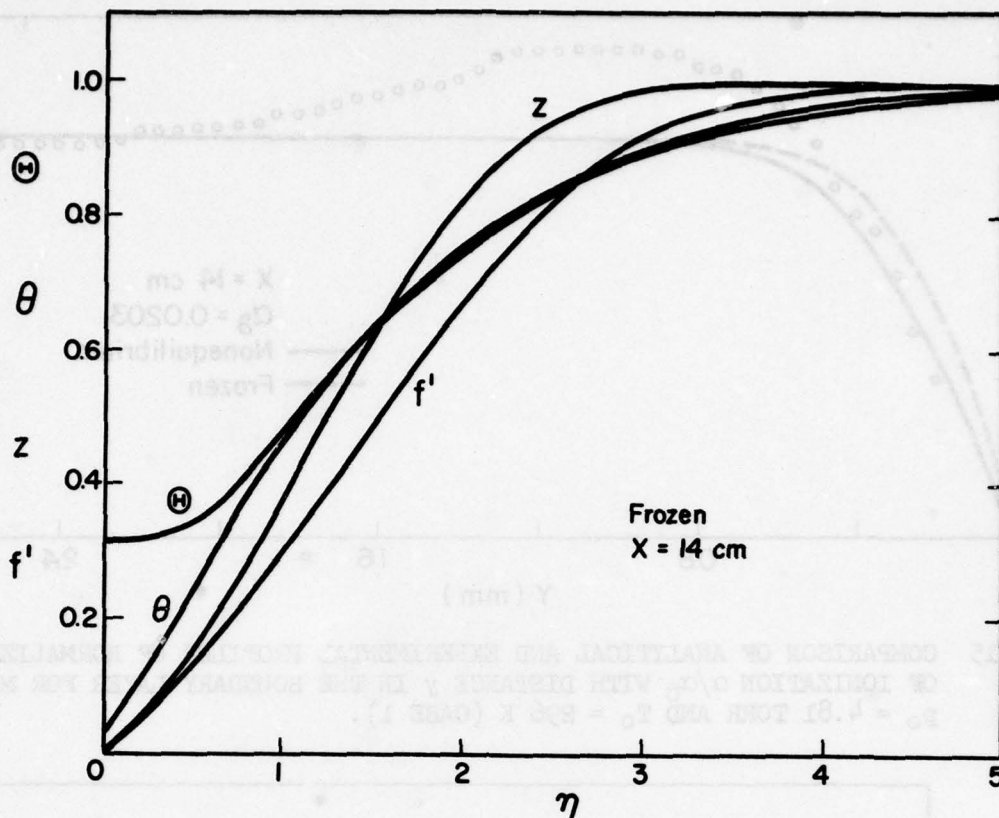


FIG. 17 FROZEN FLOW PROFILES OF NORMALIZED VELOCITY f' , DEGREE OF IONIZATION z , ATOM TEMPERATURE θ AND ELECTRON TEMPERATURE θ AS A FUNCTION OF η AT LEADING-EDGE DISTANCE $x = 14$ CM FOR $M_s = 12.8$, $p_0 = 5.01$ TORR AND $T_0 = 297$ K (CASE 2).

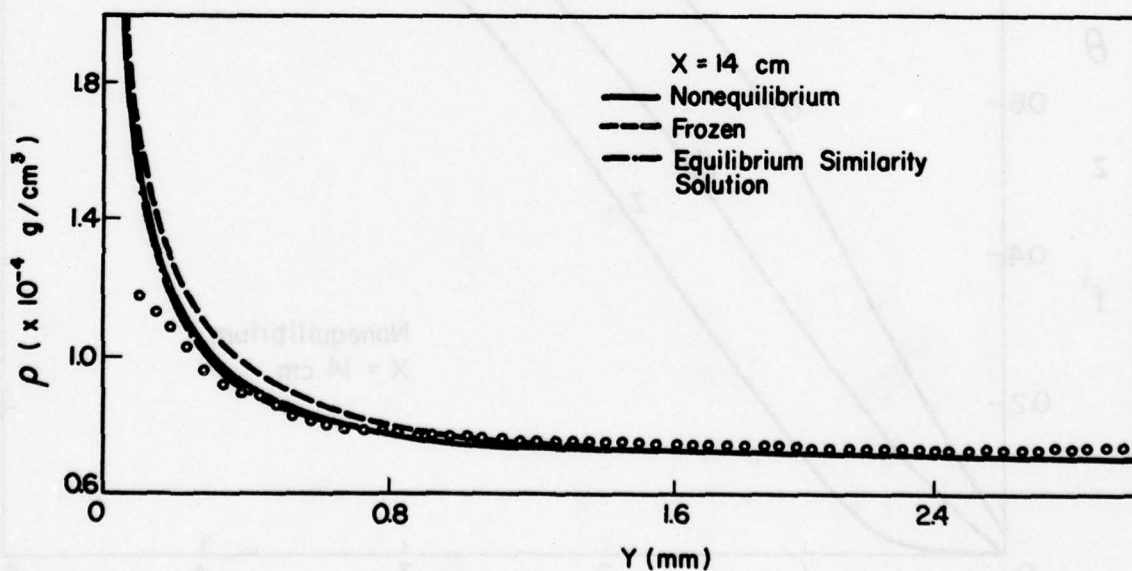


FIG. 18 COMPARISON OF ANALYTICAL AND EXPERIMENTAL PLASMA-DENSITY PROFILE ρ WITH DISTANCE y IN THE BOUNDARY LAYER FOR $M_s = 12.8$, $p_0 = 5.01$ TORR AND $T_0 = 297$ K (CASE 2).

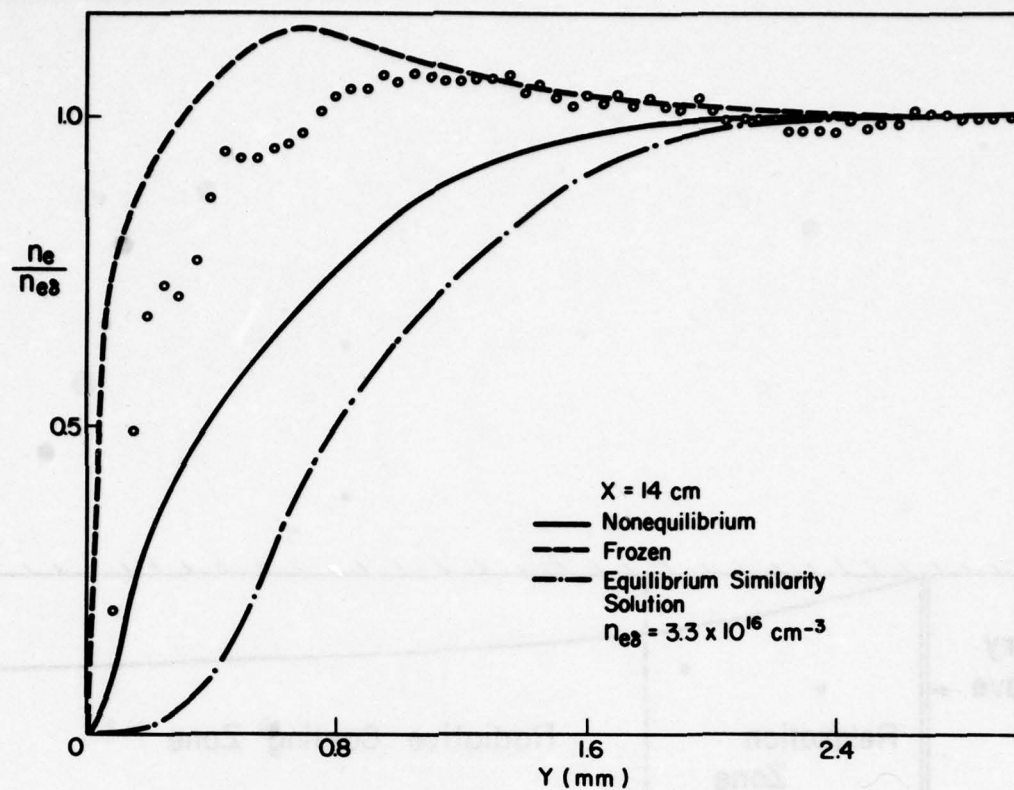


FIG. 19 COMPARISON OF ANALYTICAL AND EXPERIMENTAL PROFILES OF NORMALIZED ELECTRON NUMBER DENSITY $n_e/n_{e\delta}$ WITH DISTANCE y IN THE BOUNDARY LAYER FOR $M_s = 12.8$, $p_0 = 5.01$ TORR AND $T_0 = 297$ K (CASE 2).

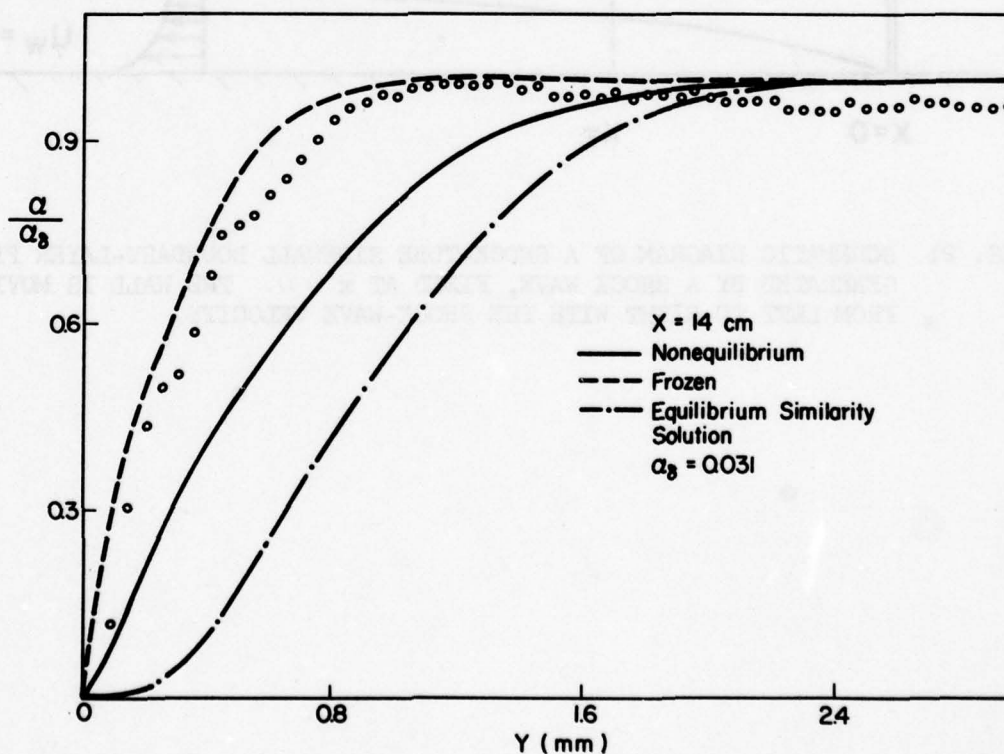


FIG. 20 COMPARISON OF ANALYTICAL AND EXPERIMENTAL PROFILES OF NORMALIZED DEGREE OF IONIZATION α/α_δ WITH DISTANCE y IN THE BOUNDARY LAYER FOR $M_s = 12.8$, $p_0 = 5.01$ TORR AND $T_0 = 297$ K (CASE 2).

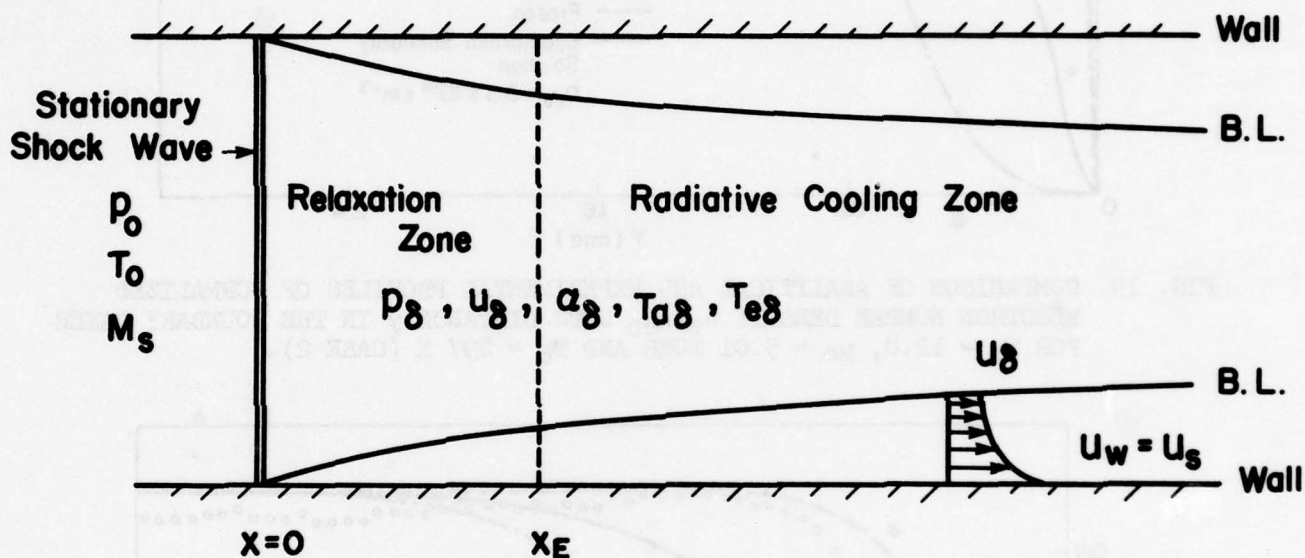


FIG. 21 SCHEMATIC DIAGRAM OF A SHOCK-TUBE SIDEWALL BOUNDARY-LAYER FLOW GENERATED BY A SHOCK WAVE, FIXED AT $x = 0$. THE WALL IS MOVING FROM LEFT TO RIGHT WITH THE SHOCK-WAVE VELOCITY.

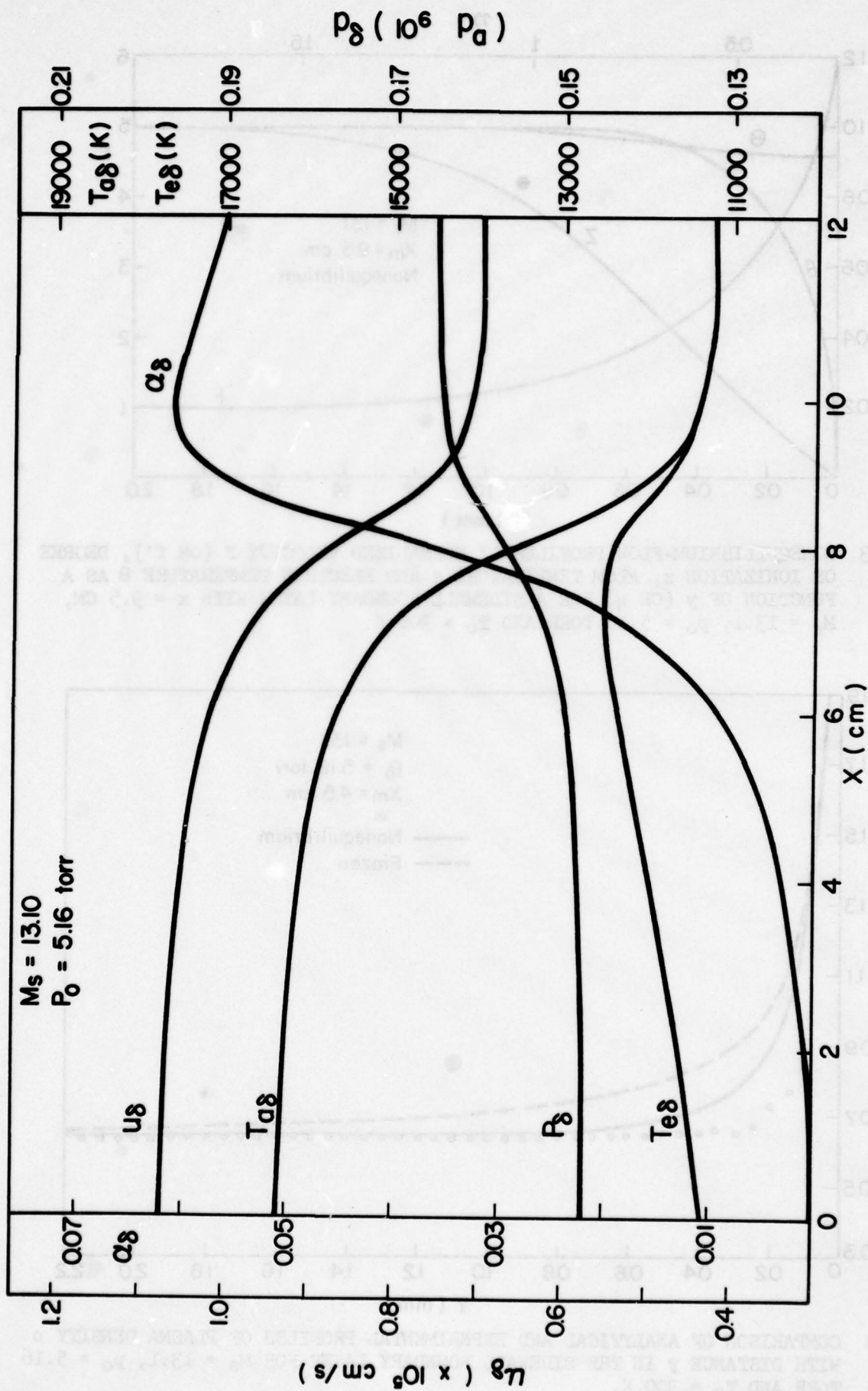


FIG. 22 FREESTREAM CONDITIONS OF THE SHOCK-TUBE SIDEWALL BOUNDARY LAYER GENERATED BY A SHOCK WAVE WITH $M_s = 13.1$, $P_0 = 5.16$ TORR AND $T_0 = 300$ K.

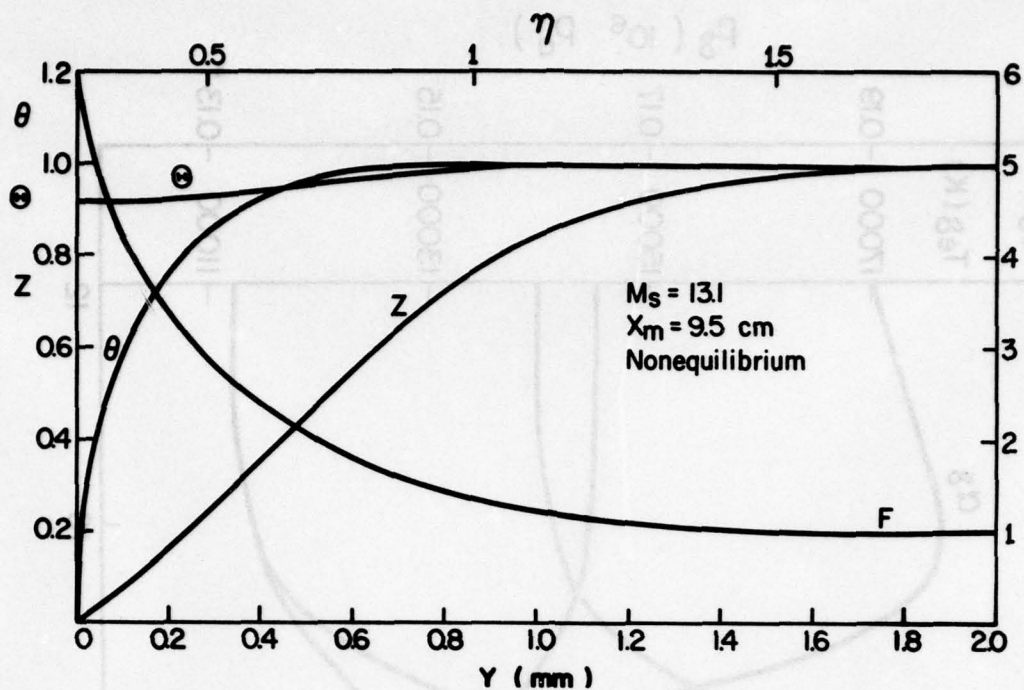


FIG. 23 NONEQUILIBRIUM-FLOW PROFILES OF NORMALIZED VELOCITY F (OR f'), DEGREE OF IONIZATION z , ATOM TEMPERATURE θ AND ELECTRON TEMPERATURE θ AS A FUNCTION OF y (OR η) FOR A SIDEWALL BOUNDARY LAYER WITH $x = 9.5$ CM, $M_s = 13.1$, $p_0 = 5.16$ TORR AND $T_0 = 300$ K.

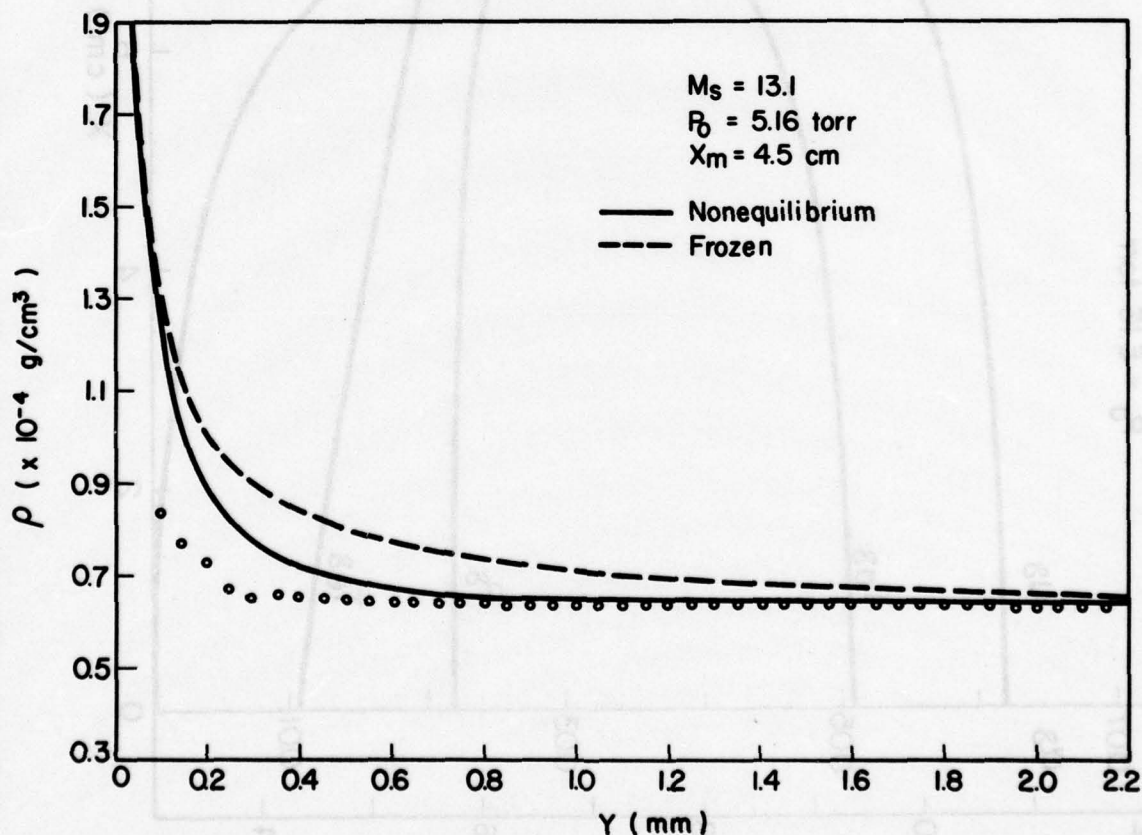


FIG. 24 COMPARISON OF ANALYTICAL AND EXPERIMENTAL PROFILES OF PLASMA DENSITY ρ WITH DISTANCE y IN THE SIDEWALL BOUNDARY LAYER FOR $M_s = 13.1$, $p_0 = 5.16$ TORR AND $T_0 = 300$ K.

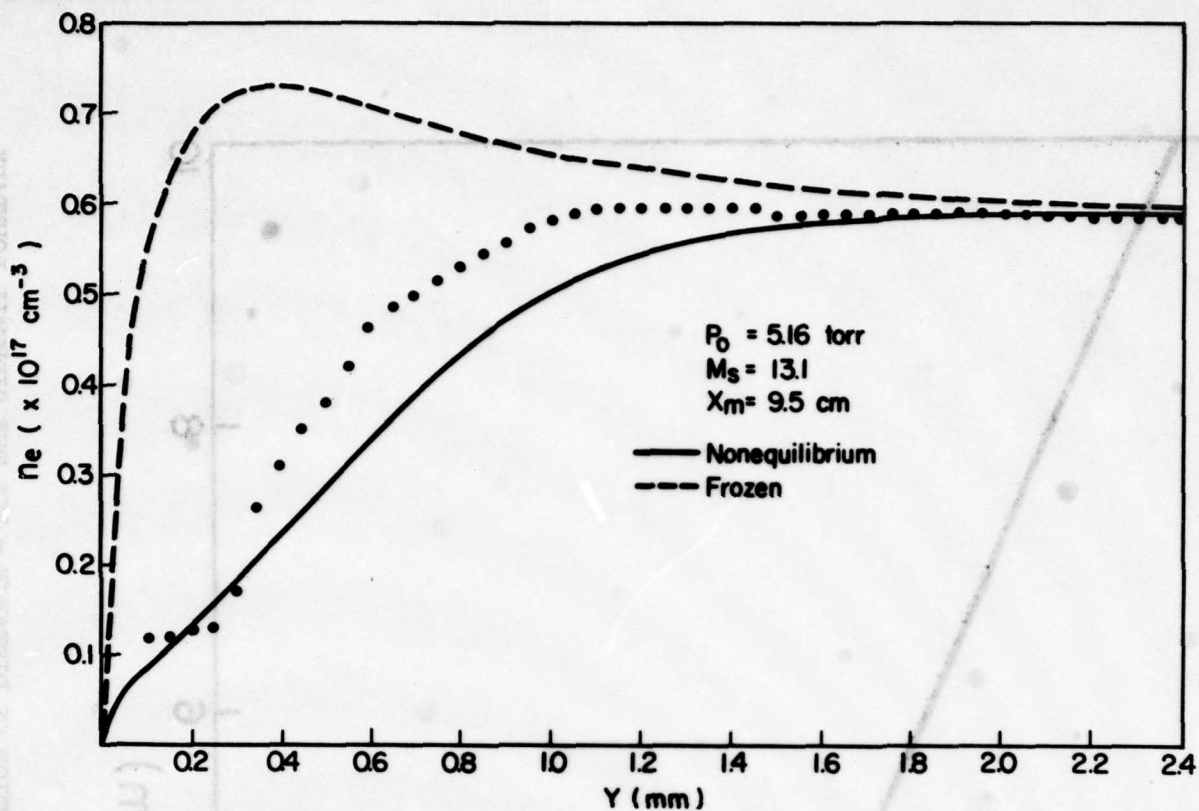


FIG. 25 COMPARISON OF ANALYTICAL AND EXPERIMENTAL PROFILES OF ELECTRON-NUMBER DENSITY n_e WITH DISTANCE y IN THE SIDEWALL BOUNDARY LAYER FOR $M_s = 13.1$, $P_0 = 5.16 \text{ TORR}$ AND $T_0 = 300 \text{ K}$.

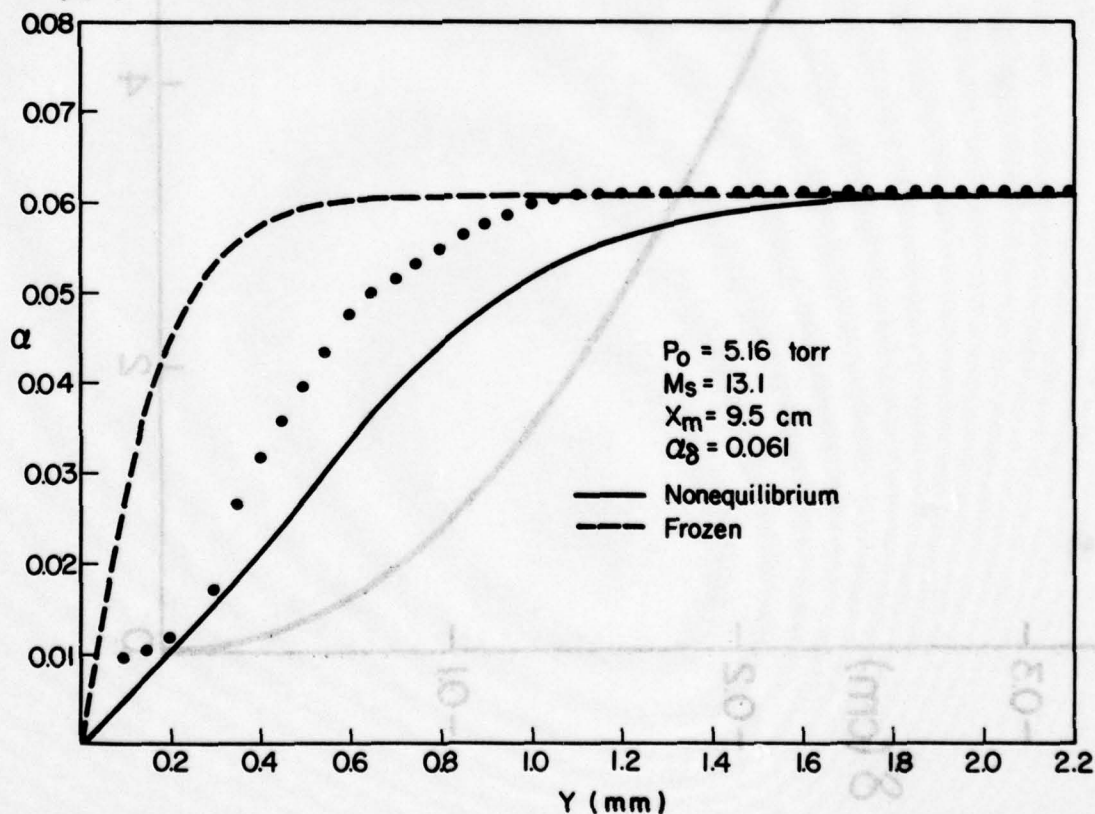


FIG. 26 COMPARISON OF ANALYTICAL AND EXPERIMENTAL PROFILES OF DEGREE OF IONIZATION α WITH DISTANCE y IN THE SIDEWALL BOUNDARY LAYER FOR $M_s = 13.1$, $P_0 = 5.16 \text{ TORR}$ AND $T_0 = 300 \text{ K}$.

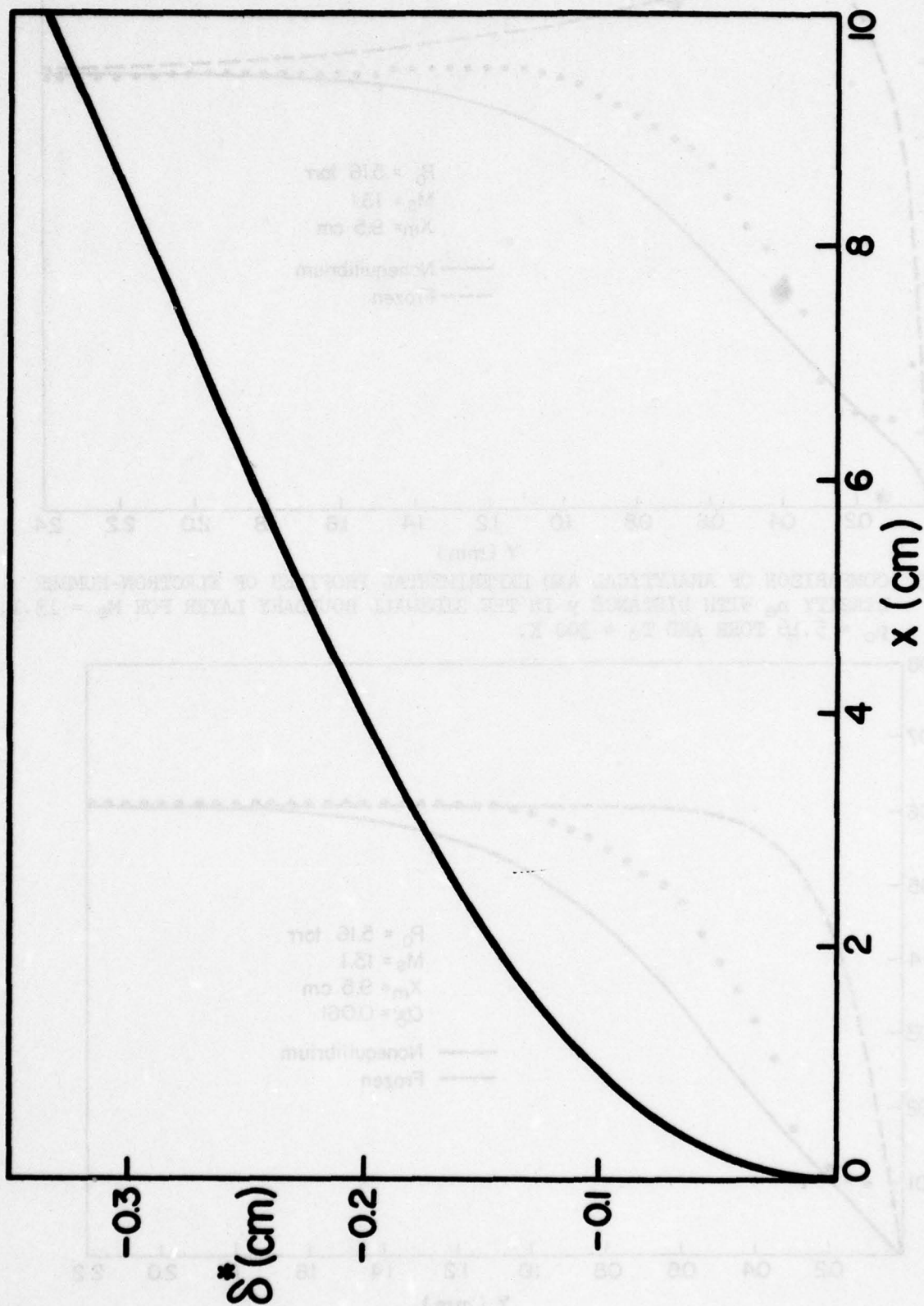


FIG. 27 BOUNDARY-LAYER DISPLACEMENT THICKNESS δ^* AS A FUNCTION OF DISTANCE x FOR THE SIDEWALL BOUNDARY LAYER FOR $M_s = 13.1$, $P_0 = 5.16$ TORR AND $T_0 = 300$ K.

APPENDIX A

DESCRIPTION OF COMPUTER PROGRAM

The program BLEIG for solving Boundary Layer Equations for Ionizing Gases is written on CDC-6600. The other versions of BLEIG on IBM-370 and PDP-10 have been written. The CGS unit system is used through all programs. The flow chart of the program is given in Fig. 28. Free format of the input data is used. The computer program is given in Appendix F.

A.1 Main Program

Before describing the notations used in the main program, the main features of the calculation procedure will be reviewed. A rectangular grid system indicated in Fig. 1 has been adopted, the j -lines running in the η (or y) direction, i.e., normal to the plate, and the i -lines in the ξ (or x) direction, i.e., parallel to the plate. Conditions along some initial j -line are known and the conditions along the $(j+1)$ -line have to be determined. The main steps in the procedure are then,

- (1) If this is an original run, the solutions of the flow at leading edge ($x=0$) are obtained by calling SUBROUTINES SETUP and BEGIN. If this is not the original run, then the solutions at some particular point of x are read in from a restart file in a magnetic tape.
- (2) From the known solutions of F , z , θ and Θ on the j -line, the solutions at $(j+1)$ -line are assumed.
- (3) Using assumed solutions at $(j+1)$ -line, the new velocity profile F at $(j+1)$ -line is calculated.
- (4) Using new value F and assumed z , θ and Θ values, the new value of z is calculated.
- (5) Using new values of F and z and assumed values of θ and Θ , new value of θ is calculated.
- (6) Using new values of F , z and θ and assumed Θ value, new Θ value is calculated.
- (7) Repeat from step (3) to step (6) until the solutions at $(j+1)$ -line converge to satisfy a preset criterion.
- (8) Calculate the boundary-layer characters and determine a suitable step-size Δx .
- (9) Use the same procedure to advance from the $(j+1)$ -line to the $(j+2)$ -line and so on.

The notations used in the main program are listed and explained below:

EDU (MREAD) = U_δ values at the edge of boundary layer.
 EDTA (MREAD) = $T_{a\delta}$ values at the edge of boundary layer.
 EDTE (MREAD) = $T_{e\delta}$ values at the edge of boundary layer.
 EDALP (MREAD) = α_δ values at the edge of boundary layer.
 EDP (MREAD) = p_δ values at the edge of boundary layer.
 XDIS (MREAD) = Reading x values for the freestream conditions.
 DENNE (I) = n_e at grid point (i, j+1).
 WF (I) = F at grid point (i, j+1).
 WZ (I) = z at grid point (i, j+1).
 WTA (I) = θ at grid point (i, j+1).
 WTE (I) = Θ at grid point (i, j+1).
 SF (I) = f at grid point (i, j+1).
 SFX (I) = f_ξ at grid point (i, j+1).
 WFP (I) = F at grid point (i, j).
 WZP (I) = z at grid point (i, j).
 WIAP (I) = θ at grid point (i, j).
 WTEP (I) = Θ at grid point (i, j).
 GUESS (4) = Initial guess values of $[Cf']_w$, $\left[\frac{C}{Sc} z' \right]_w$, $\left[\frac{C}{Pr} \theta' \right]_w$
 and Θ_w .
 WORK (I) = A function evaluated at (i, j+1).
 F(I) = Weighted F value at (i, j+1).
 Z (I) = Weighted z value at (i, j+1).
 THETA (I) = Weighted θ value at (i, j+1).
 THETE (I) = Weighted Θ value at (i, j+1).
 ELAY (I) = η at (i, j+1).
 YREAL (I) = y at (i, j+1).
 CR (I) = C at (i, j+1).

CRPR (I)	=	C/Pr at (i, j+1)
CRSC (I)	=	C/Sc at (i, j+1)
CRPRE (I)	=	C/Pr _e at (i, j+1)
RHO (I)	=	ρ at (i, j+1)
CRP (I)	=	C at (i, j)
CRPRP (I)	=	C/Pr at (i, j)
CRSCP (I)	=	C/Sc at (i, j)
CRPREP (I)	=	C/Pr _e at (i, j)
OLDWF (I)	=	Previous iterative value of F at (i, j+1)
OLDWZ (I)	=	Previous iterative value of z at (i, j+1)
OLDWTA (I)	=	Previous iterative value of θ at (i, j+1)
OLDWTE (I)	=	Previous iterative value of θ at (i, j+1)
LAMD	=	$\bar{\lambda} = (\lambda_a + \lambda_1)$
LAMDE	=	λ_e
MU	=	μ
K	=	k
NA	=	n _a
NE	=	n _e
MUW	=	μ _w
NEDOTA	=	(n _e) _a /n _e
NEDOTE	=	(n _e) _e /n _e
UED	=	U _δ
PED	=	P _δ
TAED	=	T _{aδ}
TEED	=	T _{eδ}
ALPED	=	α _δ
TW	=	T _w

ZW	=	z_w
UW	=	u_w
ROLMUE	=	$\rho_0 \mu_0$
CN	=	λ
DETA1	=	$\Delta \eta_1$
N	=	Maximum value of i
DEX	=	Δt_i
IBC	=	If IBC = 1, sheath-wall condition for T_e is used If IBC = 2, sheath-wall conditions for T_e and α are used
A(I)	=	Matrix element A_i
B(I)	=	Matrix element B_i
C(I)	=	Matrix element C_i
D(I)	=	Matrix element D_i
D1(I)	=	$1/[(1+k)\Delta \eta_1 k^1]$
D2(I)	=	$2/[(1+k)k^{2i-1}\Delta \eta_1^2]$
X(t)	=	X_i
MA	=	m_a
R	=	R
TION	=	T_I
TEXC	=	T^*
SAA	=	S_{aa}^*
SAE	=	S_{ae}^*
TACRI	=	$T_{a,cri}$
TECRI	=	$T_{e,cri}$
QAAC	=	Used in $\sigma_{aa} = QAAC/T_a^{0.25}$
QAIC	=	Used in $\sigma_{ai} = QAIC/T_a^{0.09}$

CC1, CC2, CC3,
CC4, TEEA, DD1,
DD2, DD3, DD4 =

Used in the equation:

$$\sigma_{ea} = (CC1 + CC2 \cdot T_e + CC3 \cdot T_e^2 + CC4 \cdot T_e^3) \times 10^{-16}$$

if $T_e \leq TEEA$

$$\sigma_{ea} = (DD1 + DD2 \cdot T_e + DD3 \cdot T_e^2 + DD4 \cdot T_e^3) \times 10^{-16}$$

if $T_e > TEEA$

EE1, EE2, EE3 = Used to calculate the statistical weight of ion, Z_I ,
see FUNCTION EQK: $ZI = EE1 + EE2/\exp(EE3/T)$

HVC = v_c

ZEFF = Z_{eff}

DX = Δx

XMAX = Maximum value of x

EPS = Tolerance criterion

ITYPE = ITYPE = 1 for flat-plate boundary layer
ITYPE = 2 for sidewall boundary layer

ICASE = ICASE = 1 for nonequilibrium flow
ICASE = 2 for frozen flow

CONTL = Parameter used in the control of step size Δx

YMM = y value in mm

THICKD = displacement thickness δ^* in cm

J = J

XREAL = x in cm

XI = ξ

ITER = Iteration number

IPRNTX = Solution step print selector in x direction. Output
will be printed on the line printer every IPRNTX step

IPRNTY	=	Solution step print selector in y direction. Output will be printed on the line printer every IPRNTY step
IFILE	=	Restart file solution step selector. A restart record will be written to the restart file every IFILE step
FIN	=	Read in restart file name
FOUT	=	Written out restart file name
MREAD	=	Number of points freestream conditions
N1	=	N-1
DWFDY	=	$(\partial F / \partial \eta)_w$
DWZDY	=	$(\partial Z / \partial \eta)_w$
DWTADY	=	$(\partial \theta / \partial \eta)_w$
DWTEDY	=	$(\partial \theta / \partial \eta)_w$
GAML	=	$\rho_\delta \mu_\delta U_\delta$ at (N, j)
GAM2	=	$\rho_\delta \mu_\delta U_\delta$ at (N, j+1)
TAUX	=	$T_{e\delta} / T_{a\delta} = \tau$
ALTAU	=	$\tau \alpha_\delta$
TAUU	=	$2\xi / \rho_\delta \mu_\delta U_\delta^2$
BETAF	=	β_f
BETAZ	=	β_z
BETATA	=	β_{T_a}
BETATE	=	β_{T_e}
TEW	=	T_{ew}
SCW	=	Sc_w
SLOPE	=	z'_w or θ'_w
TA	=	T_a
TE	=	T_e
XIUED	=	$\sqrt{2\xi} / U_\delta$

A.2 Subroutines

Subroutine INTERP:

The Aitken-Lagrange and Lagrange interpolations have been applied before. However, it was found that these interpolations are not suitable for the sidewall boundary layer where the variation of α_δ with x is significant. Therefore, a linear interpolation INTERP is applied in the present program.

Y = The resulting interpolated function value.

X = The argument value specified by input.

M = An input value which specifies the number of points in table (XF, YF).

XF = The input vector of argument.

YF = The input vector of function values of the table.

Subroutine SETUP:

Equations (60) - (63) are the ordinary differential equations with two-point boundary conditions. The Newton-Raphson method for the iteration techniques (see Subroutine BEGIN) is applied. In the BEGIN subroutine, four guess values for $[Cf'']_w$, $[(C/Sc)z']_w$, $[(C/Pr)\theta']_w$ and θ_w (or $[Cf'']_w$, Z_w , $[(C/Pr)\theta']_w$ and θ_w) are required. If the guess initial values are not reasonable, then the computation time is more consumable and stable solutions cannot be found in the Subroutine BEGIN. In order to avoid this difficulty, some knowledge about how to guess the initial values are necessary.

From the integral method described in Ref. 10, the following ways to guess the initial values are presented:

$$\text{GUESS (1)} = \bar{C}_w f''_w \quad (A1)$$

where

$$f'_w = a_1 / \sqrt{\lambda_0 / 2}$$

$$a_1 = 2(1 - \gamma)$$

$$\gamma = U_w / U_\delta$$

$$\lambda_0 = 2a_1 / (F_f \bar{C})$$

$$F_f = (1 - \gamma) \frac{985}{9007} + \frac{227}{1287} \gamma (1 - \gamma)$$

$$\text{GUESS (2)} = \left(\frac{\bar{C}}{Sc} \right) z'_w \quad (A2)$$

where

$$z'_w = \frac{c_1}{\sqrt{\lambda_o/2}}$$

$$c_1 = \frac{\frac{\lambda_o}{2} c_o}{\frac{1}{Sc} + \frac{\lambda_o}{2} c_1}$$

$$c_o = \frac{1}{4} (1 - z_w)(1 - \gamma) + \frac{\gamma}{2} (1 - z_w)$$

$$c_1 = \frac{32}{495} (1 - \gamma) + \frac{\gamma}{10}$$

If $z'_w = 0$ is applied, then GUESS (2) = 1.0.

$$\text{GUESS (3)} = \left(\frac{\bar{C}}{Pr} \right) \theta'_w \quad (A3)$$

where

$$\theta'_w = \frac{b_1}{\sqrt{\lambda_o/2}}$$

$$b_1 = \frac{\frac{\lambda_o}{2} [B_o - B_2 b_2] + G}{\frac{1}{Pr} + \frac{\lambda_o}{2} B_1}$$

$$B_o = \frac{31}{126} (1 - \theta_w)(1 - \gamma) + \frac{1}{2} \gamma (1 - \theta_w)$$

$$B_1 = \frac{821}{12012} (1 - \gamma) + \frac{3}{28} \gamma$$

$$B_2 = \frac{151}{9009} (1 - \gamma) + \frac{\gamma}{42}$$

$$b_2 = -2Pr \frac{U_{\delta}^2}{C_{pTa\delta}} (1 - \gamma)^2$$

$$G = a_1^2 + \frac{a_4^2}{7} + \frac{a_5^2}{9} + \frac{a_6^2}{11} + \frac{a_1 a_4}{2} + \frac{2}{5} a_1 a_5 + \frac{1}{3} a_1 a_6 + \frac{1}{4} a_4 a_5 \\ + \frac{2}{9} a_4 a_6 + \frac{1}{5} a_5 a_6$$

$$a_1 = 2(1 - \gamma)$$

$$a_4 = -5(1 - \gamma)$$

$$a_5 = 6(1 - \gamma)$$

$$a_6 = -2(1 - \gamma)$$

$$\text{GUESS (4)} = \theta_w \quad (\text{A4})$$

Using the boundary condition $\theta_w' = 0$ and Eq. (63), we obtain GUESS (4) = 1.0.

In the above equations, the transport properties, C , Sc , Pr are evaluated at some particular distance η^* from the wall. However, it is difficult to determine η^* from theory. From our experience, the guess transport properties are approximately equal to the average values of that at the freestream and at the wall.

Subroutine INTRG:

This is a subroutine to perform the following integration by three-point difference formulae.

$$z = \int_0^{\eta} y \, d\eta$$

or

$$z = \sum_{i=0}^N \frac{k^{i-1} \Delta\eta_1}{6} \left[\left(\frac{2+3k}{1+k} \right) y(i-1) + \left(\frac{1+3k}{k} \right) y(i) \right. \\ \left. - \frac{1}{k(1+k)} y(i+1) \right]$$

It is worth noting that $I = 1$ in the program corresponds to $i = 0$ here.

Subroutines BEGIN and BLF:

These subroutines are used to solve Eqs. (60) - (63) by means of the Newton-Raphson iteration techniques (Ref. 10). The following notations are applied:

$$YINIT (1) = f_w$$

$$YINIT (2) = f'_w$$

$$YINIT (3) = [Cf'']_w$$

$$YINIT (4) = z_w$$

$$YINIT (5) = \left[\frac{C}{Sc} z' \right]_w$$

$$YINIT (6) = \theta_w$$

$$YINIT (7) = \left[\frac{C}{Pr} \theta' \right]_w$$

$$YINIT (8) = \theta_w$$

$$YINIT (9) = \left[\frac{C}{Pr_e} \theta' \right]_w$$

$$F = f' \equiv u/u_\delta$$

$$Z = z$$

$$THETA = \theta$$

$$THERE = \theta$$

NORD = Number of ordinary differential equations

$$Y (1) = f$$

$$Y (2) = f'$$

$$Y (3) = Cf''$$

$$Y (4) = z$$

$$Y (5) = \frac{C}{Sc} z'$$

$$Y (6) = \theta$$

$$Y (7) = \frac{C}{Pr} \theta'$$

$$Y(8) = \theta$$

$$Y(9) = \frac{C}{Pr_e} \theta'$$

$$YPRIM(i) = Y'(i) \quad i = 1 \text{ to } 9$$

Subroutine RKGIL:

This subroutine uses the Runge-Kutta method with Gill's coefficients for the solution of initial-value problems.

Y = Input vector of initial values, y

YPRIM = y'

NORD = Number of equations

A = Lower bound of the interval

B = Upper bound of the interval

STEP = Step size

DER = An auxiliary storage array of y'

Subroutine DENSIT:

This subroutine is used to calculate n_a , n_e and ρ by given p , T_a , T_e and α .

Subroutine TRANSP:

This subroutine is used to calculate the transport parameters. The following notations are used:

$$QAA = \sigma_{aa}$$

$$QAI = \sigma_{ai}$$

$$QEA = \sigma_{ea}$$

$$QEI = \sigma_{ei}$$

$$QEE = \sigma_{ee}$$

$$QII = \sigma_{ii}$$

$$CA = \left[\frac{\pi k_B T_a}{m_a} \right]^{\frac{1}{2}}$$

$$CE = \left[\frac{\pi k_B T_e}{m_e} \right]^{\frac{1}{2}}$$

$$MU = \mu$$

$$LAMD = \bar{\lambda}$$

$$LAMDE = \lambda_e$$

$$DAMB = D_{amb}$$

$$VEAI = 2 \left(\frac{m_e}{m_a} \right) \left[\frac{\pi k_B T_e}{m_e} \right]^{\frac{1}{2}} (n_a \sigma_{ea} + n_e \sigma_{ei})$$

Subroutine RATES:

This is a subroutine to calculate the reaction rates.

$$NEDOTA = (\dot{n}_e)_a / n_e$$

$$NEDOTE = (\dot{n}_e)_e / n_e$$

$$KFA = k_{fa}$$

$$KRA = k_{ra}$$

$$EQK = K_{eq}$$

$$KFE = k_{fe}$$

$$KRE = k_{re}$$

$$SAA = \text{First excitational cross-section constant between atom and atom}$$

$$SAE = \text{First excitational cross-section constant between atom and electron}$$

Function EQK:

This is a function to calculate the equilibrium rate constant for a given temperature.

ZI = Statistical weight for an ion

EQK = K_{eq}

Function QRAD:

This function is used to calculate the radiation energy loss.

HVC = Cut-off frequency of the plasma

ZEFF = Effective nuclear charge

QC = Continuum radiation energy loss

QRAD = Total radiation energy loss

NE = Electron number density

TE = Electron temperature

Subroutines MINVRS and SUBMCS:

These subroutines are used to calculate the matrix inverse of matrix A. The input matrix and resulting matrix inverse are specified by A.

Subroutines CRANK and TRDG:

Subroutines CRANK and TRDG are an algorithm to solve a tridiagonal matrix most efficiently. The matrix equation is given by

$$A_i W_{i-1} + B_i W_i + C_i W_{i+1} = D_i$$

where $i = 1$ to $N-1$, and W_0 and W_N are given. The matrix form is

$$\begin{bmatrix} B_1^* & C_1 & & & & & & & & \\ A_2 & B_2 & C_2 & & & & & & & \\ & A_3 & B_3 & C_3 & & & & & & \\ & & & & \ddots & & & & & \\ & & & & & \ddots & & & & \\ & & & & & & \ddots & & & \\ & & & & & & & \ddots & & \\ & & & & & & & & \ddots & \\ & & & & & & & & & A_{N-2} & B_{N-2} & C_{N-2} \\ & & & & & & & & & A_{N-1} & B_{N-1} & \\ & & & & & & & & & & & 0 \end{bmatrix} \begin{bmatrix} W_1 \\ W_2 \\ W_3 \\ \vdots \\ \vdots \\ \vdots \\ W_{N-2} \\ W_{N-1} \end{bmatrix} = \begin{bmatrix} D_1^* \\ D_2 \\ D_3 \\ \vdots \\ \vdots \\ \vdots \\ D_{N-2} \\ D_{N-1}^* \end{bmatrix}$$

If W_0 is given, then

$$B_1^* = B_1$$

$$D_1^* = D_1 - A_1 W_0$$

If $(\partial W / \partial \eta)_0$ is given, then

$$B_1^* = A_1 + B_1$$

$$D_1^* = D_1 + A_1 \left(\frac{\partial W}{\partial \eta} \right)_0 \Delta \eta$$

For the present boundary layer case, $W_N (=1)$ is given, and therefore, $D_{N-1}^* = D_{N-1} - C_{N-1}$.

The arguments of CRANK are

IBC = Type of boundary condition at the wall; 1 for Dirichlet type boundary condition and 2 for Neumann type boundary conditions

SLOPE = $\left(\frac{\partial W}{\partial \eta} \right)_0$

DETA1 = $\Delta \eta_1$

WSTART = Resulting solutions

Subroutine COEFF:

This is the subroutine used to calculate the matrix element A_1 , B_1 , C_1 and D_1 (given by Eqs. 75) used in Subroutine CRANK.

Subroutine DXCTL:

This is the subroutine used to control the step size Δx . The arguments are

DX = Step size Δx

THICKD = Displacement thickness of boundary layer δ^*

CONIL = Control parameter (input value)

DIFF = Maximum value of $|W(i, j+1) - W(i, j)|$

ITER = Iteration number used for previous step size

The step size DX is given by

$$DX = CONTL \cdot |S^*|$$

Subroutine OUTDSK: Subroutine to write out the results on Tape 3.

The subroutine OUTDSK is used for writing the necessary results on the magnetic tape under the output restart file name. These results are needed for the calculation starting at x greater than zero.

A.3 Input and Output

The input data for BLEIG is a description of boundary layer characters, freestream conditions, physical parameters and parameters of boundary layer structure. Where possible, 'free format' input has been used to simplify the use of default values.

The following cards are needed for input data (using CGS units):

- (1) ITYPE, ICASE, IBC, IPRMX, IPRNTY, IFILE
- (2) N, DETAL, XREAL, DX, XMAX, K, CN, TW, EPS, CONTL, ZW
- (3) MREAD — NUMBER OF POINT FREESTREAM CONDITIONS READ
- (4) XDIS(MREAD), EDALP(MREAD), EDU(MREAD), EDTE(MREAD), EDTA(MREAD), EDP(MREAD)
- (5) FIN, FOUT — READ IN AND READ OUT RESTART FILE NAMES
- (6) IGAS — IF IGAS EQUALS TO ZERO, THEN DEFAULTED VALUES ARE USED. IF IGAS IS NOT EQUAL TO ZERO, THEN READ THE FOLLOWING DATA
- (7) MA, R, TION, TEXTC, SAA, SAE, TACRI, TECRI
- (8) QAAC, QAIC, CC1, CC2, CC3, CC4, DD1, DD2, DD3, DD4, TEEA
- (9) EE1, EE2, EE3
- (10) HVC, ZEFF

For example, the following six data cards are used for a nonequilibrium flat-plate boundary with $M_s = 16.6$, $p_o = 4.81$ torr and $T_o = 296$ K:

- (1) 1, 1, 1, 5, 1, 200
- (2) 70, 0.035, 0, 1.E-6, 14, 1.05, 0.75, 296, 1.0E-4, 0.1, 1.E-5
- (3) 1
- (4) 14, 0.021, 4.86E5, 1.049E4, 1.049E4, 0.27E7
- (5) WSL.RST
- (6) 0

The following outputs are given in the present program:

- (1) State of the boundary layer flow.
- (2) Numerical parameters.
- (3) Input freestream conditions.
- (4) Read in and write out restart file names.
- (5) Physical parameters of gas particles.
- (6) If XREAL in input data is zero, then the initial GUESS value obtained from SETUP and Y(1) to Y(9) obtained from BEGIN are given.
- (7) XREAL, XI, J, ITER, DX, UED, TAED, TEEP, ALPED and PED
- (8) I, ETAY, Y(mm), WF, W2, WTA, WTE, CR, CRPR, CRSC, CRPKE, RHO and NE

Flow Chart of Main Calculation Loop

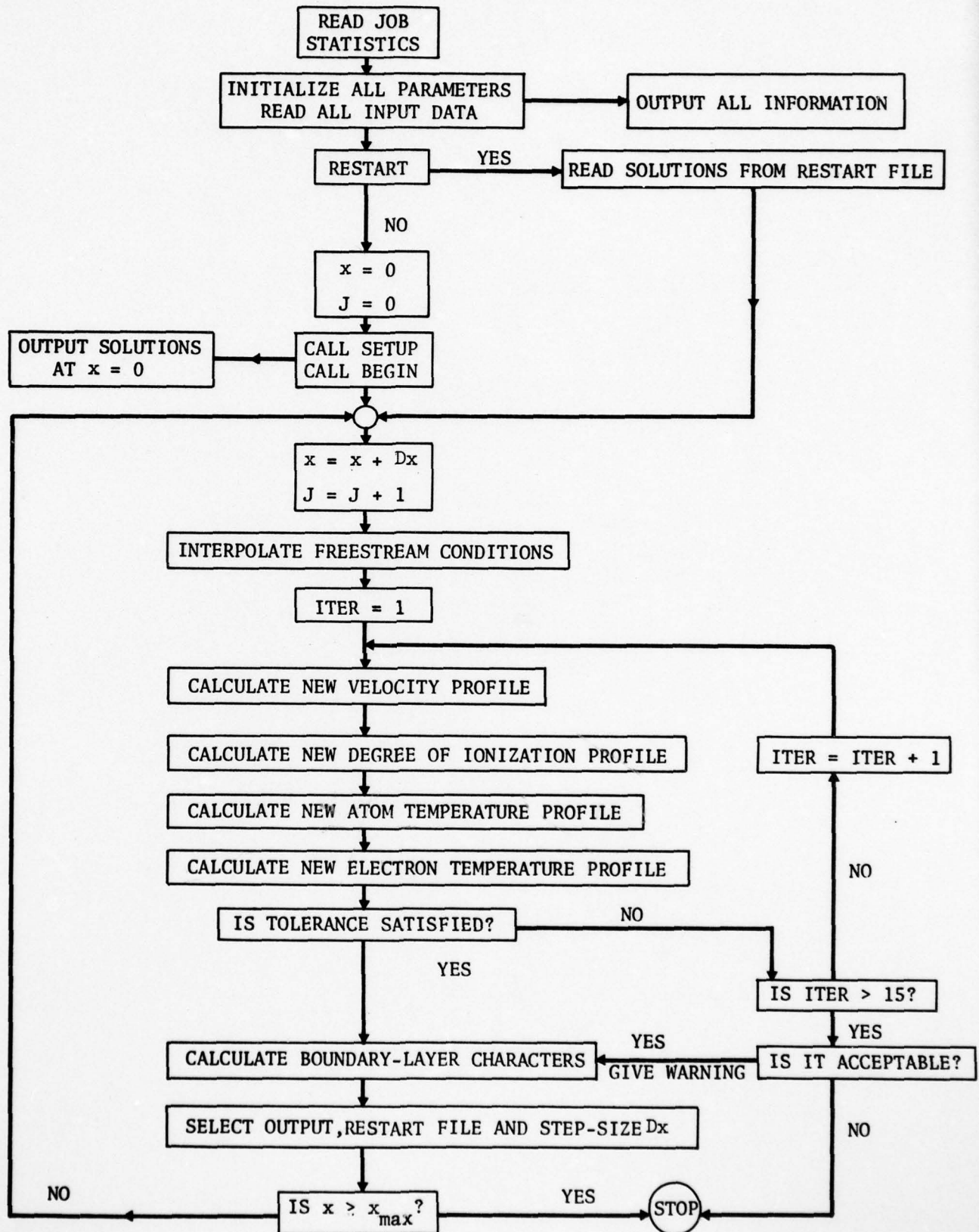


FIG. A.1 FLOW CHART OF THE PROGRAM BLEIG.

APPENDIX B

THERMODYNAMIC QUANTITIES

The definitions and the equations for thermodynamic quantities of a two-temperature ionizing monatomic gas will be summarized. The detailed formulations of the thermodynamic equations can be found in the text books and in the literature.

In this study, we are dealing with a mixture of atoms (a), ions (i) and electrons (e). Atoms and ions have the same temperature T_a and electrons have a temperature T_e . For each species j we have

$$p_j = n_j k_B T_j \quad (B1)$$

$$h_j = \int_0^{T_j} C_{pj} dT_j + h_j^0 \quad (B2)$$

where p_j is the pressure of j species, n_j is the number density of j species, k_B is the Boltzmann constant, h_j is the enthalpy per unit mass of j species, C_{pj} is the specific heat at constant pressure per unit mass of species j and h_j^0 is the chemical enthalpy per unit mass of species j .

The total pressure of the mixture is defined by Dalton's law as

$$p = \sum_j p_j \quad (B3)$$

and the density of the mixture ρ is given by

$$\rho = \sum_j \rho_j \quad (B4)$$

where $\rho_j = m_j n_j$, m_j is the mass of the species j . Since the mass of an electron is negligibly small compared with the mass of an atom, ρ is written as

$$\rho = m_a (n_a + n_e) \quad (B5)$$

where $n_i = n_e$ for singly ionized gas.

The mass fraction of ions, α , which is also called the degree of ionization, is given by

$$\alpha = \frac{\rho_i}{\rho} = \frac{n_e}{n_a + n_e} \quad (B6)$$

The mass fraction of electrons is given by

$$\frac{\rho_e}{\rho} = \frac{m_e}{m_a} \alpha \quad (\text{B7})$$

and the mass fraction of atoms is

$$\frac{\rho_a}{\rho} = 1 - \alpha \quad (\text{B8})$$

The total number density of the plasma is

$$n = \sum_j n_j = n_a + 2n_e \quad (\text{B9})$$

The relations between n_a , n_e and α are given by

$$n_a = \rho(1 - \alpha)/m_a \quad (\text{B10})$$

$$n_e = \rho\alpha/m_a \quad (\text{B11})$$

Therefore, n can be written as

$$n = \rho(1 + \alpha)/m_a \quad (\text{B12})$$

The total pressure p of the plasma becomes

$$p = (n_a + n_e)k_B T_a + n_e k_B T_e \quad (\text{B13})$$

$$= \rho R(T_a + \alpha T_e)$$

where R is the gas constant referred to the atomic gas and defined by $R = k_B/m_a$.

Let N_j be the number of j -particles in the volume V and F_j be the Helmholtz free energy function of one particle of the species j , then the Helmholtz free energy F of the mixture is given by

$$F = \sum_j N_j F_j \quad (\text{B14})$$

AD-A071 950

TORONTO UNIV DOWNSVIEW (ONTARIO) INST FOR AEROSPACE --ETC F/G 20/9
FINITE-DIFFERENCE SOLUTIONS FOR NONEQUILIBRIUM LAMINAR BOUNDARY--ETC(U)
MAY 79 W S LIU AFOSR-77-3303

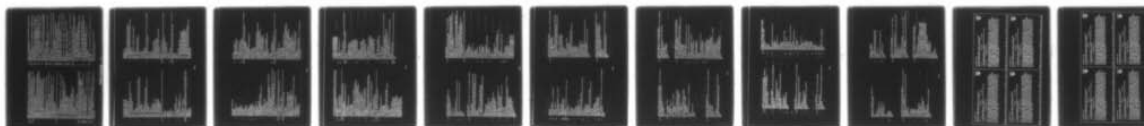
UNCLASSIFIED

UTIAS-226

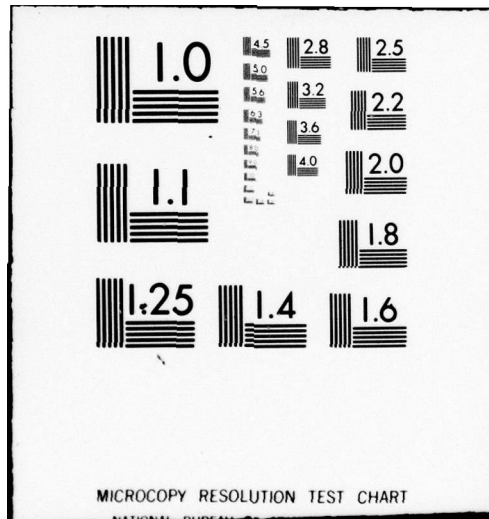
AFOSR-TR-79-0884

NL

2 OF 2
ADA
071950



END
DATE
FILMED
8-79
DDC



where $N_j = n_j V$ and F_j is given by

$$F_j = -k_B T_j [\log g_j^t - \log N_j + \log g_j^i + 1] \quad (B15)$$

g_j^t and g_j^i are the partition functions associated with the translational and internal degree of freedom, respectively.

The entropy S is defined by

$$S = \sum_j N_j S_j \quad (B16)$$

where $S_j = -(\partial F_j / \partial T_j)_V$.

The internal energy E is defined by

$$E = F + TS = \sum_j N_j E_j \quad (B17)$$

where

$$E_j = -T_j^2 \frac{\partial}{\partial T_j} \left(\frac{F_j}{T_j} \right)_V$$

The enthalpy \bar{H} is defined by

$$\bar{H} = \sum_j N_j \bar{H}_j \quad (B18)$$

where

$$\bar{H}_j = E_j + p_j \frac{V}{N_j}$$

Finally, the Gibb's free energy of the plasma G is given by

$$G = \sum_j N_j G_j \quad (B19)$$

where

$$G_j = \bar{H}_j - TS_j$$

According to the above relationships, the specific properties, i.e., the properties per unit mass of an ideal ionizing monatomic gas can be derived from the partition functions of each species involved. The partition function

associated with the translational mode is given by

$$g_j^t = \frac{(2\pi m_j kT_j)^{3/2}}{h^3} V g_{0j} e^{-\epsilon_{0j}/kT_j} \quad (B20)$$

where ϵ_{0j} is the excess energy of the ground states of the j-species above the reference (ground) energy level, g_{0j} is the probability or the statistical weight of the ground energy level ϵ_{0j} and h is the Planck constant.

The internal mode of electronic excitation is always assumed to be at its ground state. The internal partition function for electronic excitation is given by

$$g_j^i = \sum_n g_n e^{-\epsilon_n/kT_j} \quad (B21)$$

where ϵ_n is the energy of the n-th state of the particular species above its ground state and g_n is the statistical weight of state n.

Using Eqs. (B20) and (B21), the specific internal energy e ($e = E/\rho V$) and the specific enthalpy h ($h = \bar{H}/\rho V$) of the mixture can be derived as follows:

$$e = \frac{3}{2} R(T_a + \alpha T_e) + \alpha RT_I \quad (B22)$$

$$h = e + \frac{p}{\rho} = \frac{5}{2} R(T_a + \alpha T_e) + \alpha RT_I \quad (B23)$$

The component specific heats C_{pj} , and the frozen specific heat of the mixture C_{pf} at constant pressure are defined by

$$C_{pj} = \left(\frac{\partial h_j}{\partial T_j} \right)_p \quad (B24)$$

$$C_{pf} = \sum_j \frac{\rho_j}{\rho} C_{pj}$$

The specific heats are all $5k_B/2$ per particle. Therefore, C_{pf} is given by

$$C_{pf} = \frac{5}{2} R(1 + \alpha) \quad (B25)$$

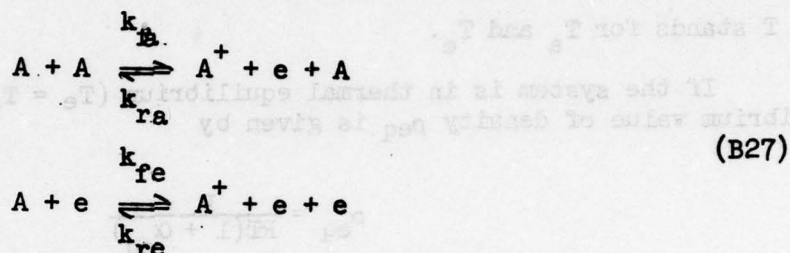
Similarly, the specific heats C_{vj} and the frozen specific heat of the mixture C_{vf} at constant volume are defined by

$$C_{vj} = \left(\frac{\partial e_j}{\partial T_j} \right)_v \quad (B26)$$

Contd...

$$C_{vf} = \sum_j \frac{\rho_j}{\rho} C_{vj} = \frac{3}{2} R(1 + \alpha) \quad (B26)$$

When the mixture is in chemical equilibrium, Gibb's free energy has its minimum for all possible changes in composition of a system at a given pressure and a given temperature. The equilibrium equation for the degree of ionization α_{eq} can be obtained by using this condition. A detailed derivation of $\alpha_{eq} = \alpha_{eq}(p, T)$ based on this concept was given by Glass and Takano. Another derivation of the Saha equation, or equilibrium equation, is described as follows: Let the overall reaction paths be represented by



where A denotes atoms.

Production rates of electron number density associated with Eq. (B27) can be expressed as follows:

$$(\dot{n}_e)_a = k_{fa} n_a^2 - k_{ra} n_a n_e^2 \quad (B28)$$

$$(\dot{n}_e)_e = k_{fe} n_a n_e - k_{re} n_e^3 \quad (B29)$$

where k_f and k_r are forward and reverse rate coefficients, respectively.

In an equilibrium state, the forward and reverse reactions are balanced in the process. Therefore,

$$\frac{k_{fa}(T_a)}{k_{ra}(T_a)} = K_{eq}(T_a) = \frac{n_{e,eq}^2(T_a)}{n_{a,eq}(T_a)} \quad (B30)$$

$$\frac{k_{fe}(T)}{k_{re}(T)} = K_{eq}(T_e) = \frac{n_{e,eq}^2(T_e)}{n_{a,eq}(T_e)} \quad (B31)$$

where $K_{eq}(T)$ is the equilibrium constant, which is given by

$$K_{eq}(T) = \frac{2g_I}{g_a} \left(\frac{2 m_e k_B T}{h^2} \right)^{3/2} \exp(-T_I/T) \quad (B32)$$

and g_a , g_I are the electronic excitation partition functions of atom A and ion A^+ particles.

Using Eqs. (B10) and (B11), the equilibrium value of degree of ionization, α_{eq} , is obtained from Eqs. (B30) and (B31) as follows:

$$\frac{\alpha_{eq}^2}{1 - \alpha_{eq}} = \frac{m_a}{\rho_{eq}} K_{eq}(T) \quad (B33)$$

where T stands for T_a and T_e .

If the system is in thermal equilibrium ($T_e = T_a = T$), then the equilibrium value of density ρ_{eq} is given by

$$\rho_{eq} = \frac{p}{RT(1 + \alpha_{eq})} \quad (B34)$$

Introducing a characteristic density for ionization, ρ_I , the equilibrium equation for α becomes

$$\alpha_{eq}(p, T) = \left[\frac{p}{\rho_I RT_I} \left(\frac{T_I}{T} \right)^{5/2} e^{T_I/T} + 1 \right]^{-1/2} \quad (B35)$$

where

$$\rho_I = 2 \left(\frac{m_e}{m_a} \right)^{3/2} \frac{g_I}{g_a} \frac{(2\pi k_B T_I)^{3/2}}{h^3} m_a^{5/2} \quad (B36)$$

For argon, $\rho_I = 150.27 \text{ g/cm}^3$.

Equation (B35) is known as Saha's equation. Given pressure p and temperature T, the degree of ionization α is calculated from Eq. (B35) if the flow is in chemical equilibrium.

Production rates of electron number density, $(\dot{n}_e)_a$ and $(\dot{n}_e)_e$, given by Eqs. (B28) and (B29) become

$$(\dot{n}_e)_a = k_{ra}(T_a) n_a [K_{eq}(T_a) n_a - n_e^2] \quad (B37)$$

$$(\dot{n}_e)_e = k_{re}(T_e) n_e [K_{eq}(T_e) n_a - n_e^2] \quad (B38)$$

The equilibrium degree of ionization α_{eq} is obtained by setting the square brackets in Eqs. (B37) and (B38) equal to zero and solving for α . Thus the equilibrium degree of ionization is a function of the local temperature and pressure. This does not imply that $(\dot{n}_e)_a = 0$ and $(\dot{n}_e)_e = 0$ or even that \dot{n}_e approaches zero at equilibrium, since to achieve equilibrium the reverse reaction rate coefficient k_{ra} and k_{re} must become infinite. As k_{ra} and k_{re}

approach infinity, equilibrium is attained. The case $k_{ra} = 0$ and $k_{re} = 0$ corresponds to frozen flow. The actual value of $(\dot{n}_e)_{eq}$ as a function of the boundary layer coordinate η cannot be calculated from the chemical kinetics but must be determined by solving the boundary layer equations.

In the inviscid flow region if the flow is frozen then α is constant since the ambipolar diffusion velocity of ions and electrons is assumed very small and can be neglected. However, if the flow is frozen then α is not constant in the boundary layer flow due to the diffusion process of ions and electrons.

The following mathematical expressions for the flow conditions are given:

Equilibrium:

$$(\dot{n}_e)_{eq} = \lim_{\substack{k_{ra} \rightarrow \infty \\ k_{re} \rightarrow \infty \\ \alpha \rightarrow \alpha_{eq}}} [(\dot{n}_e)_a + (\dot{n}_e)_e]$$

Frozen:

$$(\dot{n}_e)_{frozen} = 0$$

Nonequilibrium:

$$\dot{n}_e \neq 0$$

APPENDIX C

EXPRESSIONS OF FUNCTIONS $x_j^{(1)}$

With $i = 1$, $W^{(1)} = F$:

$$x_1 = C$$

$$x_2 = C_\eta + f + 2\xi f_\xi$$

$$x_3 = -\beta_f F$$

$$x_4 = 2\xi F$$

$$x_5 = -\beta_f \left(\frac{\rho_\delta}{\rho} \right)$$

With $i = 2$, $W^{(2)} = z$:

$$x_1 = \frac{C}{Sc}$$

$$x_2 = \left(\frac{C}{Sc} \right)_\eta + f + 2\xi f_\xi$$

$$x_3 = -\beta_z F + \tau_a \frac{\dot{n}_e}{n_e}$$

$$x_4 = 2\xi F$$

$$x_5 = 0$$

With $i = 3$, $W^{(3)} = \theta$:

$$x_1 = \frac{C}{Pr}$$

$$x_2 = \left(\frac{C}{Pr} \right)_\eta + f + 2\xi f_\xi$$

$$x_3 = -F \left(\beta_{T_a} + \frac{\beta_f \tau_f}{1 + \alpha_{\delta\tau}} \right) - \frac{3}{5} \tau_u \alpha V_{eai}$$

$$x_4 = 2\xi F$$

$$x_5 = -\tau_f C F \eta^2 + \tau_u Q_R / (\rho C_p T_{a\delta}) + \alpha \frac{T_e}{T_{a\delta}} \left[-\frac{3}{5} \tau_u V_{eai} + \tau_I \frac{(\dot{n}_e)_a}{n_e T_e} \right] \\ + \beta_f \tau_f F z \theta \frac{\alpha_\delta \tau}{1 + \alpha_\delta \tau}$$

With $i = 4$, $W^{(4)} = \theta$:

$$x_1 = \frac{C}{Pr_e}$$

$$x_2 = \left(\frac{C}{Pr_e} \right)_\eta + \left(\frac{C}{Sc} \right) \alpha_\delta z_\eta + \alpha(f + 2\xi f_\xi)$$

$$x_3 = -\alpha \left[\beta_{T_e} F + \frac{3}{5} \tau_u V_{eai} + \tau_u \frac{\dot{n}_e}{n_e} \right]$$

$$x_4 = 2\xi F \alpha$$

$$x_5 = \alpha \frac{T_a}{T_{e\delta}} \left[-\frac{3}{5} \tau_u V_{eai} + \tau_I \frac{(\dot{n}_e)_e}{n_e T_a} \right]$$

APPENDIX D

EFFECTS OF CHEMICAL REACTIONS ON BOUNDARY LAYER

The large change of the chemical reaction rates with temperatures has an important effect on the boundary layer structure for the case of large degree of ionization. Two important effects, mathematical and physical effects, of chemical reactions on the boundary layer structure are described as follows:

I. The equation for conservation of electrons is given by Eq. (21). This nonlinear equation is coupled to the equations of conservation of plasma and electron energies, momentum and mass of the remaining species through the functions C , Sc , f , f' and \dot{n}_e . Without any loss in the general character of the equation for electron species, we assume a local similarity equation with $C/Sc = 1$, $f = 1$ and $f' = 0$:

$$z'' + z' + K' \dot{n}_e = 0 \quad (D1)$$

where

$$K' = \frac{2\xi}{\rho_0 \mu_0 u_0^2} \frac{m_a}{\rho \alpha_0}$$

In order to illustrate the nature of the problem involved, the following linearized and simplified version of Eq. (D1) is considered:

$$z'' + z' - K z = 0 \quad (D2)$$

where K is a constant which includes the chemical reaction term.

This simplified and linearized equation, Eq. (D2), contains all the difficulties associated with the integration scheme used in numerical solution of the boundary layer equations. The general solution of Eq. (D2) is

$$z = C_1 e^{-\frac{1 + \sqrt{1 + 4K}}{2} \eta} + C_2 e^{\frac{\sqrt{1 + 4K} - 1}{2} \eta} \quad (D3)$$

where $K \geq 0$. The constants C_1 and C_2 can be determined from the two-point boundary values of $z = z_w$ at $\eta = 0$ and $z = 1$ at $\eta \rightarrow \infty$ or $z' = z'_w$ at $\eta = 0$ and $z = 1$ at $\eta \rightarrow \infty$.

It is seen from Eq. (D3) that if the initial guess for z'_w is not correct, then the second term in Eq. (D3) will dominate at large values of η so that $z \rightarrow \infty$ at $\eta \rightarrow \infty$. Only if $K = 0$, z at $\eta \rightarrow \infty$ will achieve a finite value that can be used to refine the guess for z'_w .

Blottner (Ref. 17) has used a finite-difference method to solve Eq. (21). However, he did not linearize the source term \dot{n}_e as we have done in Chapter 5. The solutions given by Blottner (Ref. 17) appear to be cases for which $K \ll 1$. The method used for linearization in Chapter 5 is similar to the method of quasilinearization used by Fay and Kaye (Ref. 5) in the solution of similar nonequilibrium boundary layers.

For the frozen flow ($\dot{n}_e = 0$), Eq. C1 becomes:

$$z'' + z' = 0 \quad (D4)$$

Solution of Eq. D4 is given by

$$z = C_1 e^{-\eta} + C_2$$

Therefore, no mathematical difficulty associates with the frozen flow.

2. The dependence of the reaction rate coefficients on the temperatures are described in Section 3.3. For low temperature (below 1000 K), $k_{fa}(T_a)$ and $k_{fe}(T_e)$ are very small compared with $k_{ra}(T_a)$ and $k_{re}(T_e)$, respectively, and the forward reaction rates can be neglected. With temperatures above 10,000 K, forward reaction rates become significant. However, these forward reaction rates are still very small compared with the reverse recombination rates. The following relations are satisfied at temperature about 10,000 K:

$$k_{re} n_e^3 \gg k_{fe} n_a n_e$$

$$k_{ra} n_a n_e^2 \gg k_{fa} n_a^2$$

$$k_{re} n_e^3 > k_{ra} n_a n_e^2$$

Therefore the reverse recombination rate due to electron-ion-electron collisions is the important process in the boundary layer structure.

However, in the region where atom temperature is about 25,000 K (for example, in the region near the shock front where atom temperature is much greater than electron temperature), the following relations hold:

$$k_{fa} n_a^2 \gg k_{ra} n_a n_e^2$$

$$k_{fe} n_a n_e \gg k_{re} n_e^3$$

$$k_{fa} n_a^2 > k_{fe} n_a n_e$$

The forward reaction rates become the dominant process in the flow.

For cases analyzed in Chapters 6 and 7 the degree of ionization for frozen flow is larger than that for nonequilibrium flow at fixed x and η values. As x increases, degree of ionization increases for frozen flow and decreases for nonequilibrium flow at fixed η value.

APPENDIX E

EFFECTS OF BOUNDARY LAYER ON SHOCK WAVE STRUCTURE

The analyses in Refs. 24 and 25 on shock-wave structure were made with the assumption that flow was one-dimensional. The role of the boundary-layer growth on shock-wave structure was not considered. Mirels (Ref. 54) has shown that the flow between the shock and contact surface in an actual shock tube is nonuniform due to the side-wall boundary layer. Recently, Enomoto (Ref. 55) has studied the effects of the boundary-layer growth on the ionization relaxation in argon, based on Mirel's boundary-layer theory. Enomoto (Ref. 55) showed that the temperature, density and pressure increase in value with distance from the shock front due to boundary layer growth, and the ionization relaxation time is significantly shortened by introducing side-wall boundary-layer effects.

The present section only discusses the governing equations which are applicable to quasi-one-dimensional nonequilibrium flow behind a shock wave. Details of the effects of the side-wall boundary layer on the shock-wave structure is under study and will be presented in a forthcoming UTIAS Report.

The specification of a problem in the field of gasdynamics requires the flow equations (mass, momentum and energy) with supplementary information on the equation of state of the gas. The governing equations for flow behind the shock wave are written in shock-fixed coordinates as

$$\frac{1}{A} \frac{d}{dx} \langle A \rho u \rangle = 0 \quad (E1)$$

$$\frac{1}{A} \frac{d}{dx} \langle A \rho u^2 \rangle = - \frac{dp}{dx} \quad (E2)$$

$$\frac{1}{A} \frac{d}{dx} \langle A \rho u H \rangle = -Q_R \quad (E3)$$

$$\frac{1}{A} \frac{d}{dx} \langle A \rho u \alpha \rangle = m_a \dot{n}_e \quad (E4)$$

$$\frac{1}{A} \frac{d}{dx} \langle A \rho u h_e \rangle = \left\langle u \frac{dp_e}{dx} \right\rangle + \langle Q_{el} + Q_{inel} \rangle \quad (E5)$$

where A is the effective cross-sectional tube area, and $\langle f \rangle = \int f dA/A$.

By using the equation of state, $p = \rho R(T_a + \alpha T_e)$, the governing equations can be approximated as (Enomoto, Ref. 55)

$$\frac{d\alpha}{dx} = \frac{m_a \dot{n}_e}{\rho u} \quad (E6)$$

$$\frac{du}{dx} = \frac{5u}{3\rho u^2 - 5p} \left[\frac{p}{A} \frac{dA}{dx} + \frac{2}{5} \rho R T_I \frac{d\alpha}{dx} + \rho R Q_R \right] \quad (E7)$$

$$\frac{dT_e}{dx} = \frac{2}{3} \frac{Q_{el} + Q_{inel}}{n_e u k_B} - \frac{2T_e}{3u} \frac{du}{dx} \quad (E8)$$

$$\frac{dT_a}{dx} = -\frac{u}{C_p} \frac{du}{dx} - \alpha \frac{dT_e}{dx} - \left(T_e + \frac{2}{5} T_I \right) \frac{d\alpha}{dx} - Q_R \quad (E9)$$

$$\frac{dp}{dx} = -\rho u \frac{du}{dx} \quad (E10)$$

The above five equations, Eqs. (E6 - E10), are required for the five dependent variables: α , u , T_a , T_e and γ . The initial conditions at $x = 0$, immediately behind the frozen shock, are

$$\alpha \approx 0$$

$$u = \frac{u_o}{4} \left[1 + \frac{3}{M_s^2} \right]$$

$$T_a = T_o \left[\frac{5}{16} \left(M_s^2 - \frac{3}{5M_s^2} \right) + \frac{7}{8} \right]$$

$$T_e \approx T_a \text{ or } T_o$$

$$p = \frac{\rho_o u_o}{u} R T_a$$

where the subscript o denotes quantities evaluated in the unionized ($\alpha = 0$) upstream gas. The length required to reach quasi-equilibrium is nearly identical for both initial values of T_e .

The values \bar{A} and $d\bar{A}/dx$ can be obtained from the solutions of side-wall boundary layer (Chapter 7).

It has been shown by Glass and Liu (Ref. 24) that the radiation-energy loss has no effect on the relaxation length. The condition that the side-wall boundary layer effects on shock structure can be neglected is only good when

$$\frac{dA}{dx} \ll \frac{2\rho R T_I A}{5p} \frac{d\alpha}{dx} \quad (E11)$$

It can be shown that the side-wall boundary-layer effects in the UTIAS 10 cm x 18 cm Hypervelocity Shock Tube at shock Mach numbers of $M_s \approx 13 \sim 16$ is not small since Eq. (E11) is not satisfied.

A detailed study on the mutual interactions between shock structure and shock-tube sidewall boundary layer flows based on the correct set of effective quasi-one-dimensional flow equations will be reported by K. Takayama and W. S. Liu.


```

C-----
C      PROGRAM HLEIG(INPUT,OUTPUT,TAPE=INPUT,TAPE=OUTPUT,TAPE1,TAPE3)
C      SOLVE BOUNDARY LAYER EQUATIONS OF IONIZING GAS BY MEANS OF FINITE
C      DIFFERENCE SCHEME WITH MODIFIED CRANK-NICOLSON METHOD.
C-----
C      DIMENSION EDU(100),EDTA(100),FDTE(100),EDALP(100),EDP(100)
C      DIMENSION X0IS(100),DENNE(100)
C      DIMENSION WZ(100),WZ(100),WTA(100),WTE(100),SF(100),SFV(100)
C      DIMENSION WFP(100),WZP(100),WTA(100),WTE(100),WTEP(100),GUESS(4),WDRK(100)
C      DIMENSION F(100),Z(100),WTEYA(100),WTEP(100),ETAY(100),YREAL(100)
C      DIMENSION CR(100),CRPR(100),CRSC(100),CRPRE(100),RHO(100)
C      DIMENSION CRP(100),CRPRP(100),CRSCP(100),CRPREP(100)
C      DIMENSION OLDWF(100),OLDWZ(100),OLDWTA(100),OLDWTE(100),OLDWTF(100)
C      REAL LAND,LANDE,MU,K,K1,K2,KSG,NA,NE,MA,MUM,NEDOTA,NEDOTE
C      INTEGER IN,OUT
C      COMMON/ACONVUED,PED,TAED,TEED,ALPED,TM,ALPM,IUM,GUESS,ROL,MUE
C      COMMON/DESK/WZ,WZ,WTA,WTE
C      COMMON/SOLVE/F2,THETA,THETF,ETAY,CR,CRPR,CRSC,CRPRE,MUM,DENNE,RHO
C      COMMON/ENDIF/K,CN,DETAI,N,DEX,TBC
C      COMMON/BLK1/A(100),C(100),C(100),D(100),D(100),D(100),D(100),D(100),X(5)
C      COMMON/GAS1/MA,M,TION,TEXC,SAA,SAF,TACRI,TECRI
C      COMMON/GAS2/QAAC,QATC,CC1,CC2,CC3,CC4,DD1,DD2,DD3,DD4,TEEA
C      COMMON/GAS3/EE1,EE2,EE3
C      COMMON/GAS4/HVC,ZEFF
C-----
C      DATA IKILL/0/
C      DATA IN,OUT/1,3/
C      DATA N,DX,MXAX,CN,EPB,DETAI,K/70,1.E-6,10,1,1.E-5,0.035,1.05,/
C      DATA ITYPE,TBC,ICASE/1,1,1/
C      DATA UM,TM,ALPM,CONFL,YHM,THICKD/0,300,1.E-10,0.5,0.0,0./
C      DATA J,REAL,XI,NEDOTA,NEDOTE,ITER/0,0,0,0,0,0./
C      DATA NPAGE,NFILE,IPRNTX,IPRNTY,IFILE/0,0,1,1,1/
C      DATA MA,R/6.03309E-23,2.08129E6/
C      DATA TION,TEXC/183100.,135300./
C      DATA SAA,SAE/1.0E-19,4.9E-18/
C      DATA TACRI,TECRI/3100.,3100./
C      DATA QAAC,QATC/1.704E-19,2.454E-14/
C      DATA CC1,CC2,CC3,CC4/0,713,-4,5E-4,1.5E-7,0./
C      DATA DD1,DD2,DD3,DD4/0,0.408,3.96E-4,0,0,0./
C      DATA TEEA/3100./
C      DATA EE1,EE2,EE3/4,0.2,0.2062./
C      DATA HVC,ZEFF/4.5602E-12,1.2845/
C-----
C301      FORMAT(1X,"FINITE DIFFERENCE SOLUTION OF THE COMPRESSIBLE TWO-TEMP
C302      1ERATURE BOUNDARY-LAYER EQUATIONS FOR IONIZING ARGON",//)
C303      FORMAT(1X,"FLAT-PLATE BOUNDARY-LAYER FLOW IS STUDIED")
C304      FORMAT(1X,"SHOCK-TUBE SIDE-WALL BOUNDARY-LAYER FLOW IS STUDIED")
C305      FORMAT(1X,"NONEQUILIBRIUM BOUNDARY LAYER")
C306      FORMAT(1X,"FROZEN BOUNDARY LAYER")
C307      FORMAT(1X,"USING SHEATH CONDITION FOR ELECTRON TEMPERATURE AT THE
C308      1 WALL")
C309      FORMAT(1X,"USING SHEATH CONDITION FOR ELECTRON TEMPERATURE AND DEG
C310      1 REE OF IONIZATION AT THE WALL")
C311      FORMAT(1X,"INPUT FREESTREAM CONDITIONS ARE",//)
C312      FORMAT(1X,"NUMERICAL PARAMETERS: N=",X1,DETAI="P7.4",DX
C313      1="F9.0E",CM,XMAX="F6.2",CH,K="F7.5",CN="F5.2",TM="
C314      2="F6.2",K=")

```

```

3311 FORMAT(' XDLS(CH)' ,2X,'EDALP' ,5X,'EDU(CH/SEC)' ,1X,'EDTE(K)' ,2X,  

3312 ='EDYA(K)' ,3X,'EDP(DYNES)' ,//  

3313 FORMAT('/',) GUESS(1)='F9.6', GUESS(2)='F9.6', GUESS(3)='F9.6',  

3314 GUESS(4)='F9.6',//  

3315 FORMAT(3X,'EPS =' ,G10.3, ' , CONTL =' ,F6.3, ' , ZH =' ,G10.3,//)  

3316 FORMAT(1X,'UED =' ,G11.4, ' , CH/JS, TAFD =' ,G11.4, ' , , TEED =' ,G11.4, ' ,  

3317 1 'K, ALPED =' ,G11.4, ' , PED =' ,G11.4, ' , DYNES, '//  

3318 FORMAT(' *** WARNING(12), *** , ITERATION NUMBER IS EXCEEDED 15 AT  

3319 1X =' ,F9.5, ' , CM WITH STEP SIZE DX =' ,G12.4, ' , CM *** ,//  

3320 FORMAT(' XREAL =' ,F9.6, ' , CM , XI =' ,F9.6, ' , J =' ,14, ' , ITER =' ,  

3321 113, ' , DX =' ,F9.6, ' , CM ,//)  

3322 FORMAT(1X, 'I' ,4X,'RETA(1)' ,5X,'V(MH)' ,4X,'WF' ,10X,'WZ' ,8X,'WTA',  

3323 17X,'WTE' ,6X,'CR' ,5X,'CR/PR' ,6X,'CR/SC' ,5X,'CR/PRE' ,2X,'RHO(G/CM3)' ,  

3324 2,2X,'NEI(CM3)' ,//  

3325 FORMAT(1X,13,10F10.5,2G10.3)  

3326 FORMAT('/',) THICKD =' ,G11.3, ' , CM, DMFDY =' ,G10.4, ' , DMZDY =' ,G10.4, ' ,  

3327 1 ' , DNTDY =' ,G10.4, ' , DNTEDY =' ,G10.4,//)  

3328 FORMAT(11)  

3329 FORMAT(1X,'OHMHMHMH....I AM DYING! PLEASE DECREASE K OR N TO A RE  

3330 1ASONABLE VALUE')  

3331 FORMAT('/',)1X,'THE FOLLOWING PHYSICAL PARAMETERS OF GAS PARTICLES A  

3332 1RE USED IN THE CALCULATION,/' )  

3333 FORMAT(3X,'WA =' ,G12.5, ' , GRAM, R =' ,G12.5, ' , CM2/SEC2/K')  

3334 FORMAT(3X,'TATION =' ,F9.1, ' , K, TEXT =' ,F9.1, ' , M')  

3335 FORMAT(3X,'SAA =' ,G12.4, ' , CM2/FEV, SAE =' ,G12.4, ' , CM2/FEV')  

3336 FORMAT(3X,'TACRI =' ,F7.1, ' , K, TECTR =' ,F7.1, ' , K, TEFA =' ,F7.1, ' , K')  

3337 FORMAT(3X,'OACAC =' ,G12.4, ' , OACIC =' ,G12.4, ' ,  

3338 1G12.4)  

3339 FORMAT(3X,'OACI =' ,G12.4, ' , CC2 =' ,G12.4, ' , CC3 =' ,G12.4, ' , CC4 =' ,  

3340 1G12.4)  

3341 FORMAT(3X,'EE1 =' ,G12.4, ' , EE2 =' ,G12.4, ' , EE3 =' ,G12.4, ' ,  

3342 1G12.4)  

3343 FORMAT(3X,'HVC =' ,G12.5, ' , ZEFF =' ,F8.4,//)  

3344 FORMAT(2A10)  

3345 FORMAT('/',)1X,'READ IN RESTART FILE =' ,A10, ' , READ OUT RESTART FILE  

3346 1 =' ,A10,//)  

3347 FORMAT('/',)1X,'DISTANCE OF RESTART JS' ,G13.6, ' , CM')  

3348 C-----  

3349 C THE FOLLOWING CARDS ARE NEEDED FOR INPUT DATA(USING CGS UNITS)  

3350 C (1) ITYPE, ICASE, IBC, IPRNTX, IPRNTY, IFILE  

3351 C (2) N, DETAL, XREAL, DX, XMAX, XCN, TW, EPS, CONTL, ZH  

3352 C (3) MREAD, NUMBER OF POINT FREESTREAM CONDITIONS HEAD  

3353 C (4) XDLS(MREAD), EDALP(MREAD), FDI(MREAD), EDTE(MHEAD), EDYA(MHEAD),  

3354 C FDP(MREAD)  

3355 C (5) FIN, FOUT, READ IN AND READ OUT RESTART FILE NAMES  

3356 C (6) IGAS, IF IGAS EQUALS TO ZERO, THEN DEFAULTED VALUES ARE USED  

3357 C IF IGAS IS NOT EQUAL TO ZERO, THEN READ THE FOLLOWING DATA  

3358 C (7) MA, RTION, TEKC, SAA, SAE, YACRI, YACRI  

3359 C (8) OACIC, OACI, CC1, CC2, CC3, CC4, DD1, DD2, DD3, DD4, TEFA  

3360 C (9) EE1, EE2, EE3  

3361 C (10) HVC, ZEFF  

3362 C-----  

3363 PRINT 327  

3364 PRINT 301  

3365 IF (ITYPE.EQ.1) PRINT 302

```

```

IF(I,TYPE,EG,2) PRINT 303
IF(I,CASE,EG,1) PRINT 304
IF(I,CASE,EG,2) PRINT 305
IF(I,BC,EG,1) PRINT 306
IF(I,BC,EG,2) PRINT 307
READ *,N,DETA,XREAL,DX,XMAX,K,CN,TW,EP,CONTL,ZM
PRINT 310,N,DETA1,DX,XMAX,K,CN,TW
PRINT 314,EP,CONTL,ZM
PRINT 311
READ *,MREAD
DO 1 I=1,MREAD
  READ *,XDIS(I),EDALP(I),EDU(I),EDTE(I),EDTA(I),EDP(I)
  PRINT 312,XDIS(I),EDALP(I),EDU(I),EDTE(I),EDTA(I),EDP(I)
  READ 341,FIN,FOUT
  PRINT 342,FIN,FOUT
  READ *,IGAS
  IF(IGAS,EG,0)GO TO 3
  READ *,N,RATION,TEXC,SAA,SAE,TACRI,TECRI
  READ *,GAAC,GAIC,CC1,CC2,CC3,CC4,DD1,DD2,DD3,DD4,TEEA
  READ *,E1,E2,E3
  READ *,HVC,ZEFF
  PRINT 331
  PRINT 332,MA,R
  PRINT 333,TION,TEXC
  PRINT 334,SAA,SAE
  PRINT 335,TACRI,TECRI,TEEA
  PRINT 336,GAAC,GAIC
  PRINT 337,CC1,CC2,CC3,CC4
  PRINT 338,DD1,DD2,DD3,DD4
  PRINT 339,E1,E2,E3
  PRINT 340,HVC,ZEFF
  NIM=N-1
  CP2=5-R
  CN1=1-CN
  K1=1-K
  K2=K2-1
  K3=K3-K
  DKR1=DETA1
  ETAS=0
  DO 2 I=1,N
    I=I+1
    DI(I)=1/(OK=K=I)
    IF(DI(I),LT,1,E=30) PRINT 330
    ETAY(I)=ETA
    ETABETA,DETA1*(K=(I-1))
    D2(I)=2-D1(I)/(DETA1*(K=(I-1)))
    XS=XREAL
    IF(FIN,EG,FOUT)GO TO 10
    IF(FIN,NE,SM)GO TO 10
  C-----CALCULATE FLOW PROFILES BEGINNING AT THE LEADING EDGE(OR AT X80)
  PEDREDP(1)
  TAED=EDTA(1)
  TEED=EDTE(1)
  ALPED=EDALP(1)

```

```

UED=EDU(1)
USSO=5,*RATW/3.
ALPM=2M*ALPED
IF(I,TYPE,EG,2)UM=2,*UED+SORT(4,*UED+UED-3,*USSU)
CALL DENST(PED,TAED,TEED,ALPED,ENA,ENE,ROLE)
CALL TRANSP(TAED,TEED,ENA,ENE,EMU,LAND,LAMDE,DAMG,VEA1)
ROL=MUE*ROLE*EMU
CALL SETUP
PRINT 313,GUESS(1),GUESS(2),GUESS(3),GUESS(4)
CALL BEGIN
PRINT 327
PRINT 321,XREAL,XI,J,ITER,DX
PRINT 316,UED,TAED,TEED,ALPED,PED
PRINT 322
DO 4 I=1,N
  WF(I)=F(I)
  WZ(I)=Z(I)
  WTA(I)=THETA(I)
  WTE(I)=THETE(I)
  PRINT 325,I,ETAY(I),YHM,WF(I),WZ(I),WTA(I),WTE(I),CRPR(I)
  ICPRC(I),CRPRE(I),RHU(I),DENNE(I)
  WF(N)=1.0
  WZ(N)=1.0
  WTA(N)=1.0
  WTE(N)=1.0
  DMFOV=(WF(2)-WF(1))/DETA1
  DMZDV=(WZ(2)-WZ(1))/DETA1
  DMADV=(WTA(2)-WTA(1))/DETA1
  DATEDV=(WTE(2)-WTE(1))/DETA1
  PRINT 326,THICKD,DMFOV,DMZDV,DMADV,DMTEDV
  GAM1=ROL*MUE*EDU(1)
  GO TO 5
C-----START FROM A RESTART FILE
10 READ(IN) J,XREAL,XI,DX,PED,GAM1,(WF(I),WZ(I),WTA(I),WTE(I),CR(I),
  1 CRPR(I),CRSC(I),CRPRE(I),I=1,N)
  IF(EOF(IN),NE,0)GO TO 11
  IF(XREAL,GT,XS)GO TO 11
  GO TO 10
11 CONTINUE
PRINT 350,XREAL
C-----CALCULATE FLOW PROFILES FOR X GREATER THAN ZERO
5 CONTINUE
XIO=XI
PEDO=PED
J=J+1
XREAL=XREAL+DX
IF(XREAL,GT,XMAX)XREAL=XMAX
CALL INTERP(UED,XREAL,MREAD,XDIS,EDTA)
CALL INTERP(TAED,XREAL,MREAD,XDIS,EDTA)
CALL INTERP(TEED,XREAL,MREAD,XDIS,EDTE)
CALL INTERP(ALPED,XREAL,MREAD,XDIS,EDALP)
CALL INTERP(PED,XREAL,MREAD,XDIS,FDP)
CALL DENST(PED,TAED,TEED,ALPED,ENA,ENE,ROLE)
CALL TRANSP(TAED,TEED,ENA,ENE,EMU,LAND,LAMDE,DAMG,VEA1)
ROL=MUE*ROLE*EMU
GAM2=ROL*MUE*UED

```



```

40 CALL COEFF(1,0F,DDF,XP)
   CALL CRANK(1,0,DETA1,N1,MF)
   CALL INTRG(K,DETA1,N,MF,8F)
   DO 42 I=1,N
      F(I)=CM*MF(I)+CN1*WFP(I)
      WORK(I)=(MF(I)-WFP(I))/DEX
   CALL INTRG(K,DETA1,N,WORK,8FX)
42
C-----CALCULATE THE NEW DEGREE OF IONIZATION PROFILE
C-----
   TEMCNHTE(1)=CN1*WTEP(1)
   ZMHCN*WZ(1)+CN1*WZP(1)
   SCWSCR(1)/CRSC(1)
   SLOPE=SCM*SQXUE/MUM*VIED*ZM*SQRT(YEN)
   DO 50 I=2,N1
      OLDNZ(1)=WZ(I)
      ALPH*Z(1)=ALPED
      TASTHETA(1)=TAED
      TETHETE(1)=TEED
      CALL DENSIT(PED,TA,TE,ALPH,NA,NE,ROL)
      IF(1,CASE,EO,1)CALL RATES(TA,TE,NA,NE,NEDOTA,NEDOTE)
      DCS=CRSC(I+1)+K2*CRSC(I)=KSO*CRSC(I+1)
      DCSCP=CRSCP(I+1)+K2*CRSCP(I)=KSO*CRSCP(I+1)
      DCSND(1)=(CN+DCSC*CN1+DCSCP)
      O7*WZP(I+1)+K2*WZP(I)=KSO*WZP(I+1)
      ODZ*WZP(I+1)=K1*WZP(I)+K*WZP(I+1)
      X(1)=CRSC(I)
      X(2)=DCSDN*SF(I)+2.*XE*8FX(I)
      X(3)=OETAZ*F(I)+YAUU*(NEDOTA+NEDOTE)
      X(4)=2.*XE*F(I)
      X(5)=0.0
   XPH=ZP(I)
50
   CALL COEFF(1,0Z,DDZ,XP)
   CALL CRANK(1G,SLOPE,DETA1,N1,WZ)
C-----CALCULATE THE NEW ATOM TEMPERATURE PROFILE
C-----
   DO 60 I=2,N1
      OLDTA(I)=WTA(I)
      Z(1)=CM*WZ(1)+CN1*WZP(1)
      ALPH*Z(1)=ALPED
      TASTHETA(1)=TAED
      TETHETE(1)=TEED
      CALL DENSIT(PED,TA,TE,ALPH,NA,NE,ROL)
      CALL TRANS(T,TE,NA,NE,MU,LAMB,LAMBE,DAMB,VEAL)
      IF(1,CASE,EO,1)CALL RATES(TA,TE,NA,NE,NEDOTA,NEDOTE)
      DCP=CRCP(I+1)+K2*CRCP(I)=KSO*CRCP(I+1)
      DCPBP=CRBP(I+1)+K2*CRBP(I)=KSO*CRBP(I+1)
      DCPDND(1)=(CN+DCBP*CN1+DCBP)
      DFW*WFP(I+1)+K2*WFP(I)=KSO*WFP(I+1)
      DFB*WFP(I+1)+K2*WFP(I)=KSO*WFP(I+1)
      DFO*WZ(1)=(CN+DF*CN1+DFP)
      DWTAP*WTA(I+1)+K2*WTA(I)=KSO*WTA(I+1)
      DWTBP*WTA(I+1)=K1*WTA(I)+K*WTA(I+1)
      X(1)=CRCP(I)
      X(2)=DCBPND*SF(I)+2.*XE*8FX(I)
      X(3)=F(1)*(RETATA+TAUF/(1.+ALTAU))=TAU*U*0.9*ALPH*VEAL
      X(4)=2.*XE*F(I)

```



```

SUBROUTINE BLF(NORD,ETA,Y,YPRIM)
C-----THIS SUBROUTINE EXPRESSES THE SET OF O.D.E. TO BE SOLVED IN RKGL
REAL LAMDE,LAMDE,MU,NA,NE,MA
DIMENSION Y(NORD),YPRIM(NORD)
DIMENSION GUESS(4)
COMMON/BCON/UEP,PED,TAE,TEED,ALPED,TH,ALPH,UM,GUESS,ROLMUE
COMMON/GAS1/MA,R,TION,TEX,CAA,SAE,TACRI,TECRI
COMMON/GAS2/QAAC,QATC,CC1,CC2,CC3,CC4,DD1,DD2,DD3,DD4,TEEA
CP=2.54R
IF(ABS(Y(3)),LT,1.0E-6)Y(3)=0.0
IF(ABS(Y(5)),LT,1.0E-6)Y(5)=0.0
IF(ABS(Y(7)),LT,1.0E-6)Y(7)=0.0
ALPH=ALPED*Y(4)
TAE=UEP*Y(4)
TE=UEP*Y(6)
IF(CALPH,LT,0.0)ALPH=1.0E-20
IF(TA,LE,100)TA=100.
IF(TE,LE,100)TE=100.
CALL DENSIT(PED,TA,TE,ALPH,NA,NE,ROL)
CALL TRANSP(TA,TE,NA,NE,MU,LAMDE,DAMB,VEA1)
C=ROL*MU/ROLMUE
PR=MU*CP/LAMD
SC=HU/(ROL*DAMB)
PRE=MU*CP/LAMDE
YPRIM(1)=Y(2)
YPRIM(2)=Y(3)/C
YPRIM(3)=Y(1)*YPRIM(2)
YPRIM(4)=Y(5)*SC/C
YPRIM(5)=Y(1)*YPRIM(4)
YPRIM(6)=Y(7)*PR/C
YPRIM(7)=Y(1)*YPRIM(6)*UED/(CP*TAE)*Y(3)*Y(3)/C
YPRIM(8)=Y(9)*PRE/C
YPRIM(9)=ALPED*YPRIM(8)*(Y(5)+Y(4)*Y(1))
RETURN
END

```

```

SUBROUTINE OUTDSK(J,XREAL,XI,OX,PED,GAM1,N,CR,CRPR,CRSC,CRPRE)
C-----THIS SUBROUTINE WRITES THE OUTPUT ON THE TAPE 3
DIMENSION MF(100),MZ(100),MTA(100),MTE(100)
DIMENSION CR(100),CRPR(100),CRSC(100),CRPRE(100)
COMMON/DESK/MF,MZ,MTA,MTE
INTEGER OUT
DATA OUT/3/
WRITE(OUT) J,XREAL,XI,OX,PED,GAM1,(MF(I),MZ(I),MTA(I),MTE(I),CR(I),
1,CRPR(I),CRSC(I),CRPRE(I),I=1,N)
RETURN
END

```

```

40 GO TO 70
CONTINUE
45 DO 45 J=1,NGUESS
D(J,I)=FD(J,3)=FD(J,1)/(STEPD*STEPD)
KSAVE=2
50 YINIT(I)=GUESS(I)
CONTINUE
CALL MINVRS(D,4,NGUESS,DET,IM1,IM2,IER)
DO 55 I=1,NGUESS
PROB=0.0
DO 55 J=1,NGUESS
PROD=PROD+(I,J)*FD(J,2)
55 GUESS(I)=GUESS(I)-PROD
60 CONTINUE
C-----PROCEED WITH THE CORRECT INITIAL VALUES AND SOLVE
70 DO 75 I=1,9
V(I)=YINIT(I)
75 ETAP=0.0
DO 80 I=1,N
ETAY(I)=ETA
F(I)=Y(2)
Z(I)=Y(4)
THETA(I)=Y(6)
THETE(I)=Y(8)
STEPD=ETA*(K=1)
ETA=ETA+STEPL
IF(ISTEP,GT,STPMAX)STEPL=STPMAX
IF(I,LE,LAST) CALL RKGL(Y,YPRIM,ETA,ETA1,STEPL,BLF)
80 ETAE=ETA1
DO 90 I=1,N
TAE=ETA1*THETA(I)
TE=ETA1*THETE(I)
ALPH=ALPED*Z(I)
CALL DENSIT(PED,TA,TE,ALPH,NA,NE,ROL)
CALL TRANSP(TA,TE,NA,NE,MU,LAMDE,DAMB,VEA1)
RHO(I)=ROL
DENNE(I)=NE
IF(I,GT,1)MUM=HU
CR(I)=ROL*MU/ROLMUE
CRPR(I)=CR(I)*LAMD/(MU*CP)
CRSC(I)=CR(I)*ROL*DAMB/MU
CRPRE(I)=CR(I)*LAMD/(MU*CP)
90 PRINT I,YINIT
1 FORMAT(IH,---INITIAL VALUES FOR V(I)=Y(9) IN THE BEGIN SUBROUTINE
1---,//9F10.6)
RETURN
END

```



```

SUBROUTINE DENSITY(P,TA,TE,ALPHA,NA,NE,RHO)
C-----FIND THE PLASMA DENSITY AND NUMBER DENSITIES OF ATOMS 3 ELECTRONS
REAL NA,NA,NE
COMMON/GAS1/NA,R,TION,TEXC,SAA,SAT,TACRI,TECRI
RHO=P/(R*(TALPHA*TE))
NE=RHO*ALPHA/NA
NARHO=C(1.-ALPHA)/NA
IF(NE.LT.100.)NE=100.
RETURN
END

```

```

SUBROUTINE TRANSPITA,TE,NA,NE,MU,LAMD,LAMDE,DAMB,VEAI)
C-----FIND THE TRANSPORT PROPERTIES, MU,LAMD,LAMDE,DAMB,VEAI)
REAL LAMD,LAMDE,NA,NE,NA,NE,MU
COMMON/GAS1/NA,R,TION,TEXC,SAA,SAT,TACRI,TECRI
COMMON/GAS2/QAAC,QAIC,CC1,CC2,CC3,CC4,DD1,DD2,DD3,DD4,TEEA
DATA ME/9.10956E-28/
QAAC=QAIC/(TA*0.25)
QAIC=QAIC/(TA*0.09)
IF (TE*TEEA) 2,2,3
IF (TA*CC1+CC2*TE+CC3*TE+CC4*TE*TE)*1.0E-16
GO TO 4
QEA=(DD1+DD2*TE+DD3*TE+TE+DD4*TE*TE)*1.0E-16
RATIO=10.
IF(NE.GT.0.)RATIO=LOG(TE*TE*TE/NF)
IF(RATIO>11.59)12,12,13
ALOGG=7.4929+0.3333*RATIO
GO TO 9
ALOGG=9.42453+0.5*RATIO
QEA=3.064E-6*ALOGG/(TE*TE)
QEA=QEA
RATIO=10.
IF(NE.GT.0.)RATIO=LOG(TA*TA*TA/NE)
IF(RATIO>11.59)12,12,13
ALOGG=7.4929+0.3333*RATIO
GO TO 15
ALOGG=9.42453+0.5*RATIO
QI=4.3064E-6*ALOGG/(TA*TA)
CA=SQRT(3.515725E-16*TA/NA)
CF=SQRT(3.515725E-16*TE/NE)
AA=0.7071*NA*CA/(NA+QEA+NE+QAI)
AI=0.7071*NE*CA/(NA+QAI+NE+QII)
AE=NE*CF/(2.*NA+QEA+2.*NE+QEI+1.4142*NE*QEE)
MUEQ=49067*MA*(AA+AI)
LAMD=2.9142E-16*(AA+AI)
LAMDE=2.9142E-16*AE
IF(LAMDE.LT.1.00)LAMDE=1.00
DAMB=2.*0.4152*CA/(NE+NA)*QAI)
VFAI=2.*CF*(NA+QEA+NE+QEI)*NE/NA
RETURN
END

```

```

SUBROUTINE RKILL(V,YPRIM,NORD,A,B,STEP,DER)
C-----THE RUNGE-KUTTA METHOD WITH GILL'S COEFFS. IS APPLIED FOR O.D.E's
REAL Y(NORD),YPRIM(NORD),Z(0),YV(9),Q(1)
NSTEP=5*(B-A)/STEP
M(B-A)/NSTEP
L=0
X=A

```

```

100 CALL DER(NORD,X,Y,YPRIM)
DO 1 I=1,NORD
Z(I)=YPRIM(I)*H
YV(I)=YV(I) + 0.5*Z(I)
1 Q(I)=Z(I)
CALL DER(NORD,X+0.5*H,YV1,YPRIM)
DO 2 I=1,NORD
Z(I)=YPRIM(I)*H
YV(I)=YV(I) + 0.2928934*(Z(I)-Q(I))
YV(I)=YV(I) + 0.121321*Q(I) + 0.344213*Z(I)
2 Q(I)=0.121321*Q(I) + 0.5857868*Z(I)
CALL DER(NORD,X+0.5*H,YV1,YPRIM)
DO 3 I=1,NORD
Z(I)=YPRIM(I)*H
YV(I)=YV(I) + 1.707107*(Z(I)-Q(I))
YV(I)=YV(I) + 0.121321*Q(I) + 0.344213*Z(I)
3 Q(I)=0.121321*Q(I) + 0.5857868*Z(I)
CALL DER(NORD,X+H,YV1,YPRIM)
DO 4 I=1,NORD
Z(I)=YPRIM(I)*H
YV(I)=YV(I) + 0.1666666*Z(I) - 0.3333333*Q(I)
4 Y(I)=YV(I) + 0.1666666*Z(I) - 0.3333333*Q(I)
X=X+H
L=L+1
IF(L-NSTEP)100,5,5
5 RETURN
END

```

```

SUBROUTINE INTRG(K,DETA1,N,Y,Z)
C-----TO PERFORM THE INTEGRATION BASED ON THREE-POINT DIFFERENCE SCHEME
REAL Y(N),Z(N),K
C=(3.*K+2.)/(K+1.)
C2=(3.*K+1.)/K
Z(1)=Y(1)*K
Z(1)=0.0
N=N+1
DO 1 I=2,N1
Z(I)=Z(I-1)+K*(I-2)*DETA1/6.+(C1*Y(I-1)+C2*Y(I)-C3*Y(I+1))
Z(N)=Z(N-1)+0.5*K*(N-2)*DETA1+(Y(N-1)+Y(N))
RETURN
END

```

```

SUBROUTINE MINVRS(A,IA,MA,DETA,IR,IC,IER)
C-----TO EVALUATE THE MATRIX INVERSE OF MATRIX A
DIMENSION A(6,6),IR(4),IC(4)
DO 1 I=1,MA
  IR(I)=0
  IC(I)=0
  DETA=1.0
  S=0.0
  R=MA
  CALL SUBRCS(A,IA,IA,MA,MA,IR,IC,I,J)
  PIV=AI(I,J)
  DETA=PIV*DETA
  V=ABS(PIV)
  IF(V.EQ.0.)GO TO 17
  IR(I)=J
  IC(J)=I
  PIV=1.0/PIV
  AI(I,J)=PIV
  DO 5 K=J,MA
    IF(K.NE.J)A(I,K)=A(I,K)*PIV
  DO 9 K=J,MA
    IF(K.EQ.I)GO TO 9
    PIV=A(K,J)
    DO 8 L=J,MA
      IF(L.NE.J)A(K,L)=A(K,L)-PIV*A(I,L)
    DO 11 K=J,MA
      IF(K.NE.I)A(K,J)=PIV*A(K,J)
    S=S+1.0
    IF(S.LT.R)GO TO 2
    DO 16 I=1,MA
      K=IC(I)
      M=IR(I)
      IF(K.EQ.I)GO TO 16
      DETA=DETA
      DO 14 L=J,MA
        TEMP=A(K,L)
        A(K,L)=A(I,L)
        A(I,L)=TEMP
      DO 15 L=J,MA
        TEMP=A(L,M)
        A(L,M)=A(L,I)
        A(L,I)=TEMP
      IC(M)=K
      IR(K)=M
    CONTINUE
    IERSO
    RETURN
  IERS=1
  PRINT 18
  FORMAT('***MATRIX IS SINGULAR**')
  RETURN
END

```

```

SUBROUTINE RATES(TA,TE,MA,NE,NEDOTA,NEDOTE)
C-----FIND THE CHEMICAL REACTION RATES, NEDOTA/NE, NEDOTE/NE
REAL RZA,RE,KRA,KRE,RA,MA,NE,NEDOTA,NEDOTE
COMMON/SA3/MA,R,TION,TEXC,SA,SAF,TACRI,TECRI
COMMON/SA3/EE1,EE2,EE3
A=TA
E=TE
A=TA
E=TE
IF (AA.LT.TACRI) A=TACRI
KRA=1.18249E-12*SA*SQRT(AA/MA)*AA*(TEXC/AA+2.)/EXP(TEXC/AA)
KRE=KRA/EEK(AA)
NEDOTA=0
IF(NE.GT.0)NEDOTA=MA*(KRA*MA/NE-KRA*NE)
IF(NEDOTA.LT.0.0)NEDOTA=0.0
IF (EE.LT.TECRI) GO TO 7
KPE=3.5331*SA*EE*1.5*(TEXC/EE+2.)/EXP(TEXC/EE)
KRE=KPE/EEK(EE)
GO TO 8
7 KRE=1.0*EE-8/EE+8.5
KPE=KRE*EEK(EE)
NEDOTE=KPE*MA-KRE*NE
RETURN
END

```

```

FUNCTION EOK(T)
C-----FIND THE EQUILIBRIUM RATE COEFFICIENT KEO BY GIVEN TEMPERATURE T
REAL MA
COMMON/SA3/MA,R,TION,TEXC,SA,SAF,TACRI,TECRI
COMMON/SA3/EE1,EE2,EE3
EOK=0.0
R=ATION/T
IF (RATIO.GT.100.) RETURN
Z=EE1+EE2/EXP(EE3/T)
EOK=4.8290E15*Z1*(T+1.5)/EXP(TION/T)
RETURN
END

```

```

FUNCTION GRAD(NE,TE)
C-----TO CALCULATE THE TOTAL RADIATION ENERGY LOSS,GRAD
REAL NE
COMMON/SA3/MVC,ZEFF
GRAD=1.032545E-11*ZEFF*ZEFF*NE*(MVC+1.380622E-16*TE)/SORT(TE)
GRAD=2.0*GRAD
RETURN
END

```

```

SUBROUTINE SUBMCS(A,IA,JA,MA,NA,IR,IC,I,J)
  DIMENSION A(4,4),IR(4),IC(4)
  I=0
  J=0
  TEST=0.0
  DO 5 K=1,MA
    IF(IR(K).NE.0)GO TO 5
    DO 4 L=1,NA
      IF(IC(L).NE.0)GO TO 4
      X=ABS(A(K,L))
      IF(X.LT.TEST)GO TO 4
      IK=K
      JL=L
    5
  4
  TEST=X
  CONTINUE
  CONTINUE
  RETURN
  END

```

```

SUBROUTINE CRANK(IBC,SLOPE,DETA1,N,MSTART)
  C-----AN ALGORITHM TO CALCULATE A TRI-DIAGONAL MATRIX EQUATION (ABC)*M=ED
  DIMENSION M(100,4),MSTART(100)
  COMMON/BLK1/A(100),B(100),C(100),D(100),D1(100),D2(100),X(5)
  MNSHSTART(1)
  MNSHSTART(N+1)
  NISH=1
  DO 1 I=1,N1
    M(I,1)=A(I)
    M(I,2)=B(I)
    M(I,3)=C(I)
    M(I,4)=D(I)
    M(NI,3)=0.0
    M(NI,4)=D(NI)
    IF(IBC.EQ.1)GO TO 4
    M(I,2)=A(I)+B(I)
    M(I,4)=D(I)+A(I)*SLOPE+DETA1
    M(NI,4)=D(NI)+C(NI)*M(N)
    CALL TROG(M,N1)
    DO 5 I=2,N
      MSTART(I)=M(I-1,4)
      IF(IBC.EQ.2)MSTART(1)=M(1,4)-SLOPE*DETA1
    5
  RETURN
  END

```

```

SUBROUTINE TROG(M,N)
  DIMENSION M(100,4)
  DO 10 I=2,N
    M(I,2)=M(I,2)+M(I-1,2)*M(I-1,3)
    M(I,4)=M(I,4)+M(I-1,4)+M(I-1,2)*M(I-1,4)
    NISH=N-1
    DO 20 I=1,NM1
      M(NI,4)=M(NI,4)+M(NI,3)*M(NI+1,4)
    20
    DO 30 I=1,N
      M(I,4)=M(I,4)/M(I,2)
    30
  RETURN
  END

```

```

SUBROUTINE COEFF(I,DX,DDX,XP)
  C-----CALCULATE THE MATRIX ELEMENTS A,B,C,AND D USED IN CRANK
  REAL X
  COMMON/FNDIF/K,CH,DETA1,N,DEX,IBC
  COMMON/BLK1/A(100),B(100),C(100),D(100),D1(100),D2(100),X(5)
  SAA=CN*D2(I)
  SBB=(1.-CN)*D2(I)
  SCC=CN*D1(I)
  SDD=(1.-CN)*D1(I)
  A(I)=SAA+K*X(1)-SCC*K*K*X(2)
  B(I)=SAA*X(1)+(-1.-K)*SCC*X(2)+K*K*X(3)+CN*X(3)+X(4)/DEX
  C(I)=SAA+K*X(1)+SCC*X(2)
  D(I)=SBB+K*X(1)+DDX*SDD+X(2)+DX*(-1.-CN)*X(3)+XP-X(4)/DEX+XP*X(5)
  RETURN
  END

```

```

SUBROUTINE DXCTL(DX,THICKD,CONTL,DIFF,LITER)
  C-----THIS IS A SUBROUTINE TO CONTROL THE STEP-SIZE DX
  DX=DX
  IF(LITER.GE.8)GO TO 1
  IF(DIFF.LT.0.001)CONTL=1.5*CONTL
  IF(DIFF.GT.0.001.AND.DIFF.LT.0.002)CONTL=1.3*CONTL
  IF(DIFF.GT.0.002.AND.DIFF.LT.0.005)CONTL=1.2*CONTL
  IF(DIFF.GT.0.005.AND.DIFF.LT.0.01)CONTL=1.1*CONTL
  IF(DIFF.GT.0.01.AND.DIFF.LT.0.015)CONTL=1.05*CONTL
  IF(DIFF.GT.0.015.AND.DIFF.LT.0.02)CONTL=0.95*CONTL
  IF(DIFF.GT.0.02)CONTL=0.9*CONTL
  DX=CONTL*ABS(THICKD)
  IF(DX.LT.1.E-6)DX=1.E-6
  IF(DX.GT.0.03)DX=0.03
  RETURN
  CONTINUE
  DX=0.5*DX
  CONTL=0.5*CONTL
  RETURN
  END

```


UTIAS REPORT NO. 226

Institute for Aerospace Studies, University of Toronto (UTIAS)
4925 Dufferin Street, Downsview, Ontario, Canada, M3H 5T6

Liu, W. S. 108 pages 27 figures

1. Finite difference solutions
2. Nonequilibrium flat-plate boundary layers
3. Nonequilibrium sidewall boundary layers.

I. Liu, W. S. II. UTIAS Report No. 226

Details are given of an implicit six-point finite-difference scheme for solving two-temperature chemical nonequilibrium laminar boundary-layer flows in ionizing argon. The analysis extends previous work by considering the radiation-energy loss and the chemical reactions in the plasma of the ionizing boundary layer. The variations of transport properties based on the known elastic-scattering cross-sections for an argon plasma across the boundary layer are considered. The effects of the chemical reactions, radiation-energy loss and the electric sheath on the boundary-layer structures are discussed. Both the flat-plate and the shock-tube sidewall boundary-layer flows are analyzed and compared with interferometric data obtained using the UTIAS 10 cm x 18 cm Hypervelocity Shock Tube at shock Mach numbers $M_\infty \approx 13$ and ~ 16 at an initial argon pressure $P_0 \sim 5$ torr and temperature $T_0 \sim 300$ K. Fairly good agreement was obtained between analysis and experiment for both types of boundary layers.



Available copies of this report are limited. Return this card to UTIAS, if you require a copy.

UTIAS REPORT NO. 226

Institute for Aerospace Studies, University of Toronto (UTIAS)
4925 Dufferin Street, Downsview, Ontario, Canada, M3H 5T6

Liu, W. S. 108 pages 27 figures

1. Finite difference solutions
2. Nonequilibrium flat-plate boundary layers
3. Nonequilibrium sidewall boundary layers.

I. Liu, W. S. II. UTIAS Report No. 226

Details are given of an implicit six-point finite-difference scheme for solving two-temperature chemical nonequilibrium laminar boundary-layer flows in ionizing argon. The analysis extends previous work by considering the radiation-energy loss and the chemical reactions in the plasma of the ionizing boundary layer. The variations of transport properties based on the known elastic-scattering cross-sections for an argon plasma across the boundary layer are considered. The effects of the chemical reactions, radiation-energy loss and the electric sheath on the boundary-layer structures are discussed. Both the flat-plate and the shock-tube sidewall boundary-layer flows are analyzed and compared with interferometric data obtained using the UTIAS 10 cm x 18 cm Hypervelocity Shock Tube at shock Mach numbers $M_\infty \approx 13$ and ~ 16 at an initial argon pressure $P_0 \sim 5$ torr and temperature $T_0 \sim 300$ K. Fairly good agreement was obtained between analysis and experiment for both types of boundary layers.



Available copies of this report are limited. Return this card to UTIAS, if you require a copy.

UTIAS REPORT NO. 226

Institute for Aerospace Studies, University of Toronto (UTIAS)
4925 Dufferin Street, Downsview, Ontario, Canada, M3H 5T6

Liu, W. S. 108 pages 27 figures

1. Finite difference solutions
2. Nonequilibrium flat-plate boundary layers
3. Nonequilibrium sidewall boundary layers.

I. Liu, W. S. II. UTIAS Report No. 226

Details are given of an implicit six-point finite-difference scheme for solving two-temperature chemical nonequilibrium laminar boundary-layer flows in ionizing argon. The analysis extends previous work by considering the radiation-energy loss and the chemical reactions in the plasma of the ionizing boundary layer. The variations of transport properties based on the known elastic-scattering cross-sections for an argon plasma across the boundary layer are considered. The effects of the chemical reactions, radiation-energy loss and the electric sheath on the boundary-layer structures are discussed. Both the flat-plate and the shock-tube sidewall boundary-layer flows are analyzed and compared with interferometric data obtained using the UTIAS 10 cm x 18 cm Hypervelocity Shock Tube at shock Mach numbers $M_\infty \approx 13$ and ~ 16 at an initial argon pressure $P_0 \sim 5$ torr and temperature $T_0 \sim 300$ K. Fairly good agreement was obtained between analysis and experiment for both types of boundary layers.



Available copies of this report are limited. Return this card to UTIAS, if you require a copy.

UTIAS REPORT NO. 226

Institute for Aerospace Studies, University of Toronto (UTIAS)
4925 Dufferin Street, Downsview, Ontario, Canada, M3H 5T6

Liu, W. S. 108 pages 27 figures

1. Finite difference solutions
2. Nonequilibrium flat-plate boundary layers
3. Nonequilibrium sidewall boundary layers.

I. Liu, W. S. II. UTIAS Report No. 226

Details are given of an implicit six-point finite-difference scheme for solving two-temperature chemical nonequilibrium laminar boundary-layer flows in ionizing argon. The analysis extends previous work by considering the radiation-energy loss and the chemical reactions in the plasma of the ionizing boundary layer. The variations of transport properties based on the known elastic-scattering cross-sections for an argon plasma across the boundary layer are considered. The effects of the chemical reactions, radiation-energy loss and the electric sheath on the boundary-layer structures are discussed. Both the flat-plate and the shock-tube sidewall boundary-layer flows are analyzed and compared with interferometric data obtained using the UTIAS 10 cm x 18 cm Hypervelocity Shock Tube at shock Mach numbers $M_\infty \approx 13$ and ~ 16 at an initial argon pressure $P_0 \sim 5$ torr and temperature $T_0 \sim 300$ K. Fairly good agreement was obtained between analysis and experiment for both types of boundary layers.



Available copies of this report are limited. Return this card to UTIAS, if you require a copy.

UTIAS REPORT NO. 226

Institute for Aerospace Studies, University of Toronto (UTIAS)
4925 Dufferin Street, Downsview, Ontario, Canada, M3H 5T6

Liu, W. S. 108 pages 27 figures

1. Finite difference solutions
2. Nonequilibrium flat-plate boundary layers
3. Nonequilibrium sidewall boundary layers.

I. Liu, W. S. II. UTIAS Report No. 226

Details are given of an implicit six-point finite-difference scheme for solving two-temperature chemical nonequilibrium laminar boundary-layer flows in ionizing argon. The analysis extends previous work by considering the radiation-energy loss and the chemical reactions in the plasma of the ionizing boundary layer. The variations of transport properties based on the known elastic-scattering cross-sections for an argon plasma across the boundary layer are considered. The effects of the chemical reactions, radiation-energy loss and the electric sheath on the boundary-layer structures are discussed. Both the flat-plate and the shock-tube sidewall boundary-layer flows are analyzed and compared with interferometric data obtained using the UTIAS 10 cm x 18 cm Hypervelocity Shock Tube at shock Mach numbers $M_\infty = 13$ and ~ 16 at an initial argon pressure $P_0 \sim 5$ torr and temperature $T_0 \sim 300$ K. Fairly good agreement was obtained between analysis and experiment for both types of boundary layers.



Available copies of this report are limited. Return this card to UTIAS, if you require a copy.

UTIAS REPORT NO. 226

Institute for Aerospace Studies, University of Toronto (UTIAS)
4925 Dufferin Street, Downsview, Ontario, Canada, M3H 5T6

Liu, W. S. 108 pages 27 figures

1. Finite difference solutions
2. Nonequilibrium flat-plate boundary layers
3. Nonequilibrium sidewall boundary layers.

I. Liu, W. S. II. UTIAS Report No. 226

Details are given of an implicit six-point finite-difference scheme for solving two-temperature chemical nonequilibrium laminar boundary-layer flows in ionizing argon. The analysis extends previous work by considering the radiation-energy loss and the chemical reactions in the plasma of the ionizing boundary layer. The variations of transport properties based on the known elastic-scattering cross-sections for an argon plasma across the boundary layer are considered. The effects of the chemical reactions, radiation-energy loss and the electric sheath on the boundary-layer structures are discussed. Both the flat-plate and the shock-tube sidewall boundary-layer flows are analyzed and compared with interferometric data obtained using the UTIAS 10 cm x 18 cm Hypervelocity Shock Tube at shock Mach numbers $M_\infty = 13$ and ~ 16 at an initial argon pressure $P_0 \sim 5$ torr and temperature $T_0 \sim 300$ K. Fairly good agreement was obtained between analysis and experiment for both types of boundary layers.



Available copies of this report are limited. Return this card to UTIAS, if you require a copy.

UTIAS REPORT NO. 226

Institute for Aerospace Studies, University of Toronto (UTIAS)
4925 Dufferin Street, Downsview, Ontario, Canada, M3H 5T6

Liu, W. S. 108 pages 27 figures

1. Finite difference solutions
2. Nonequilibrium flat-plate boundary layers
3. Nonequilibrium sidewall boundary layers.

I. Liu, W. S. II. UTIAS Report No. 226

Details are given of an implicit six-point finite-difference scheme for solving two-temperature chemical nonequilibrium laminar boundary-layer flows in ionizing argon. The analysis extends previous work by considering the radiation-energy loss and the chemical reactions in the plasma of the ionizing boundary layer. The variations of transport properties based on the known elastic-scattering cross-sections for an argon plasma across the boundary layer are considered. The effects of the chemical reactions, radiation-energy loss and the electric sheath on the boundary-layer structures are discussed. Both the flat-plate and the shock-tube sidewall boundary-layer flows are analyzed and compared with interferometric data obtained using the UTIAS 10 cm x 18 cm Hypervelocity Shock Tube at shock Mach numbers $M_\infty = 13$ and ~ 16 at an initial argon pressure $P_0 \sim 5$ torr and temperature $T_0 \sim 300$ K. Fairly good agreement was obtained between analysis and experiment for both types of boundary layers.



Available copies of this report are limited. Return this card to UTIAS, if you require a copy.

UTIAS REPORT NO. 226

Institute for Aerospace Studies, University of Toronto (UTIAS)
4925 Dufferin Street, Downsview, Ontario, Canada, M3H 5T6

Liu, W. S. 108 pages 27 figures

1. Finite difference solutions
2. Nonequilibrium flat-plate boundary layers
3. Nonequilibrium sidewall boundary layers.

I. Liu, W. S. II. UTIAS Report No. 226

Details are given of an implicit six-point finite-difference scheme for solving two-temperature chemical nonequilibrium laminar boundary-layer flows in ionizing argon. The analysis extends previous work by considering the radiation-energy loss and the chemical reactions in the plasma of the ionizing boundary layer. The variations of transport properties based on the known elastic-scattering cross-sections for an argon plasma across the boundary layer are considered. The effects of the chemical reactions, radiation-energy loss and the electric sheath on the boundary-layer structures are discussed. Both the flat-plate and the shock-tube sidewall boundary-layer flows are analyzed and compared with interferometric data obtained using the UTIAS 10 cm x 18 cm Hypervelocity Shock Tube at shock Mach numbers $M_\infty = 13$ and ~ 16 at an initial argon pressure $P_0 \sim 5$ torr and temperature $T_0 \sim 300$ K. Fairly good agreement was obtained between analysis and experiment for both types of boundary layers.



Available copies of this report are limited. Return this card to UTIAS, if you require a copy.